Department of Earth and Environmental Sciences
University of Milano-Bicocca

Light-absorbing impurities: source, transport and impact on the cryosphere using optical remote sensing.

Ph.D. Dissertation

Candidate:

Dr. Biagio Di Mauro

Tutor:

Dr. Roberto Colombo

Ph.D. Coordinator:

Prof. Valter Maggi

PH.D. SCHOOL OF ENVIRONMENTAL SCIENCES. XXVIII CYCLE

Acknowledgments:

I would like just to briefly acknowledge people of LTDA (Roberto, Tommaso, Cinzia, Micol, Francesco, Robi G, Marco, Chiara, Sergio, Fabio, Claudio, Giulia) that helped me during these year. In particular, I would like to mention Roberto Colombo, for his support and the trust he put in me during these years. I also wish all the best to Francesco and Nicla for their new life in Nairobi, and to Micol and his little Jacopo. I thank Giovanni and Robi G for sharing with me some dust and cryoconite fever. Finally, I thank my familiy, because none of this would have been possible without them.

Front cover: Landsat 8 tile of the European Alps (March 2014)

Back cover: Morteratsch glacier (Photo by G. Baccolo)

“Wovon man nicht sprechen kann,

darüber muss man schweigen”

Ludwig Wittgenstein *(1922)*

Index

Abstract (English)

The objective of my Ph.D. is to investigate the impact of light-absorbing impurities on the cryosphere using optical remote sensing data. Light-absorbing impurities (LAI) are particulate matter, such as mineral dust and black carbon, that can be deposited on snow and ice, reducing their albedo and accelerating the melt. The impact of LAI on the cryosphere has been studied at a global and regional scale, but still few scientific literature focuses on the European Alps.

In the first year, I conducted a sensitivity analysis of a radiative transfer model, the SNow, ICe, and Aerosol Radiative model (SNICAR) to study the optical properties of snow and ice. In particular, this model allows to simulate spectral reflectance of snow, as a function of different variables, such as snow grain size [μm], mineral dust concentration [ppm] and dimension [μm], black carbon concentration [ppb], solar zenith angle and snow density, using different atmospheric profiles. During the second year of Ph.D., different field campaigns were organized in order to measure spectral reflectance of snow after LAI depositional events, and to compare observed with simulated spectra. During field campaigns, we flew an Unmanned Aerial Vehicle (UAV) over a flat snow-covered area in the European Alps. Data collected from ground, UAV and satellite (Landsat 8 - Operational Land Imager, OLI) were analysed to estimate the impact of mineral dust on snow optical properties. A novel spectral index non-linearly correlated with mineral dust concentration was proposed and tested at different scales.

During the third year, I focused on the impact of LAI on ice in the Alps. Mountain glaciers represent an important source of fresh water across the globe. Those reservoirs are seriously threatened by global climate change, and a widespread reduction of glacier extension has been observed in recent years. Surface processes that promote ice melting are driven both by temperature/precipitation and by albedo. The latter is mainly influenced by the growth of snow grain size and by the impurities content (such as dust, soot, ash, algae etc.). The origin of these light-absorbing impurities can be local or distal; often they aggregate on the glacier tongue forming characteristic cryoconites, that decrease ice albedo promoting the melting. During summer 2015, two field campaigns were conducted at the Vadret da Morteratsch glacier (Swiss Alps). The aim of the campaings was to collect ground hyperspectral reflectance data and ice/snow samples at the glacier ablation zone. During August 2015, the Earth Observing One (EO-1) satellite was planned to acquire a series of scene over the Morteratsch glacier.

Furthermore, a Landsat 8 Operational Land Imager (OLI) was downloaded from the Earth Explorer portal. Results from spectra analysis showed interesting features in albedo distribution at Morteratsch glacier. In particular, the ablation area showed very low albedo values (circa 0.2), and this is probably due to multiple processes such as accumulation of particulate matters, collapsing of lateral moraine and debris covering. In addition, the presence of surface cryoconites strongly lowers ice albedo, ground measurements showed that these objects have an albedo smaller than 0.1 and that creates melt pond and surface run off that further increase the absorption of incident radiation and accelerate the melting. Hyperion and Landsat data showed that the glacier has areas with different spectral characteristics. In the area across the Equilibrium Line Altitude (ELA), outcropping dust from a Saharan event was also visible, this is highlighted by high Snow Darkening Index (SDI) values.

Abstract (Italian)

L'obiettivo del mio dottorato è studiare l'impatto delle *light-absorbing impurities* (LAI) sulla criosfera tramite l'utilizzo di telerilevamento ottico. Le LAI sono particelle atmosferiche, come polveri minerali e *black carbon*, che possono depositarsi su neve e ghiaccio riducendone l'albedo e favorendone la fusione. L'impatto delle LAI sulla criosfera è stato studiato a livello globale e locale, ma ancora poca letteratura scientifica è dedicata allo studio del fenomeno nelle Alpi Europee.

Durante il primo anno è stata sviluppata un'analisi di sensitività di un modello di trasferimento radiativo (SNow, ICe, and Aerosol Radiative model, SNICAR) con l'obiettivo di studiare le proprietà ottiche di neve e ghiaccio. In particolare, questo modello permette di simulare la riflettanza spettrale della neve in funzione di diverse variabili quali: la dimensione dei cristalli di neve [µm], la concentrazione di polveri minerali [ppm] e la loro distribuzione dimensionale [µm], la concentrazione di *black carbon* [ppb], l'angolo zenitale solare e la densità della neve, usando differenti profili atmosferici. In seguito a questa analisi di sensitività, sono state organizzate alcune campagne sperimentali, con l'obiettivo di misurare la riflettanza della neve in seguito ad un evento naturale di deposizione di LAI, quindi confrontare i dati osservati con quelli simulati con il modello SNICAR. Durante le campagne di misura, sono stati organizzati dei sorvoli con un Unmanned Aerial Vehicle (UAV) su zone coperte da neve nelle Alpi Europee. I dati acquisiti da terra, da UAV e da satellite (Landsat 8 - Operational Land Imager, OLI) sono stati analizzati con l'obiettivo di stimare l'impatto delle polveri minerali sulle proprietà ottiche della neve. In seguito, è stato sviluppato e testato un nuovo indice spettrale

(Snow Darkening Index, SDI), non-linearmente correlato alla concentrazione di polveri minerali nella neve.

Durante l'ultimo anno di dottorato, mi sono concentrato sull'impatto delle LAI sul ghiaccio in ambiente Alpino. I ghiacciai alpini rappresentano infatti un'importante fonte di acqua dolce a livello globale. Queste riserve sono seriamente minacciate dai cambiamenti climatici in atto, e in anni recenti è stata osservata una significativa riduzione delle masse glaciali. I processi superficiali che favoriscono la fusione del ghiaccio sono guidati da temperatura, precipitazioni e albedo. Quest'ultima è influenzata principalmente dalla dimensione dei cristalli di neve e dal contenuto di LAI. L'origine di queste impurità può essere prossimale o remota, e spesso queste si possono aggregare sulla lingua glaciale formando le caratteristiche crioconiti, le quali diminuiscono l'albedo del ghiaccio favorendone la fusione. Durante l'estate del 2015 sono state organizzate due campagne di misura sul ghiacciaio del Morteratsch (Alpi Svizzere). L'obiettivo delle campagne era quello di acquisire spettri di riflettanza e campioni di neve e ghiaccio, in modo da caratterizzare radiativamente e geochimicamente le polveri e i materiali depositati sul ghiacciaio. Inoltre, sono stati analizzati dati satellitari dei sensori Hyperion e Landsat, acquisiti a pochi giorni di distanza dalla campagna. I risultati hanno mostrato che le crioconiti possono diminuire la riflettanza del ghiaccio fino a 0.2 nelle lunghezze d'onda del visibile e vicino infrarosso. Questo processo può fortemente alterare i bilanci radiativi del ghiacciaio, siccome provoca la presenza di acqua di scorrimento superficiale, la quale assorbe ulteriore radiazione incidente e favorisce la fusione del ghiaccio sottostante. I dati Hyperion e Landsat hanno mostrato una grande variabilità nelle proprietà spettrali del ghiacciaio, in particolare tra zona di accumulo ed ablazione. Nella zona a cavallo della *Equilibrium Line Altitude* (ELA), degli strati di polveri sahariane sono inoltre visibili ed evidenziate dalle mappe di SDI.

1 Introduction

The cryosphere is an important constituent of a planetary system, since it regulates short wave radiation balance. On the Earth, the cryosphere is formed by mountain glaciers, ice sheets, ice caps, ice shelf, sea ice, seasonal snow, frozen rivers and lakes; and they cover up to 10% of Earth surface. During Earth climatic history, the cryosphere played a fundamental role in defining the global temperature. The extension of land and sea ice, promoted by Milankovian oscillations, caused the Earth to swing between glacial and interglacial periods [*Petit et al.*, 1999].

To date, the study of the cryosphere is an active field of research in the Earth and Environmental Sciences. In particular, because its components were found to be extremely sensitive to global climate changes. Mountain glaciers retreat and ice sheets negative mass balance became emblematic of the effect of natural and anthropogenic climate changes on natural environments. The attention gained by cryospheric changes due to climate variability raised a big body of scientific research that spans from paleoclimatic reconstruction to global climate modeling and remote sensing applications. The latter exploits the spectral difference of snow and ice in order to quantify variation in seasonal snow cover, extension ice sheet and sea ice during the satellite-era. Snow and ice crystals feature typical optical characteristics: they reflect the most radiation in visible wavelengths and absorb radiation in Near-InfraRed (NIR) and Short-Wave Infrared (SWIR). This behavior is due to the complex refractive index of ice crystals, which is depicted in Figure 1a. The optical characteristics of ice and snow are mainly dependent on the dimension of ice crystals, often referred as snow grain size or effective radius, when they are approximated by spheres (Mie scattering theory). Snow

1b grain size usually increases with snow aging, as the air contained is extruded from the snow pack creating longer path in photons scattering. As the light is absorbed by the snow pack, the reflectance decreases in the NIR and SWIR wavelengths (Figure)

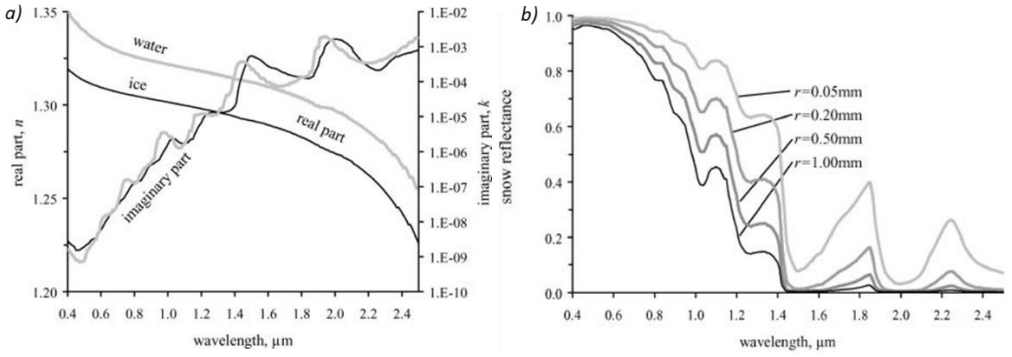

Figure 1 Left: Complex refractive index of ice (black line) and water (grey line). Right panel: spectral reflectance of snow as a function of snow grain size. [Dozier and Painter, 2004].

Other variables that influence snow and ice optical properties are solar zenith angle, snow density and concentration of light-absorbing impurities [*Warren and Wiscombe*, 1980; *Wiscombe and Warren*, 1980]. Typical impurities found in snow and ice can be summarized in three categories:

1. Mineral dust: from arid and hyper-arid region of the Earth, they are uplifted in the atmosphere by local or regional low pressure systems and then transported through the troposphere [*Mahowald et al.*, 2013];
2. Carbonaceous particles: those are Black Carbon (BC), Organic Carbon (OC) and Elemental Carbon (EC) produced by incomplete combustion of fossil fuels, biofuels and forest fires [*Bond et al.*, 2013].
3. Volcanic ash: large particle produced by volcanic activity, they can be directly deposited in snow and ice as tephra, or being re-suspended after being deposited in arid area (e.g. central Iceland)[*Dagsson-Waldhauserova et al.*, 2015]

The impact of these light-absorbing impurities on snow and ice optical properties consists in reducing the spectral reflectance in visible wavelengths (Figure 2) and promoting the melting. This is a complex process that involve also the increasing in grain size that further enhance the melting, in particular during the spring and summer season when snow and ice are directly exposed to higher solar radiation. This process has been studied both with experimental [*Painter et al.*, 2007, 2010; *Hadley and Kirchstetter*, 2012] and simulation data [*Flanner and Zender*, 2005; *Zhao et al.*, 2014] and showed to have a positive radiative forcing in the global climate system [*Bond et al.*, 2013]. In Figure 3, it is showed an example of the impact of BC on the climate system, including the source, transport and deposition on the cryosphere.

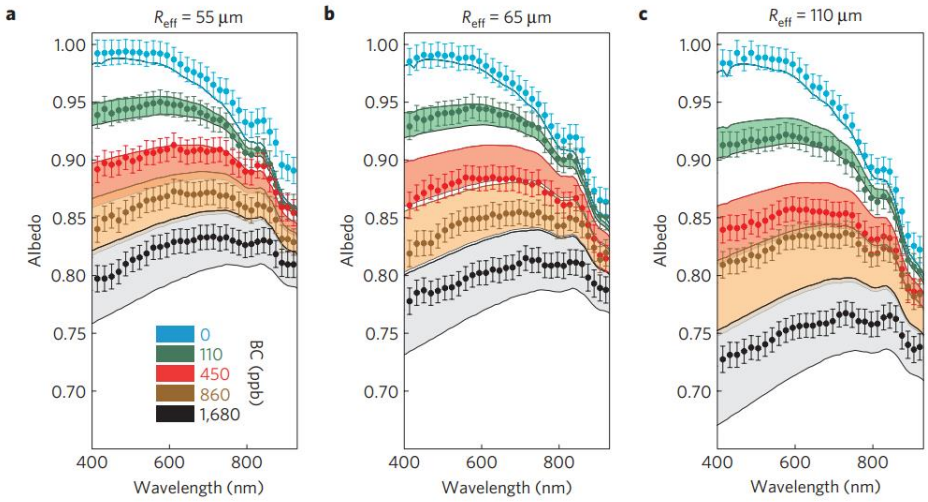

Figure 2 Impact of different concentrations of black carbon on snow spectral albedo, from [Hadley and Kirchstetter, 2012]

The source and transport of light-absorbing impurities are frequently observed combining satellite observations and simulated using Land Surface Models (LSM). Currently, LSM such as the Community Land Model (CLM) incorporates model schemes that simulate light-absorbing impurities emission, transport and impact on the cryosphere [*Flanner et al.*, 2007a]. Those LSM run at medium-coarse resolution (circa 1-

2 degrees) and are frequently used to study the impact of different natural and anthropogenic processes on global climate system. Regarding the impact of light-absorbing impurities, CLM has been widely applied to detect the timing of snow melt in the Boreal hemisphere [*Yasunari et al.*, 2015] and more in general for global radiative forcing estimations [*Flanner and Zender*, 2005; *Flanner et al.*, 2007b; *Sterle et al.*, 2013].

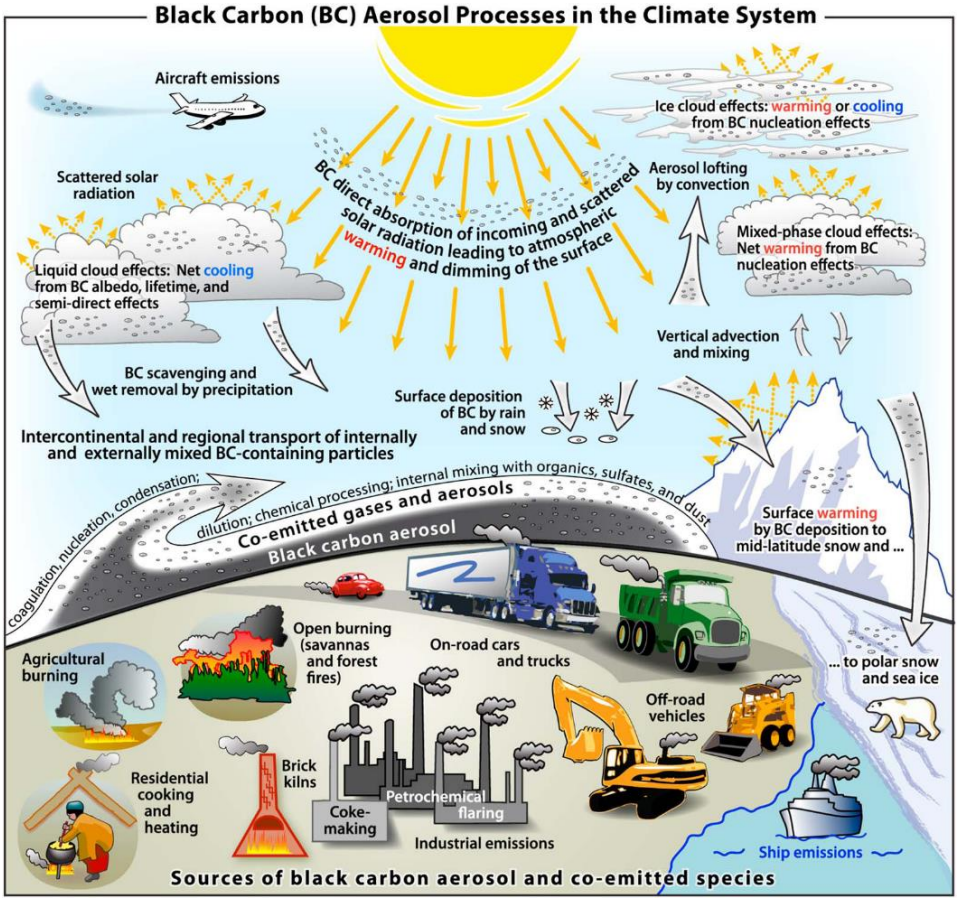

Figure 3 Source, transport and impact on the climate system of Black Carbon (from, [Bond et al., 2013])

Objectives and thesis structure

The main objective of this thesis is to determine the impact of light-absorbing impurities on seasonal snow and glaciers in the European Alps. Specific objectives regards the

integration of ground, Unmanned Aerial Vehicle (UAV) and satellite data, with radiative transfer and land surface modeling.

This Ph.D. thesis is structured as a collection of scientific papers. In fact, each chapter is an article with its own introduction, methods, results, discussion and conclusions. In Chapter 2, I present the activity conducted during 2014 aimed to determine the impact of mineral dust on snow in the European Alps combining ground, UAV and satellite observation with simulation using radiative transfer modeling. We conducted two field campaigns aimed at collecting ground spectral reflectance of snow after a Saharan dust deposition. During the first campaign, we also flew a fixed-wing UAV in order to create an orthophoto and a digital surface model of the area. Results were than compared with Landsat 8 synchronous acquisition. In Chapter 3, results obtained in the previous analysis were applied to repeated digital imagery acquired from an experimental micrometeorological station in the Aosta Valley, in order to link dust depositions and snowmelt during 2013 and 2014 melting seasons. In Chapter 4, I present the results from two campaigns at the Morteratsch glacier (Swiss Alps) where we collected spectral measurements and ice samples, integrating them with hyperspectral satellite data (from Hyperion sensor) in order to understand what caused glacier darkening observed by *Oerlemans et al.* [2009]. Chapter 5 presents conclusions gained from different analyses. At the end of the thesis, Appendix 1 reports an independent research that I conducted during the Ph.D. regarding a methodology to benchmark a land surface model (CLM) using power law size-frequency analysis. Appendix 2 instead presents a complete list of publications (journal articles and conferences) that I conducted and co-authored during the last three years.

Bibliography

Bond, T. C. et al. (2013), Bounding the role of black carbon in the climate system: A scientific assessment, *J. Geophys. Res. Atmos.*, *118*(11), 5380–5552, doi:10.1002/jgrd.50171.

Dagsson-Waldhauserova, P., O. Arnalds, H. Olafsson, J. Hladil, R. Skala, T. Navratil, L. Chadimova, and O. Meinander (2015), Snow–Dust Storm: Unique case study from Iceland, March 6–7, 2013, *Aeolian Res.*, *16*, 69–74, doi:10.1016/j.aeolia.2014.11.001.

Dozier, J., and T. H. Painter (2004), Multispectral and hyperspectral remote sensing of Alpine snow properties, *Annu. Rev. Earth Planet. Sci.*, *32*(1), 465–494, doi:10.1146/annurev.earth.32.101802.120404.

Flanner, M. G., and C. S. Zender (2005), Snowpack radiative heating: Influence on Tibetan Plateau climate, *Geophys. Res. Lett.*, *32*(6), L06501, doi:10.1029/2004GL022076.

Flanner, M. G., C. S. Zender, J. T. Randerson, and P. J. Rasch (2007a), Present-day climate forcing and response from black carbon in snow, *J. Geophys. Res.*, *112*(D11), D11202, doi:10.1029/2006JD008003.

Flanner, M. G., C. S. Zender, J. T. Randerson, and P. J. Rasch (2007b), Present-day climate forcing and response from black carbon in snow, , *112*(September 2006), 1–17, doi:10.1029/2006JD008003.

Hadley, O. L., and T. W. Kirchstetter (2012), Black-carbon reduction of snow albedo, *Nat. Clim. Chang.*, *2*(6), 437–440, doi:10.1038/nclimate1433.

Mahowald, N., S. Albani, J. F. Kok, S. Engelstaeder, R. Scanza, D. S. Ward, and M. G. Flanner (2013), The size distribution of desert dust aerosols and its impact on the Earth system, *Aeolian Res.*, doi:10.1016/j.aeolia.2013.09.002.

Oerlemans, J., R. H. Giesen, and M. R. Van Den Broeke (2009), Retreating alpine glaciers: increased melt rates due to accumulation of dust (Vadret da Morteratsch, Switzerland), *J. Glaciol.*, *55*(192), 729–736, doi:10.3189/002214309789470969.

Painter, T. H., A. P. Barrett, C. C. Landry, J. C. Neff, M. P. Cassidy, C. R. Lawrence, K. E. McBride, and G. L. Farmer (2007), Impact of disturbed desert soils on duration of

mountain snow cover, *Geophys. Res. Lett.*, *34*(12), L12502, doi:10.1029/2007GL030284.

Painter, T. H., J. S. Deems, J. Belnap, A. F. Hamlet, C. C. Landry, and B. Udall (2010), Response of Colorado River runoff to dust radiative forcing in snow, *Proc. Natl. Acad. Sci. U. S. A.*, (5), doi:10.1073/pnas.0913139107.

Petit, R. J., D. Raynaud, I. Basile, J. Chappellaz, C. Ritz, M. Delmotte, M. Legrand, C. Lorius, and L. Pe (1999), Climate and atmospheric history of the past 420,000 years from the Vostok ice core, Antarctica, *Nature*, *399*, 429–413, doi:10.1038/20859.

Sterle, K. M., J. R. McConnell, J. Dozier, R. Edwards, and M. G. Flanner (2013), Retention and radiative forcing of black carbon in eastern Sierra Nevada snow, *Cryosph.*, *7*(1), 365–374, doi:10.5194/tc-7-365-2013.

Warren, S. G., and W. J. Wiscombe (1980), A Model for the Spectral Albedo of Snow. II: Snow Containing Atmospheric Aerosols, *J. Atmos. Sci.*, *37*, 2734–2745, doi:10.1175/1520-0469(1980)037<2734:AMFTSA>2.0.CO;2.

Wiscombe, W. J., and S. G. Warren (1980), A Model for the Spectral Albedo of Snow. I: Pure Snow, *J. Atmos. Sci.*, *37*(12), 2712–2733, doi:10.1175/1520-0469(1980)037<2712:AMFTSA>2.0.CO;2.

Yasunari, T. J., R. D. Koster, K.-M. Lau, and K.-M. Kim (2015), Impact of snow darkening via dust, black carbon, and organic carbon on boreal spring climate in the Earth system, *J. Geophys. Res. Atmos.*, n/a–n/a, doi:10.1002/2014JD022977.

Zhao, C. et al. (2014), Simulating black carbon and dust and their radiative forcing in seasonal snow: a case study over North China with field campaign measurements, *Atmos. Chem. Phys.*, *14*(20), 11475–11491, doi:10.5194/acp-14-11475-2014.

2 Mineral dust impact on snow radiative properties in the European Alps combining ground, UAV and satellite observations.

Abstract

In this chapter, we evaluate the impact of mineral dust (MD) on snow radiative properties in the European Alps at ground, aerial and satellite scale. A field survey was conducted to acquire snow spectral reflectance measurements with an ASD Field-spec Pro spectroradiometer. Surface snow samples were analyzed to determine the concentration and size distribution of MD in each sample. An overflight of a four-rotor Unmanned Aerial Vehicle (UAV) equipped with an RGB digital camera sensor was carried out during the field operations. Finally, Landsat 8 Operational Land Imager (OLI) data covering the Central European Alps were analyzed.

Observed reflectance evidenced that MD strongly reduced the spectral reflectance of snow, in particular from 350 to 600 nm. Reflectance was compared with that simulated by parameterizing the Snow, Ice and Aerosol Radiation (SNICAR) radiative transfer model. We defined a novel spectral index, the Snow Darkening Index (SDI), that combines different wavelengths showing nonlinear correlation with measured MD concentrations (R2=0.87, RMSE=0.037). We also estimated a positive instantaneous radiative forcing that reaches values up to 153 W/m^2 for the most concentrated sampling area (107 ppm).

SDI maps at local scale were produced using the UAV data, while regional SDI maps were generated with OLI data. These maps show the spatial distribution of MD in snow after

a natural deposition from the Saharan desert. Such post-depositional experimental data are fundamental for validating radiative transfer models and Global Climate Models (GCM) that simulate the impact of MD on snow radiative properties.

2.1 Introduction

The Cryosphere is an integral part of the Earth system that includes the highest reflecting natural surfaces (albedo greater than 0.95 in visible spectrum for pristine snow). The Cryosphere plays a significant role in the global climate system and is particularly sensitive to very small variations in the amount of reflected/absorbed radiation, which have shown to produce significant effects on the hydrological cycle and the energy balance of the earth system at different spatial scales [*Flanner and Zender*, 2005; *Flanner et al.*, 2007; *Bond et al.*, 2013; *Painter et al.*, 2013a]. Besides the widespread general reduction in snow cover extent, changes in the Cryosphere associated with a general decrease in surface snow albedo are also involved in the positive feedback of a warming climate, and represent a topic of great societal concern.

Light absorption due to impurities content in snow and ice is involved in complex mechanisms such as the snow-albedo positive feedback [*Hansen and Nazarenko*, 2004; *Myhre et al.*, 2013], which represents a classical example of nonlinearity in the climate system, that is: the more the snow melts, the more radiation is absorbed and the more other snow melts. This process has shown to produce a significant impact on snow chemical [*Rhoades et al.*, 2010] and radiative properties [*Clarke and Noone*, 1985; *Flanner et al.*, 2007, 2009], snow hydrology [*Hadley et al.*, 2010; *Painter et al.*, 2012a; *Sterle et al.*, 2013; *Kaspari et al.*, 2015], timing of snow melt [*Li et al.*, 2013], vegetation phenology [*Steltzer et al.*, 2009] and also glacier retreat [*Oerlemans et al.*, 2009; *Wientjes et al.*, 2011; *Painter et al.*, 2013a].

The optical properties of snow and ice depend largely on the shape and dimension of their crystals: with an increase in the size of the crystals (often referred as “effective

radius", according to Mie's theory [*Mie*, 1908; *Wiscombe*, 1980]) reflected radiance decreases with great sensitivity at near-infrared and longer wavelengths [*Wiscombe and Warren*, 1980; *Warren*, 1982]. Light-absorbing impurities can also influence snow optical properties. Typical impurities are represented by carbonaceous particles [*Flanner et al.*, 2007; *Hadley and Kirchstetter*, 2012; *Doherty et al.*, 2014; *Meinander et al.*, 2014], volcanic ash [*Conway et al.*, 1996] and mineral dust [*Painter et al.*, 2010, 2012a, 2013b; *Li et al.*, 2013]. When deposited in snow, this particulate matter acts, at different degrees, like a black body absorbing radiation and thermalizing it through the media. This process alters the radiative balance of snow and ice, causing the absorption of an additional amount of radiation (i.e. radiative forcing, RF) and ultimately influencing surface melting processes of snow and ice.

Some methods based on numerical modeling have been proposed in literature with the aim of estimating the RF due to light-absorbing impurities such as black carbon (BC), mineral dust (MD) and volcanic ash (VA) deposited on snow and ice [*Jacobson*, 2004; *Flanner et al.*, 2007; *Aoki et al.*, 2011; *Yasunari et al.*, 2011; *Bauer and Ganopolski*, 2014]. While BC is emitted from both natural (*e.g.* forest fires) and anthropogenic (*e.g.* fossil fuel and biofuel combustion) sources [*Bond et al.*, 2013], the main sources of MD are represented by arid regions with low vegetation cover where fine-grained material is available [*Prospero*, 2002]. Once suspended in the atmosphere, MD aerosol influences climate both directly and indirectly [*Goudie and Middleton*, 2001; *Claquin et al.*, 2003; *Field et al.*, 2010; *Mahowald et al.*, 2013]. The direct effect consists mainly of changing the radiative properties of the atmosphere through the scattering and absorption of solar and terrestrial radiation. Conversely, the indirect effect of MD consists of acting as cloud condensation and ice nuclei and modifying cloud properties by delivering micronutrients (*e.g*. Fe) to the ocean [*Mahowald et al.*, 2005; *Winton et al.*, 2014], and modulating the uptake of carbon in the marine ecosystems and the atmospheric concentration of CO_2 (e.g. *Maher et al.*, 2010 and references therein). On the other hand, production and transport of dust is itself extremely sensitive to climate change

and is a current topic of active research; in this respect, past atmospheric conditions and particle deposition in mountainous and non-mountainous areas over the last centuries are widely studied using ice cores from non-polar glaciers and ice caps [*Sodemann et al.*, 2006; *Thevenon et al.*, 2009] and land-atmosphere model simulations [*Lawrence et al.*, 2011; *Albani et al.*, 2014].

Today, much scientific literature exists on numerical modeling [*Jacobson*, 2004; *Flanner et al.*, 2007; *Aoki et al.*, 2011; *Yasunari et al.*, 2011, 2015; *Liou et al.*, 2014] and controlled experiments on light-absorbing impurities on snow [*Brandt et al.*, 2011; *Hadley and Kirchstetter*, 2012; *Meinander et al.*, 2014]. However, only a few studies present field spectral data collected after events of MD deposition on snow and they are mainly located in the United States and Asia. These studies are fundamental for understanding the actual radiative effect of MD in snow-covered areas [*Pedersen et al.*, 2015] and for validation of Radiative Transfer (RT) models such as the Snow Ice and Aerosol Radiation (SNICAR) model [*Flanner et al.*, 2007, 2009]), which is included in the Community Land Model [*Lawrence et al.*, 2011]. In fact, those models are widely applied for local and global prediction of light-absorbing impurities in snow and ice [*McConnell et al.*, 2007; *Hadley and Kirchstetter*, 2012; *Lin et al.*, 2014].

Despite some uncertainties for BC [*Warren*, 2013], MD deposition on snow has been successfully investigated in the recent past using remotely sensed data [*Painter et al.*, 2012b, 2013b; *Gautam et al.*, 2013; *Li et al.*, 2013; *Dumont et al.*, 2014]. Recent studies have analyzed the impact of MD on snow and ice by integrating ground and satellite observations to physically-based models. These researches suggest that MD depositions alter the radiative balance of the region considered owing to the reduction of the snow cover associated with an increased melting rate that exposes darker surfaces (e.g. soil or vegetation) to direct solar radiation.

Some of these studies have also been conducted on the MD impact on snow in the Colorado river basin [*Painter et al.*, 2012a; *Bryant et al.*, 2013], Himalayan chain [*Painter*

et al., 2012b; *Gautam et al.*, 2013], Greenland [*Carmagnola et al.*, 2013; *Dumont et al.*, 2014], Iceland [*Dagsson-Waldhauserova et al.*, 2015] and Caucasus mountains [*Kutuzov et al.*, 2013], also in relation to the mineralogical composition of MD [*Reynolds et al.*, 2013].

Despite this increasing interest in the MD impact on snow, to date no studies that evaluate the BC and MD impact on snow have been conducted in the European Alps. The European Alps are considered to be highly sensitive to climatic and environmental conditions and even slight changes in radiative balances in mountain areas can influence the hydrological cycle and glacier retreat. These dependencies were also highlighted in a recent study suggesting that the deposition of industrial BC on snow may have played an important role in forcing the end of the Little Ice Age in the Alps [*Painter et al.*, 2013a]. The importance of MD on the Alps is stressed by the fact that a large amount of MD can be transported long-range from North Africa to Europe [*Tschiersch et al.*, 1990; *Sodemann et al.*, 2006] with significant direct and indirect radiative effects [*Helmert et al.*, 2007]. During these events, aeolian MD can also reach areas covered by seasonal or perennial snow and ice in the Alps [*De Angelis and Gaudichet*, 1991; *Franzén et al.*, 1995].

In this context, we have tried to fill the aforementioned gaps by measuring snow optical properties and MD content of a seasonal snow pack using a multi-scale approach in a test site in the European Alps, a few days after a significant MD transport event occurred in February 2014.

The main objective of this study is to investigate how Saharan MD alters Alpine snow optical properties by exploiting a combined approach based on ground hyperspectral measurements, a survey of an Unmanned Aerial Vehicle (UAV) and Landsat 8 Operational Land Imager (OLI) satellite data. Specific objectives of this study are:

i. To compare experimental data with a physically-based radiative transfer (RT) model;
ii. To develop a novel spectral index sensitive to MD concentration in snow;
iii. To exploit a spectral index to represent the spatial patterns of MD deposition in snow.

2.2 Study area and mineral dust transport

The campaign was conducted after a significant transport of MD from the Saharan desert occurred in February 2014. In the Mediterranean area, under peculiar meteorological conditions [*Pey et al.*, 2013], such as the passage of a cold front over the source and low pressure patterns over the Mediterranean Sea causing Sirocco (from South-East) or Libeccio winds (from South-West), dust can be suspended in the atmosphere and transported for hundreds of kilometers. These atmospheric conditions are quite frequent in the spring season in the Northern Hemisphere and they are mainly dictated by meteo-climatic patterns such as the North Atlantic Oscillation (NAO) [*Thevenon et al.*, 2009]. The study area is located on the Artavaggio plains (Lecco, Italy) at 1650 meters a.s.l. near Lake Lecco in a small portion of the central European Alps (Figure 1). MD was entrained in the troposphere over the North African Grand Erg Oriental (Saharan lowlands of northeast Algeria) on February 18th during the passage of a cold front, and then transported NE over the Mediterranean Sea by cyclonic atmospheric transport ("cut-off" block). MSG-SEVIRI data monitored the transport through the DUST-RGB product (Figure 1) in which the brightness temperatures at different infrared channels are combined to enhance the presence of MD layers in the atmosphere. As the plume reached the Italian peninsula, it was deposited by both wet and dry deposition over the Alpine chain. This deposition was forecasted by the BSC-DREAM-8b model [*Basart et al.*, 2012] operated at the Barcelona Supercomputing Center (Figure 2). The model predicted a significant amount (~50-100 mg/m^2) of MD to be deposited on the European Alpine chain as wet deposition (rain and snow).

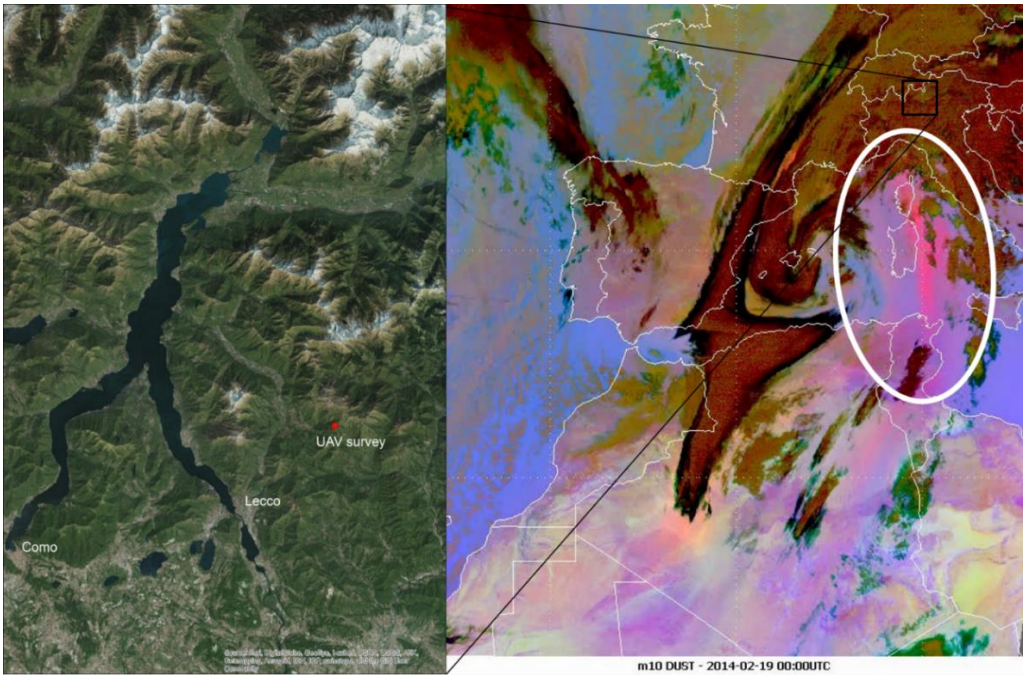

Figure 1 Left: focus on the Central European Alps, the red polygon represents the test site on the Artavaggio plains, where the UAV survey was performed. Right: Aeolian transport of MD from the Sahara desert (white ellipse) as seen by the MSG-SEVIRI Dust RGB product (copyright 2014 EUMETSAT). Dust RGB product represents dust in pink/magenta, instead clouds are represented in brown/orange. Further information about the dust transport event can be found at: http://www.eumetsat.int/website/home/Images/ImageLibrary/DAT_2104098.html

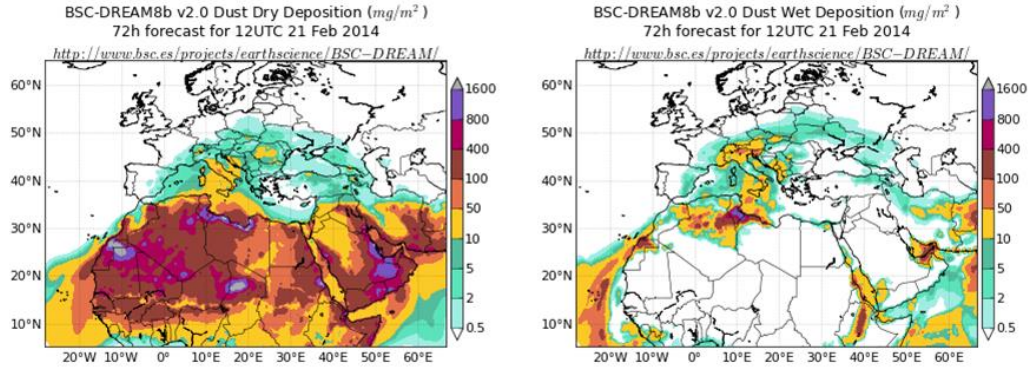

Figure 2 Dry and wet MD deposition as forecasted by the BSC-DREAM8 model. Image from the BSC-DREAM8b (Dust REgional Atmospheric Model) model, operated at the Barcelona Supercomputing Center (http://www.bsc.es/projects/earthscience/BSC-DREAM)

2.3 Materials & methods

2.3.1 Field and laboratory measurements

A field measurement campaign was organized on the Artavaggio plains on the 14th of March 2014, a few weeks after the MD deposition at the site on February 19th. The date of the campaign was chosen after a visual inspection of the heterogeneous outcrop of the MD due to the melting of the snow with the arrival of the spring. This situation generated a unique condition of high spatial variability, which allowed observation of the radiative effect (*e.g.* albedo decrease) of MD deposition on Alpine seasonal snow-packs.

In total, 10 sampling areas (each of 2 square meters) were defined on the Artavaggio plains. Sampling areas were selected by visual inspection to have a significant variability of MD concentration among samples. Three snow sampling areas were selected as "blanks", while seven others were selected because of their MD content. In this sense, "blanks" represent the cleanest snow in the area, but they contain a certain amount of impurities (i.e aerosol particles) of different natures. For each area, snow spectral reflectance was measured with a non-imaging hyperspectral radiometer, Analytical Spectral Devices (ASD) Field Spec pro. The instrument collects electromagnetic radiation ranging from 350 to 2500 nm with a Full-Width at Half Maximum (FWHM) of 5-10 nm and a spectral resolution of 1 nm. Measured reflected radiance $L_{ref}(\lambda)$ was converted into reflectance units $\rho(\lambda)$ normalizing for incident radiance $L_{inc}(\lambda)$ collected using a calibrated Lambertian Spectralon® panel. Spectral data were collected at each sampling area in clear-sky conditions during ~3 hours. Spectral measurements were performed using a bare optical fiber with a Field Of View (FOV) of 25 degrees. The distance between the optical fiber and the snow sample was 80 cm. The measurement was repeated three times for each area to calculate both the mean and the standard deviation of the reflectance.

Surface snow density and grain size were also measured in the field (first 5 centimeters of snow), this latter by comparison with a micron-sized grid.

Snow samples were collected from the first 5 centimeters of the snowpack using glass bottles of 1 L each. The bottles were previously cleaned three-times with ultra-pure water (Milli-Q®; 18.2 MΩ·cm at 25 °C; Water Purification System, Millipore, Bedford, MA, USA) exposing them for 20 minutes in an ultrasonic bath (SONICA®, Soltec, Italy).

After collection, the snow samples were stored in a polystyrene box surrounded by snow and transported to the University Campus in 2 h where they were stored at -20°C in darkness until they were analyzed. Snow samples were analyzed in a cold room to determine mass concentration and size distribution of MD (section 3.2).

The concentration and size-distribution of the insoluble particles were determined through two different methods: 1) a counting method (size range: 1 - 30 µm); 2) a gravimetric method (total bulk concentration).

The choice of using two experimental methods for MD characterization depends on the possibility of taking advantage of the strengths of each experimental technique: 1) the counting method allowed experimental determination of the MD size distribution in input to the simulation of the reflectance spectra using the Snow Ice and Aerosol Radiation (SNICAR) model; 2) the gravimetric method allowed experimental determination of the particulate matter mass concentration even below 1 µm and above 30 µm.

The counting method used a Coulter Counter (CC) technique. Samples were melted in a clean room (class 1000 clean room at EUROCOLD laboratory facilities, University of Milano-Bicocca) and diluted by a factor of ~10 with ultrapure (Milli-Q) water. Analyses were carried out using a Multisizer™ 3 COULTER COUNTER® set to measure particles with a diameter (equivalent spherical) between 1 and 30 µm in 300 size channels. To obtain dust mass from particle volume, a typical crustal density of 2.5 g/cm^3 was

adopted. MD total concentration from the CC method was estimated from the integral of the concentration between 1 and 18 µm to separate the contribution of MD particles from larger particles present in the sampled snow. Laboratory blanks were in all cases more than 100 times lower than the diluted samples. All steps of the analytical protocol followed *Delmonte et al.*, [2002] and *Ruth et al.*, [2008].

The gravimetric method (GM) allowed determination of the total mass concentration (ppm in melted snow) of MD deposited in the snow. Samples were first melted at ambient temperature (20°C) inside their own glass bottles used during the snow sampling, thus avoiding any external contamination during the melting. A magnetic stirred bar, pre-cleaned with ultrapure water (Milli-Q), allowed homogenization of the sample using magnetic stirring. The volume of the melted samples was determined using a graduated cylinder with a precision of ± 1 ml. The mass of the total particulate matter (PM: MD + other particles) in the melted snow was first collected using Millipore® filtering system equipped with a Whatman Quartz Fiber Filters (ø=47 mm). The mass of the filtered PM was determined as the weight difference of the filters observed after and before filtration of the melted snow. The weight of the filters was determined as the average value of three weights measured both before and after filtration of the melted snow using a Sartorius® SE2-F microbalance with a precision of ± 0.1 µg.

Before weighing, the filters were kept for 48 h at 20°C in darkness inside a silica-gel dryer (RH<2%) to remove all the water content. The final MD mass concentration was determined as the difference between the total PM concentration measured in each sample and the average PM concentration measured in the three blank samples. Considering the whole dataset and each source of uncertainty, the average error associated with the MD mass concentration in the snow was ± 0.87 ppm. As the MD concentration in the snow was very high (section 4.1, Table 1), this uncertainty represents on average 0.42 % of the measured MD and can be considered negligible for the scope of the present application.

2.3.2 Airborne and satellite data

During the field measurements, an Unmanned Aerial Vehicle (UAV) survey was performed to study the impact of MD on snow at local scale. The day after the campaign, a Landsat 8 tile was collected to analyze the impact of MD at regional scale in the Alps. Data acquisition and processing scheme are described in the following sections.

Unmanned Aerial Vehicle (UAV) survey

Recently, Unmanned Aerial Vehicles (UAVs) have been widely used for environmental monitoring [*Hodson et al.*, 2007; *Whitehead et al.*, 2013; *Immerzeel et al.*, 2014; *Lucieer et al.*, 2014], in particular for surveys in snow- and ice-covered areas difficult to reach for ground observation [*Ryan et al.*, 2015]. In this work we used a four-rotor UAV (ANTEOS, produced by http://www.aermatica.com) equipped with an RGB digital camera (model: Canon s100) that is automatically triggered (1 image/sec). The UAV is also equipped with a full Integrated Navigation System (INS) and with a Global Positioning System (GPS). The positioning data are used to precisely control the flight, to locate the UAV and to tag all data collected from the sensors. The sensor data are continuously displayed over a Mission Map in the Ground Control Station (GCS) monitor. RGB images collected on-board are digitized and sent through the wireless link directly to the GCS, where the operator can view the images and telemetry data (GPS coordinates, flight altitude, flight speed, roll, pitch and yaw) in the real-time mode. The UAV weights 9 kg and is able to carry a maximum payload of 2 kg with a flight autonomy of 20 minutes. With blades unfolded, the UAV features a width of 200 cm, a length of 200 cm and a height of 55 cm. Maximum forward flight speed is 5 m/s.

Two UAV overflights were organized to cover the whole study area. The altitude of the test site reduced the flight autonomy of the UAV, which flew at 30 m from the ground level for ~10 minutes/flight. RGB images acquired from the UAV survey (more than 600 images) were resampled to reduce computation time and then processed with a Structure From Motion (SFM) algorithm [*Westoby et al.*, 2012] implemented in the

Agisoft Photoscan© package (http://www.agisoft.com/). SFM processing allows exploitation of the overlap between adjacent images and creation of georeferenced orthomosaic maps and high resolution Digital Surface Models (DSM) of the test site. The position of the camera for each image was retrieved from the UAV telemetry acquired at constant frequency (1 data package/1 sec).

Landsat OLI data

A Landsat 8 Operational Land Imager (OLI) scene acquired the day after the campaign (14th Feb) was downloaded from the USGS Global Visualization Viewer (http://glovis.usgs.gov) repository. The OLI sensor collects reflected radiance in 9 spectral channels from visible to near-infrared wavelengths with a spatial resolution of 30 meters [*Irons et al.*, 2012]. The 9 OLI bands were converted first into Top Of Atmosphere (TOA) radiance and then into reflectance using the OLI calibration coefficients.

The correction for topographic and atmospheric effects of Landsat-8 OLI data was carried out using the ATCOR-3 code (Atmospheric/Topographic Correction for Mountainous Terrain) [*Richter*, 2007]. Similar to the whole ATCOR suite, ATCOR-3 also uses look-up tables generated by MODTRAN [*Berk et al.*, 1989], relating sensor radiances and albedo for various atmospheric and geometric conditions. Then ATCOR-3 includes the capability for radiometric correction in rugged terrain considering cast shadow and illumination calculations. In this study, ATCOR-3 was run with a winter mid-latitude atmospheric profile and an image-based estimate of the visibility based on the dark dense vegetation approach [*Kaufman and Sendra*, 1988]. The ASTER Global Digital Elevation Map (GDEM) at 30 meters spatial resolution was used for removing topographic effects. These corrections allowed removal of the atmospheric contribution by retrieving Top of Surface (TOS) reflectance and avoidance of the effect of shadow which is substantial in areas with complex topography such as the Alps.

2.3.3 RT modeling

Measured reflectances were compared to those simulated with the Snow Ice and Aerosol Radiation (SNICAR) model [*Flanner et al.*, 2007, 2009]. The model simulates hemispherical reflectance spectra between 300 and 5000 nm with a resolution of 10 nm. Model simulations were obtained by parameterizing the SNICAR radiative transfer model with observed variables. Those variables are: snow grain size (μm), snow density (Kg/m^3), snowpack thickness (m), surface spectral distribution, Solar Zenith Angle (SZA), MD concentration in four particle dimension classes (0.1–1.0 μm, 1.0–2.5 μm, 2.5–5.0 μm and 5.0–10.0 μm). The comparison between observed and simulated data was made to benchmark the model with direct reflectance measurements of snow containing a significant amount of light-absorbing impurities.

2.3.4 Spectral index development

Spectral data collected at different scales (field, UAV and satellite) and modelled data were used to test the possibility of retrieving the presence of MD in snow. To achieve this goal, a set of linear and nonlinear Ordinary Least Squares (OLS) regressions were performed between algebraic combination of reflectance in specific wavelengths and MD concentration measured at each sampling area. The algebraic combination used for the spectral index is widely used to enhance differences in the reflectance of surfaces: it can be expressed in the form of a normalized ratio, as for example the Normalized Difference Snow Index [*Hall et al.*, 1995], for snow classification.

The choice of the values of the two wavelengths was performed according to *Hansen and Schjoerring*, [2003] and *Fava et al.* [2009], where all possible combinations of wavelengths are explored. Then the spectral bands are chosen by looking for "hot spots" in the correlation heat map. The method was applied both on observed spectra collected with the ASD spectrometer and the spectra simulated with the SNICAR model [*Flanner et al.*, 2007].

2.3.5 Radiative forcing calculation

Instantaneous RF (iRF) refers to an instantaneous change in net (down minus up) radiative flux (shortwave plus long wave, in W/m^2) due to an imposed change [*Myhre et al.*, 2013]. We refer herewith to iRF at Top of Surface (TOS) as the net change in upwelling irradiance due to the deposition of light-absorbing impurities in snow.

The iRF is here computed using a simple method based on field measurements of spectral irradiance *E(λ)* (W m^{-2} nm^{-1}), calculated from observed radiance L(λ) (W m^{-2} sr^{-1} nm^{-1}), using the formula *E(λ)* =π*L(λ) therefore assuming a Lambertian spectral response of snow. The method consists of calculating the spectral difference between the irradiance of "pure" snow $E_{ps}(\lambda)$ and the irradiance of a snow containing light-absorbing impurities $E_{MD}(\lambda)$, and then calculating the integrated instantaneous RF (iiRF) across the range from 350 to 850nm. In formula, it can be expressed as:

$$iiRF = \sum_{350nm}^{850nm} iRF(\lambda)\Delta\lambda = \sum_{350nm}^{850nm} E_{ps}(\lambda) - E_{MD}(\lambda)\Delta\lambda$$

The method is similar to that proposed by *Painter et al.* [2012b], but it differs from that since it does not depend on simulations of the spectral reflectance of snow. Although very simple, our method relies on the availability of snow cover with different concentration of MD and "pure" snow patches. This represents a limitation in the applicability in vast areas, but allows direct observation of iRF values to compare with satellite observations and radiative transfer model simulations.

2.4 Results & discussion

2.4.1 Mineral dust determination

MD concentrations determined by Coulter Counter (CC) and through the gravimetric method (GM) are reported for each sample in Table 1. The marked difference between the two methods can be ascribed to the different size intervals of the two

measurements: CC techniques measured only particles between 1 and 30 micron, while the GM method measured bulk particle weight.

ID	C1	C2	C3	DS1	DS2	DS3	DS4	DS5	DS6	DS7
MD ppm (CC)	0.9	0.8	1	84	54.6	29	57	76	107	39
MD ppm (GM)	2.9	3.7	3	198	154	231	132	295	325	/

Table 1 Concentration of MD for the control (C1-3) and the dust sample (DS1-7) determined with the Coulter Counter (CC) and the Gravimetric Method (GM). Notice that Sample 7 (DS7) was damaged during transportation to the laboratory.

Size distribution of fine particles determined by CC (an example in Figure 3) showed log-normal features with a main mode peaking at circa 7 µm on average. This can be considered the mode of MD transported from North Africa. Another mode is present in both samples and controls, starting at 18-20 µm. This coarse distributions are often associated with local transport of large particles produced by anthropic activity and/or local soil erosion, but a remote origin cannot be excluded [*Jeong et al.*, 2014].

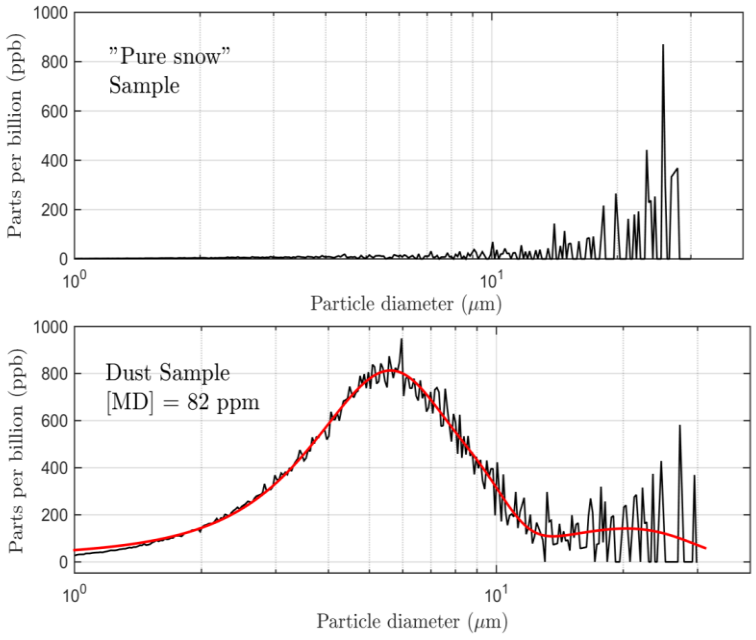

Figure 3 Size distribution of dust particles for a control sample (upper panel) and a snow sample containing 84 ppm of MD (lower panel). The red line depicts a lognormal fit of the main distribution (R^2 = 0.92) (Note that the abscissa is represented in a logarithmic scale in both plots)

2.4.2 Field spectral data and RT model

Examples of reflectance spectra collected with the ASD field spectrometer at each sampling area are shown in Figure 4a. The presence of MD strongly decreases the albedo in the visible wavelengths, in particular from 350 to 800 nm. Beyond 800 nm the effect of MD is negligible, since in this wavelength range the impact of snow grain size is major [*Warren*, 1982]. This is in agreement with the simulation analysis conducted with the SNICAR model. Figure 5 shows examples of the Hemispherical Albedo simulated at different concentrations of MD (left panel) and different snow grain size (right panel). The plots point out the different effect of MD (size class from 5 to 10 µm) and grain size, in particular the effect of MD is concentrated approximately between 350 and 1000 nm, while the effect of increasing grain size is observed for larger wavelengths, above 1000 nm.

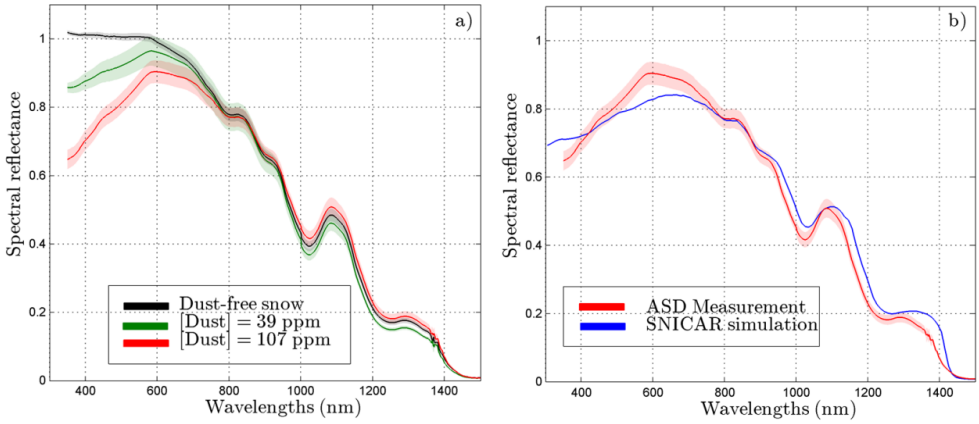

Figure 4 Left panel: measured spectral reflectance (ASD Field Spec) for a control (C1) and two dust samples (DS6 and DS7). Right panel: comparison between observed (red line) and simulated (blue line) reflectance (SNICAR model) for the sample DS6. In both plots, shaded areas represent the standard deviation

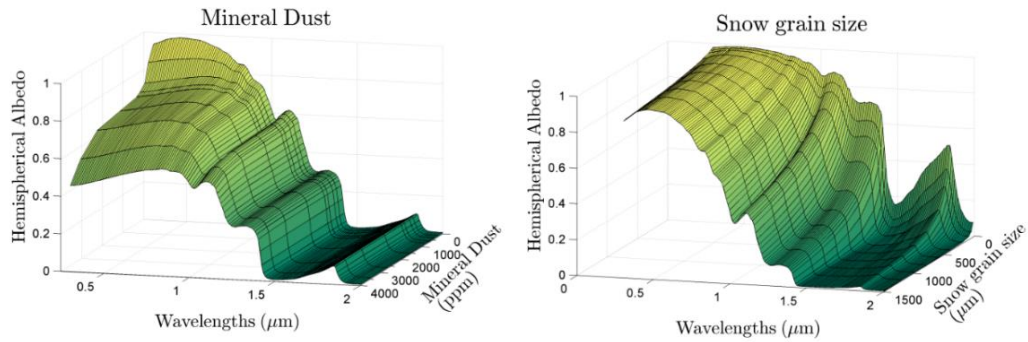

Figure 5 Snow hemispherical albedo simulated with the SNICAR model [Flanner et al., 2007]. Left panel: SNICAR model was run varying MD concentration from 0 to 4000 ppm (size class: 5.0–10.0 µm). Right panel: SNICAR model was run varying snow grain size

The presence of MD in snow decreases its albedo in the visible wavelengths up to 40% for Sample 6 which contains the major MD mass (CC: 107.4 ppm and GM: 325 ppm). Despite still few papers show observed reflectance spectra just after natural depositions of impurities, our data showed to be consistent with observation of MD on snow in literature (*e.g.* [*Painter et al.*, 2007]). Conversely, marked differences were found with respect to spectra of BC on snow (i.e. *Hadley and Kirchstetter* [2012]), since in that case the decrease in albedo is more homogeneous among visible spectrum. Comparisons with the SNICAR simulations (Figure 4b) show that the model slightly underestimates the effect of MD for visible wavelengths, in particular between 350 and 420 nm, and it overestimates the effect from 420 to 800 nm. The deviation between observed and simulated reflectance may be due to the upper boundary of SNICAR in particle dimension. In fact, even particles larger than 10 µm can in principle affect snow albedo by magnifying the absorption in visible wavelengths. This is not taken into account in the model formulation. In this respect, the difference between the MD concentration determined between the GM and CC indicated the presence of MD particles beyond the size-range of the CC, as reported also in literature [*Katra et al.*, 2014]. This allows us to

propose a first explanation regarding the SNICAR deviations with respect to the measured spectra.

Another possible source of mismatch between observed and simulated spectra is the different physical variable represented. In fact, the collection of measurements with a bare optical fiber implies observing an Hemispherical Conical Reflectance (HCR) [*Schaepman-Strub et al.*, 2006], while the SNICAR model simulates a Bi-Hemispherical Reflectance (BHR). This can, in principle, affect a complete overlapping of the two reflectance.

In some cases, reflectance exceeded the value of 1 and it was impossible to compare observed and simulated data. This feature has often been found in literature [*Painter and Dozier*, 2004; *Schaepman-Strub et al.*, 2006; *Carmagnola et al.*, 2013] and was ascribed to the bidirectional effect that often occurs in surfaces such as snow [*Giardino and Brivio*, 2003; *Painter and Dozier*, 2004; *Schaepman-Strub et al.*, 2006]. However, as reported in literature, we do not expect this feature to affect the possibility of calculating spectral indices from the reflectance, in particular for indices that operate in visible wavelengths where the bidirectional effect is more homogeneous [*Painter and Dozier*, 2004].

2.4.3 Definition of the Snow Darkening Index (SDI)

A nonlinear model (rational polynomial fitting) was chosen to account for the saturation effect in the decreasing of the albedo observed during the preliminary sensitivity analysis of the SNICAR simulations. Various linear and nonlinear models were applied to fit the simulated and observed data, but rational fitting produced the best results in terms of R^2. Furthermore, regarding SNICAR simulations, a rational model better approximated the dependence of SDI on MD concentration (Figure 8c). The model structure can be expressed in formula:

$$f(x) = \frac{p_1 x + p_2}{x + q_1}$$

Where p_1, p_2 and q_1 are the parameters of the model and x represents the concentration of MD obtained from the Coulter Counter determination.

From Figure 6 it is possible to identify which wavelength combination generates the hot spot of highest correlation. Although different hot spots are displayed, we selected red (from 640 to 670 nm) and green (from 550 to 590 nm) wavelengths because they are spectral channels typically integrated in satellite sensors, they allow good applicability of the spectral index and they are not influenced by snow grain size but enhance a spectral feature of MD in snow.

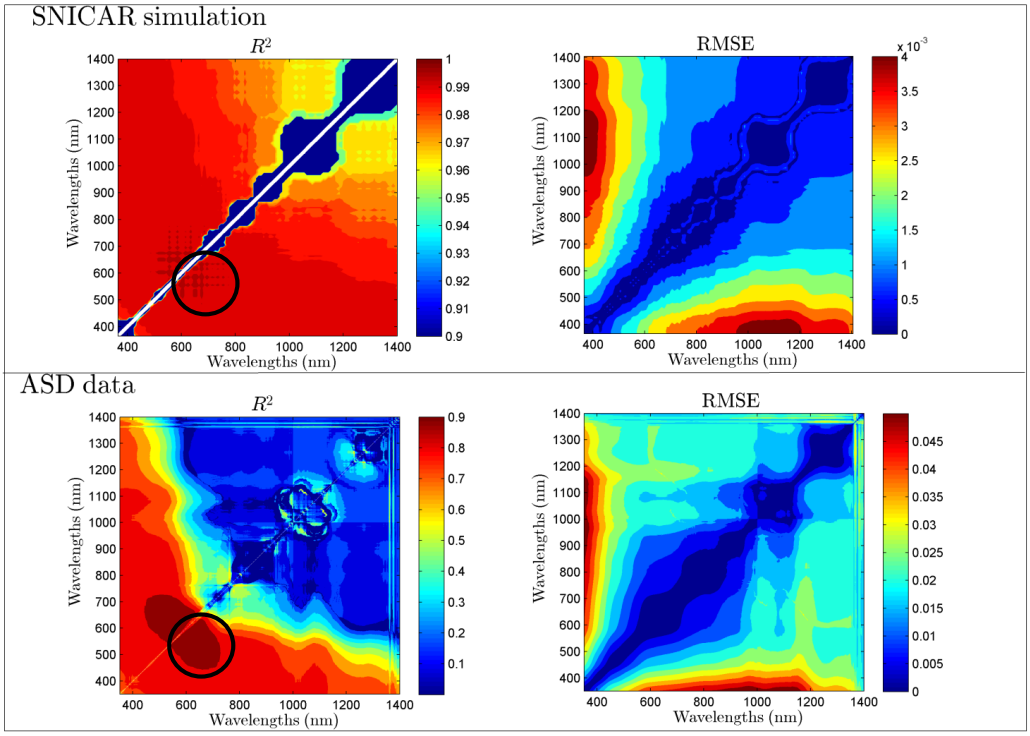

Figure 6 Upper panel: correlation heat map of R^2 and Root Mean Square Error (RMSE) resulting from nonlinear Ordinary Least Squares (nOLS) between SNICAR simulated reflectance and MD concentration of samples (determined with CC). Lower panel: correlation heat map of R^2 and RMSE resulting from nOLS between ASD reflectance and MD concentration (determined with CC)

This correlation hot spot was found both in the measured and simulated data sets. The SDI was then formalized as follows:

$$SDI = \frac{\rho(640;670\text{nm}) - \rho(550;590\text{nm})}{\rho(640;670\text{nm}) + \rho(550;590\text{nm})}$$

In Figure 7a we show the best model obtained from the set of nonlinear Ordinary Least Squares (nOLS) regressions between MD concentration using the CC method and combination of reflectance collected with the ASD spectrometer in the 10 sampling areas at the Artavaggio plains. In Figure 7b we show the linear regression between the Snow Darkening Index (SDI) calculated from the ASD data and from the SNICAR simulated data. The correlation between the data (R^2 = 0.86) means that, despite some differences found between observed and simulated spectra (Section 4.2), the SDI is able to capture the overall variability in MD concentration from different source of data. To validate the hypothesis that large particles (i.e. diameter >30 μm) also affect snow albedo, we calculated the differences between the Gravimetric Method (GM) and the Coulter Counter (CC) measurements, which reflect the amount of large particles among snow samples. Then we calculated the correlation between this difference and the difference of SDI calculated from the ASD band and from the SNICAR model. The nonlinear correlation found in data (rational fit, R^2 = 0.95) states that as the concentration of large particles increases, the deviation between observed and simulated SDI first increases and then shows a saturation effect.

Clearly, SDI and integrated snow broadband albedo have a linear inverse correlation (data not shown) and it is important to underline that SDI is built on a spectral feature of MD in snow. As a consequence, a decrease in albedo due to increasing grain size in snow without MD will not affect SDI values but will, nevertheless, decrease snow albedo.

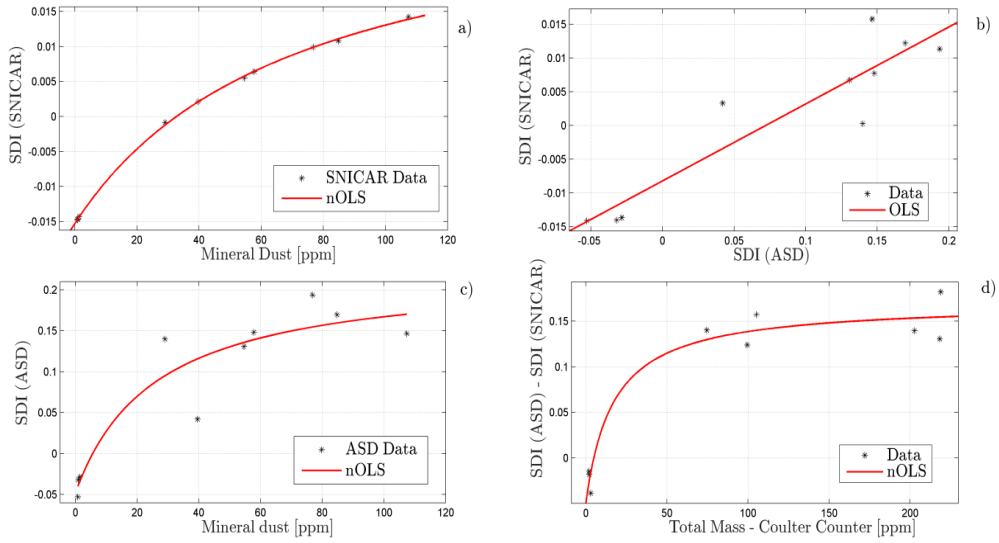

Figure 7 Nonlinear OLS regression between MD concentration and SDI values calculated from SNICAR simulations (7a). Linear OLS regression between the SDI calculated from observed ASD data and simulated SNICAR data (7b). Nonlinear OLS regression (rational fit) between MD concentrations obtained with the Coulter Counter (CC) versus the Snow Darkening Index (SDI) calculated on the hyperspectral data collected with the ASD spectrometer (7c). Nonlinear OLS regression between the differences of MD concentration obtained from GM and CC method, versus the differences of the SDI calculated from SNICAR and observed with the ASD radiometer (7c).

Table 2 shows a review of the model structures and goodness of fit in terms of coefficient of determination (R^2), adjusted coefficient of determination (R^2_{adj}), Root Mean Square Error (RMSE) and Sum Square Error (SSE).

Figure 8 shows the combined effect on SDI of increasing MD concentration and snow grain size using the simulations from the SNICAR model. A global spline interpolator was applied for representation purposes. The interaction of increasing MD concentration and increasing of individual snow grain size causes an amplified effect on snow albedo and hence on SDI values. It is well known that light-absorbing impurities cause an increase in snow grain size due to enhanced absorption [*Warren and Wiscombe*, 1980; *Meinander et al.*, 2014]; because of this feature, the two effects are very difficult to separate and SDI showed a nonlinear response to grain size increase in snow containing MD (Figure 9).

Variables	Type of fit	Model structure	R^2	R^2_{adj}	RMSE	SSE
MD vs. SDI (ASD)	Rational	$f(x) = \frac{p_1 x + p_2}{x + q_1}$	0.87	0.84	0.037	0.009
SDI (ASD) vs. SDI (SNICAR)	Linear	$f(x) = p_1 x + p_2$	0.86	0.84	0.005	0.002
MD (CC) vs. SDI (SNICAR)	Rational	$f(x) = \frac{p_1 x + p_2}{x + q_1}$	0.99	0.99	0.00025	4.557e-07
SDI (ASD) vs. SDI (UAV)	Linear	$f(x) = p_1 x + p_2$	0.83	0.81	0.006	0.001
GM-CC vs. SDI (ASD)-SDI (SNICAR)	Rational	$f(x) = \frac{p_1 x + p_2}{x + q_1}$	0.95	0.94	0.022	0.003

Table 2 Review of the model structure and goodness of fit in terms of coefficient of determination (R^2), adjusted coefficient of determination (R^2_{adj}), Root Mean Square Error (RMSE) and Sum Square Error (SSE) of the plots shown in Figures 7 and 11.

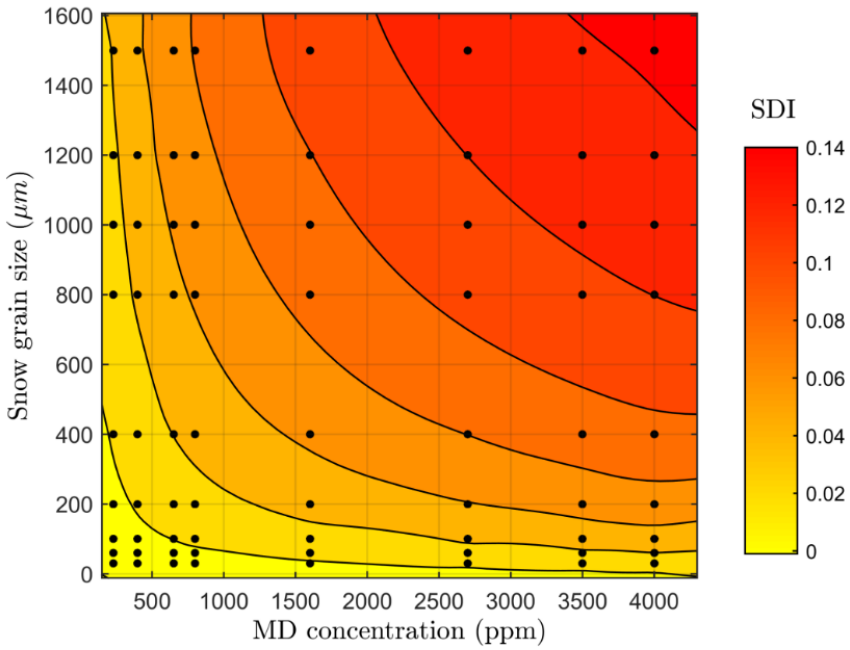

Figure 8 Representation of the SDI index as a function of Mineral Dust (MD) concentration (ppm) and snow grain size (μm). Black dots are obtained from SNICAR simulation and colored facets are a global spline interpolator applied for representation purposes.

2.4.4 RF estimation

An example of the Radiative Forcing (RF) computed at the Artavaggio site for two sampling areas containing 39 ppm and 107 ppm of MD measured with the CC method is shown in Figure 9. The left panel shows the upwelling spectral irradiances (W/m^2) of three plots (one control, C1, and two dust samples, DS6 and DS7) measured with the ASD spectrometer. The spectral difference (*i.e.* the instantaneous RF) between these two irradiances represents a direct proxy of the amount of solar radiation absorbed in the snowpack due to the present of MD deposition. The integration of the iRF between 350 and 850 nm gives the integrated instantaneous RF (iiRF) in W/m^2, which was estimated as equal to 103.2 W/m^2 for the DS with 39 ppm and 153.9 W/m^2 for the DS with 107ppm. We also show the spectral dependence of iRF. In particular, we observed that the iRF increases from 350 to 450 nm and then decreases in longer wavelengths, reaching approximately zero at 1000 nm. This spectral dependence is very specific for the MD impact on snow radiative properties. Possible difficulties in the application of this method lie in the choice of the sampling areas in which to measure the spectral irradiance and the availability of adjacent snow patches with comparable slope and aspect showing different concentrations of impurities. Previous works [*Painter et al.*, 2012b, 2013b; *Kaspari et al.*, 2014, 2015], found similar values for iiRF of light-absorbing impurities in snow. We remark that MD has a strong positive forcing effect when deposited on snow. The instantaneous RF from MD can be higher than that generated by BC depositions on snow, as recently suggested by *Kaspari et al.* [2014] from a modeling approach in the Himalayan region. Still a lot of uncertainties exist regarding the RF of BC and MD in snow. A critical point regards methodologies followed by different authors; they should be unified in order to effectively compare results from different observational and simulation studies.

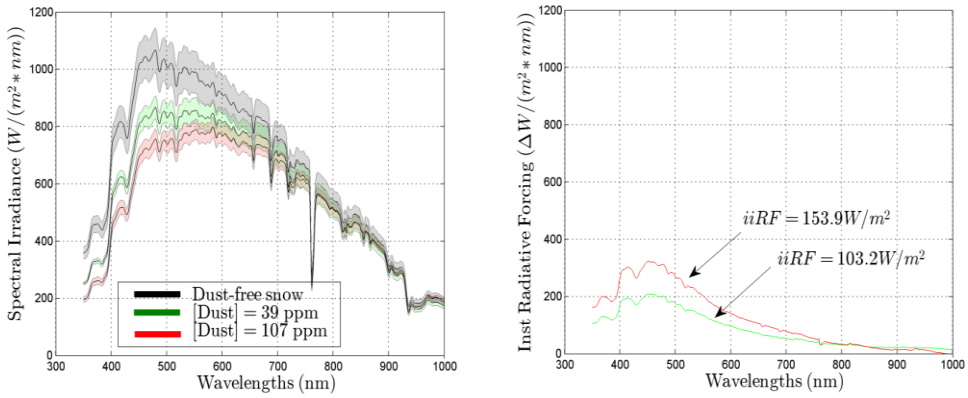

Figure 9 Left panel: Spectral irradiances of the sample containing 0.92ppm of MD (black line), snow containing 39 ppm (green line) and 107 ppm (red line) of MD. Right panel: Instantaneous radiative forcing iRF(λ) of snow containing different concentrations of MD. The samples are the same showed in Figure 4.

The amount of solar radiation absorbed in the snowpack because of the presence of MD can be directly thermalized through the media enhancing its temperature. If no new snowfall occurs, this process can significantly accelerate the melting of snow [*Painter et al.*, 2010], anticipating snow retreat in mountain areas, altering local radiative balance and shifting vegetation phenology. Furthermore, the well-known snow-albedo feedback [*Hansen and Nazarenko*, 2004] can here operate in the following way: as the snow melt is increased by the presence of MD, the MD itself is concentrated by the melting in nearly flat areas in mountain regions. In this study, we present only an instantaneous view of the process. During the 2013-2014 winter, the European Alpine area experienced intense snowfalls; in this way, the radiative effect of MD may be damped by the presence of fresh snow above the MD layers. But during the melting season, the MD layers re-emerge and enhance the absorption of solar radiation. This process may also affect also underling ice in the accumulation zone of Alpine mountain glaciers.

2.4.5 Snow Darkening Index (SDI) applications

The RGB Digital Numbers (DN) of the camera onboard the UAV were algebraically combined to reproduce the SDI index as follows: (DN(Red)-DN(Green))/(DN(Red)+DN(Green)). The

values of SDI estimated from UAV were then compared to those observed from the ground using the ASD spectrometer.

Atmospherically and topographically corrected Landsat OLI Top Of Surface (TOS) reflectances in Band 3 (0.525 - 0.600 µm) and Band 4 (0.630 - 0.680 µm) were also algebraically combined to calculate the SDI index as follows:

$$(\rho(B4_{TOS}) - \rho(B3_{TOS}))/\ (\rho(B4_{TOS}) + \rho(B3_{TOS})).$$

SDI values were calculated only in those areas covered by snow and ice. The classes were produced using a supervised classification approach (Maximum Likelihood) of the 9 OLI bands. The classification was applied only in mountain areas of the Landsat tile using the three training classes: snow, vegetation, urban.

Once the SDI map was created, it was classified in terms of exposure of the slopes (8 classes: NNE, EEN, EES, SSE, SSW, WWS, WWN, NNW) using the ASTER GDEM, to analyze whether South facing slopes were more impacted by the MD transport because of enhanced melting due to higher solar irradiance.

Figure 10 shows the SDI map derived from UAV data on the Artavaggio plains. Spatial variability of dust patches is clearly visible in the RGB orthomosaic (Figure 10) and it is enhanced in the SDI map. The map shows both fresh and re-emerging layers of MD in snow and represents a simple way to detect MD depositions in snow by exploiting the different reflectance in visible channels. The map shows a south-facing slope where the concentrations of impurities in snow are naturally higher in the Northern Hemisphere because of the longer exposition to direct solar radiation. This indicates that slope morphology plays an important role in enhancing or dampening the effect of MD on snow albedo. In fact, small basins in high altitude areas can increase the concentration of MD in snow during the melting season, thus accelerating the nonlinear response of snow. Possible influence of other light absorbing impurities (e.g. BC) are not tested here

since we focused on MD, but they may be contributing to the overall reduction of reflectance.

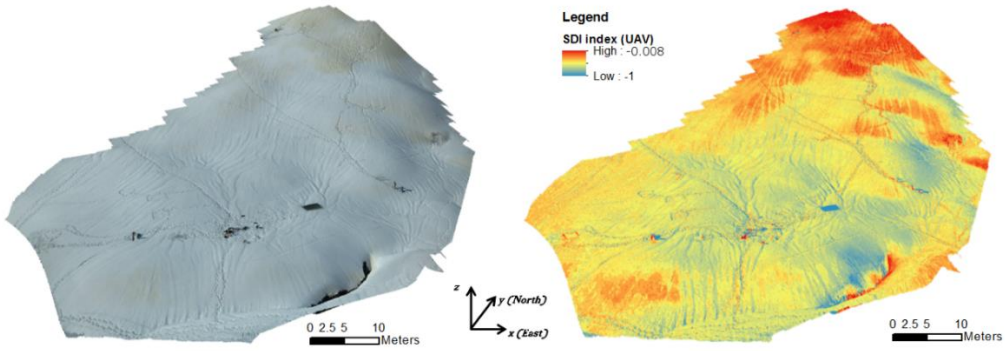

Figure 10 Left panel: Orthomosaic of UAV-RGB data for the first flight draped on the Digital Surface Model (DSM) of the area. Right panel: maps SDI index calculated as the normalized ratio between the Red and Green channel of the Canon s100.

Figure 11 shows the linear regression (R^2 = 0.83) between the SDI calculated in each sampling area of the UAV orthomosaic and the SDI calculated from ASD spectra. We found a linear correlation that assesses the possibility of calculating the SDI also from RBG images to spatially represent MD deposition in snow. SDI values calculated from UAV and ASD data differ more than an order of magnitude, this feature is due to the fact that SDI from UAV was calculated combining raw DN values of the RGB images.

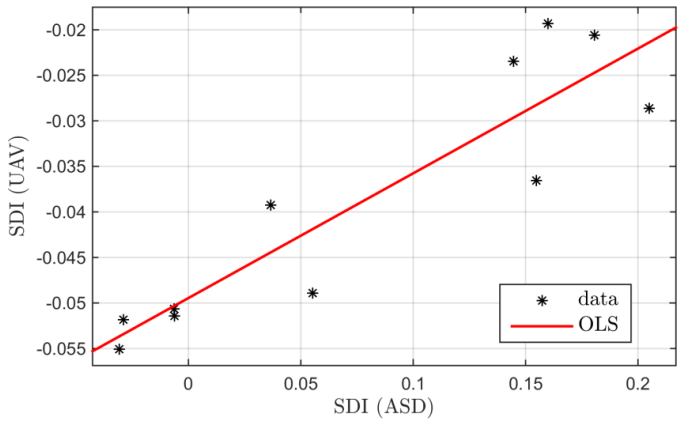

Figure 11 Linear OLS regression between the SDI calculated from ASD data and from UAV data (R^2=0.83) at each sampling area of the Artavaggio plains

Results from the SDI calculation on Landsat OLI bands are shown in Figures 12-13. Figure 12 shows the Landsat image and the SDI map (12a) of the Artavaggio plains. The black polygon in the maps represents the area covered by the UAV survey. The coarse resolution of the Landsat image (30 m) does not allow the entire capture of all the spatial variability of MD due to snow micromorphology as compared with the UAV resolution (Figure 10), although some spatial variability of SDI is still visible in Landsat data. In Figure 13, a larger area within the Central European Alps is examined. The presence of MD in snow is visible from the Landsat true color representation (Figure 13a) and it is well represented in the SDI map, which reveals portions of lower and higher MD deposition differently located in the catchment.

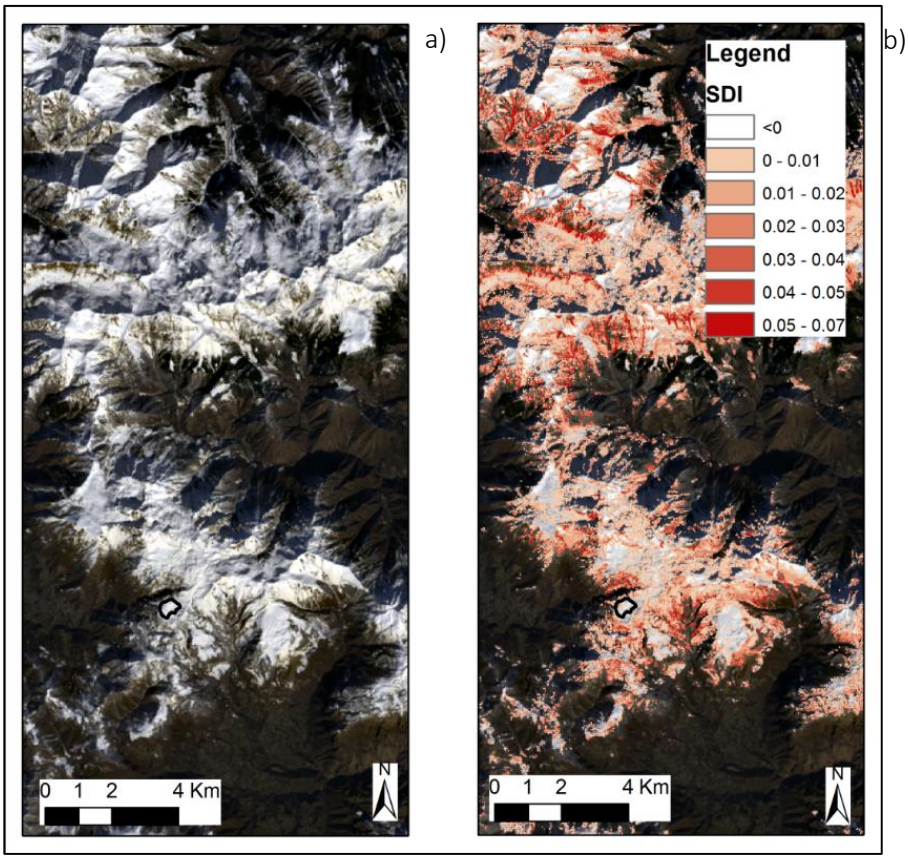

Figure 12 Landsat 8 image (a) and SDI map (b) of the Artavaggio plains. Black polygon in the maps represents the area covered by the UAV survey

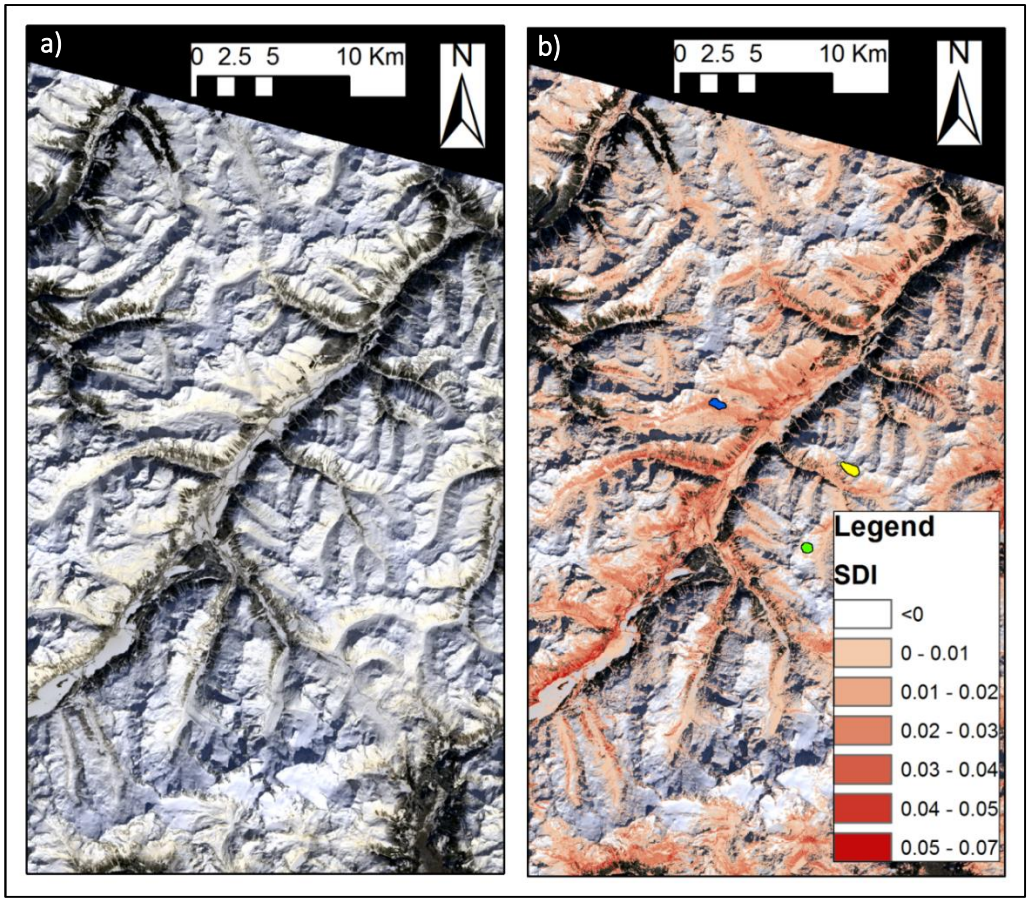

Figure 13 Landsat 8 OLI image (a) and SDI maps (b) of the Central European Alps. Three Regions Of Interest (ROI) showing different values of SDI were selected in the Engadine region (Switzerland). ROI color legend: Blue: ROI-2, Yellow: ROI-1, Green: ROI-0

Figure 14 shows the frequency distribution of the SDI index in South South-East (SSE) and in the North North-West (NNW) classes of slope exposure for the mountain area within the Landsat tile. SDI assumes higher values in SSE slopes with respect to NNW slopes. Since the image was topographically corrected using the ATCOR code, the effect of shadows does not influence SDI values. The separation of the two distributions shows that also in this case south-facing slopes have, on average, higher SDI values, suggesting that both the provenance of the MD plume and longer exposition to solar radiation manifest their effects at different scales. Similar pattern was observed in broadband albedo and RF values in Colorado [*Painter et al.*, 2013b], where lower RF values were

found in the high north facing cirques where less direct radiation slow the metamorphism of snow; higher RF values were found on southeast facing slopes at the lowest elevations.

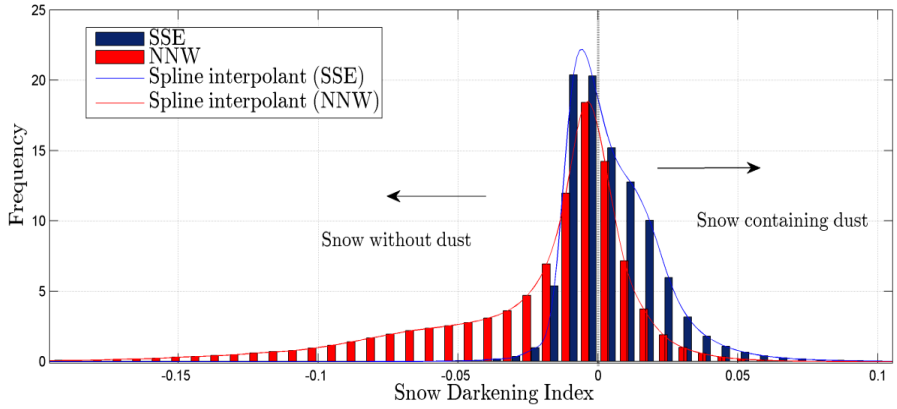

Figure 14 Frequency distribution of SDI for the Central European Alps classified in class of slope exposition: South South-East (SSE) and North North-West (NNW). The histograms show that south-facing slopes have higher SDI values than the north-facing slopes.

In the upper-left region of the Central European Alps (Engadina, Switzerland), we selected three Regions Of Interest (ROIs) showing different SDI values comparable with those observed in the study area: from low (ROI-0) to medium (ROI-1) and high (ROI-2) SDI values. For each ROI, we extracted the mean and standard deviation of reflectance from the Landsat image. In Figure 15 we show the spectra of atmospherically-topographically corrected reflectance for the three ROIs, overlapped with SNICAR simulations that showed similar SDI values. Although Landsat has a lower spectral resolution of Landsat with respect to that of the SNICAR, the plot from ROI 0 shows a good agreement between observed and simulated reflectance. The plot from ROI 1 shows an offset between the reflectances, and the plot from ROI 2, shows a behavior similar to that observed between ASD and SNICAR reflectance (Figure 4b). In fact, the SNICAR model also in this case slightly underestimates the effect of MD on snow reflectance for wavelengths lower than 600 nm.

To be noted is that also for the Landsat spectra we found reflectance values that exceeded the value of 1, thus confirming the feature reported in previous literature [*Painter and Dozier*, 2004; *Schaepman-Strub et al.*, 2006; *Carmagnola et al.*, 2013; *Pope and Rees*, 2014] and ascribed to the strong forward scattering of snow.

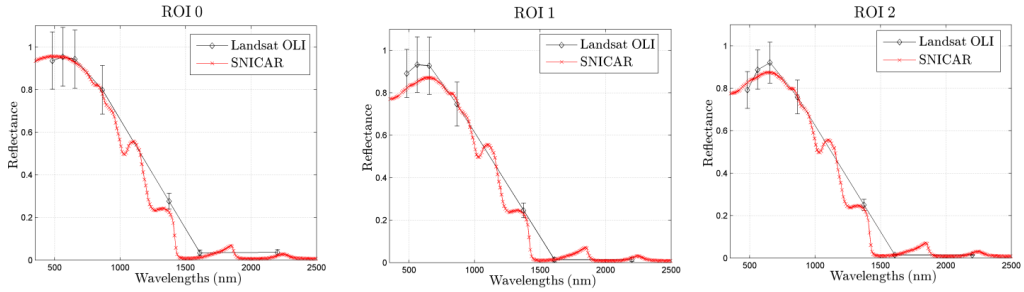

Figure 15 Comparison between Landsat and SNICAR reflectance for the three Regions Of Interest (ROI) shown in Figure 10

2.5 Conclusions

In this paper, we propose a simple methodology for mapping light-absorbing impurities such as Mineral Dust (MD) in snow using optical data that range from hyperspectral sensor to multispectral and RGB images. We developed the method through a field campaign aimed at quantifying the actual impact of MD on snow albedo after a significant MD transport that reached the European Alps from the Saharan desert during the spring of 2014. We compared high resolution reflectance spectra (collected with an ASD Field Spectrometer) with reflectance simulated by parameterizing a physically-based radiative transfer model (SNICAR). Differences between observed and simulated data were ascribed to the effect of particles with diameters above 30 µm that are not included in the SNICAR model but nevertheless can increase light absorption. Using the hot spots method it was possible to find a model based on maximization of the coefficient of regression (R^2) and minimization of the Root Mean Squared Error (RMSE). Through these rules it was found that the normalized ratio between red and green wavelengths (the Snow Darkening Index, SDI) is highly correlated with the MD

concentration. We claim that this may help to gain reasonable estimates of light-absorbing impurities, such as MD, in snow.

Multiscale observations with an Unmanned Aerial Vehicle (UAV) and Landsat OLI satellite sensor showed a significant impact of MD on snow albedo. This allowed us to spatially represent the SDI at local and regional scale in the European Alps. The wide applicability of the SDI will allow mapping of past events of MD deposition on snow from different sensors that ranges from airborne and terrestrial digital cameras (i.e. Dumont et al., 2011) to different satellite sensors (Landsat, MODIS *etc.*), generating, for example, SDI time series to study post-depositional dynamics of MD on snow and ice.

Furthermore, we propose a simple method to estimate instantaneous Radiative Forcing (iRF) of MD in snow, based on the difference between spectral irradiances of pure snow and snow containing a significant amount of MD. Our iRF estimations are comparable with those found in previous literature and represent an opportunity to directly estimate iRF from field spectral measurements, which is very useful for validating GCM and radiative transfer models.

The impact of light-absorbing impurities on snow radiative properties represents an active field of research in atmosphere and cryosphere sciences, with many uncertainties in model simulations. Our results show the first evidence that MD strongly impacts snow reflectance in European Alps, where Saharan MD events are very frequent in the spring season. Furthermore, climate change is known to alter meteo-climatic patterns (e.g. North Atlantic Oscillation, NAO), eventually leading to stronger and more frequent MD transport toward the European Alpine chain, and this may result in an early snowmelt and variations in local radiative balances.

Acknowledgements:

This chapter was developed within the SINOPIAE project funded by the Regione Lombardia. A published version can be found in:

Di Mauro, B., F. Fava, L. Ferrero,R. Garzonio, G. Baccolo, B. Delmonte, and R. Colombo (2015), Mineral dust impact on snow radiative properties in the European Alps combining ground, UAV, and satellite observations, *J. Geophys. Res. Atmos*., 120, doi:10.1002/2015JD023287

I wish to thank C. Giardino (CNR-IREA) for lending the ASD-Field Spec and for help with Landsat 8 topo-atmospheric correction with ATCOR. Furthermore, I acknowledge the Aermatica team, S. Cogliati, M. Fagnani, E. Bolzacchini and M. Casati for their help in organizing the field campaign.

Bibliography

Albani, S., N. M. Mahowald, A. T. Perry, R. A. Scanza, C. S. Zender, N. G. Heavens, V. Maggi, J. F. Kok, and B. L. Otto-Bliesner (2014), Improved dust representation in the Community Atmosphere Model, *J. Adv. Model. Earth Syst.*, n/a–n/a, doi:10.1002/2013MS000279.

Aoki, T., K. Kuchiki, M. Niwano, Y. Kodama, M. Hosaka, and T. Tanaka (2011), Physically based snow albedo model for calculating broadband albedos and the solar heating profile in snowpack for general circulation models, *J. Geophys. Res.*, *116*(D11), D11114, doi:10.1029/2010JD015507.

Basart, S., C. Pérez, S. Nickovic, E. Cuevas, and J. M. Baldasano (2012), Development and evaluation of the BSC-DREAM8b dust regional model over Northern Africa, the Mediterranean and the Middle East, *Tellus B*, *64*, doi:10.3402/tellusb.v64i0.18539.

Bauer, E., and a. Ganopolski (2014), Sensitivity simulations with direct shortwave radiative forcing by aeolian dust during glacial cycles, *Clim. Past*, *10*(4), 1333–1348, doi:10.5194/cp-10-1333-2014.

Berk, A., L. S. Bernstein, and D. C. Robertson (1989), *MODTRAN: A Moderate Resolution Model for LOWTRAN 7*.

Bond, T. C. et al. (2013), Bounding the role of black carbon in the climate system: A scientific assessment, *J. Geophys. Res. Atmos.*, *118*(11), 5380–5552, doi:10.1002/jgrd.50171.

Brandt, R. E., S. G. Warren, and A. D. Clarke (2011), A controlled snowmaking experiment testing the relation between black carbon content and reduction of snow albedo, *J. Geophys. Res.*, *116*(D8), D08109, doi:10.1029/2010JD015330.

Bryant, A. C., T. H. Painter, J. S. Deems, and S. M. Bender (2013), Impact of dust radiative forcing in snow on accuracy of operational runoff prediction in the Upper Colorado River Basin, *Geophys. Res. Lett.*, *40*(15), 3945–3949, doi:10.1002/grl.50773.

Carmagnola, C. M. et al. (2013), Snow spectral albedo at Summit, Greenland: measurements and numerical simulations based on physical and chemical properties of the snowpack, *Cryosph.*, *7*(4), 1139–1160, doi:10.5194/tc-7-1139-2013.

Claquin, T. et al. (2003), Radiative forcing of climate by ice-age atmospheric dust, *Clim. Dyn.*, *20*(2-3), 193–202, doi:10.1007/s00382-002-0269-1.

Clarke, A. D., and K. J. Noone (1985), Soot in the Arctic snowpack: a cause for perturbations in radiative transfer, *Atmos. Environ.*, *19*(12), 2045–2053, doi:10.1016/0004-6981(85)90113-1.

Conway, H., A. Gades, and C. F. Raymond (1996), Albedo of dirty snow during conditions of melt, *Water Resour. Res.*, *32*(6), 1713–1718, doi:10.1029/96WR00712.

Dagsson-Waldhauserova, P., O. Arnalds, H. Olafsson, J. Hladil, R. Skala, T. Navratil, L. Chadimova, and O. Meinander (2015), Snow–Dust Storm: Unique case study from Iceland, March 6–7, 2013, *Aeolian Res.*, *16*, 69–74, doi:10.1016/j.aeolia.2014.11.001.

De Angelis, M., and A. Gaudichet (1991), Saharan dust deposition over Mont Blanc (French Alps) during the last 30 years, *Tellus B*, *43*(1), doi:10.3402/tellusb.v43i1.15246.

Delmonte, B., J. Petit, and V. Maggi (2002), Glacial to Holocene implications of the new 27000-year dust record from the EPICA Dome C (East Antarctica) ice core, *Clim. Dyn.*, *18*(8), 647–660, doi:10.1007/s00382-001-0193-9.

Doherty, S. J., C. Dang, D. A. Hegg, R. Zhang, and S. G. Warren (2014), Black carbon and other light-absorbing particles in snow of central North America, *J. Geophys. Res. Atmos.*, *119*(22), 12,807–12,831, doi:10.1002/2014JD022350.

Dumont, M., P. Sirguey, Y. Arnaud, and D. Six (2011), Monitoring spatial and temporal variations of surface albedo on Saint Sorlin Glacier (French Alps) using terrestrial photography, *Cryosphere*, *5*, 759–771, doi:10.5194/tc-5-759-2011.

Dumont, M., E. Brun, G. Picard, M. Michou, Q. Libois, J.-R. Petit, M. Geyer, S. Morin, and B. Josse (2014), Contribution of light-absorbing impurities in snow to Greenland's darkening since 2009, *Nat. Geosci.*, *7*(7), 509–512, doi:10.1038/ngeo2180.

Fava, F., R. Colombo, S. Bocchi, M. Meroni, M. Sitzia, N. Fois, and C. Zucca (2009), Identification of hyperspectral vegetation indices for Mediterranean pasture characterization, *Int. J. Appl. Earth Obs. Geoinf.*, *11*(4), 233–243, doi:10.1016/j.jag.2009.02.003.

Field, J. P., J. Belnap, D. D. Breshears, J. C. Neff, G. S. Okin, J. J. Whicker, T. H. Painter, S. Ravi, M. C. Reheis, and R. L. Reynolds (2010), The ecology of dust, *Front. Ecol. Environ.*, *8*(8), 423–430, doi:10.1890/090050.

Flanner, M. G., and C. S. Zender (2005), Snowpack radiative heating: Influence on Tibetan Plateau climate, *Geophys. Res. Lett.*, *32*(6), L06501, doi:10.1029/2004GL022076.

Flanner, M. G., C. S. Zender, J. T. Randerson, and P. J. Rasch (2007), Present-day climate forcing and response from black carbon in snow, *J. Geophys. Res.*, *112*(D11), D11202, doi:10.1029/2006JD008003.

Flanner, M. G., C. S. Zender, P. G. Hess, N. M. Mahowald, T. H. Painter, V. Ramanathan, and P. J. Rasch (2009), Springtime warming and reduced snow cover from carbonaceous particles, *Atmos. Chem. Phys.*, *9*(7), 2481–2497, doi:10.5194/acp-9-2481-2009.

Franzén, L. G., M. Hjelmroos, P. Kållberg, A. Rapp, J. O. Mattsson, and E. Brorström-Lundén (1995), The Saharan dust episode of south and central Europe, and northern Scandinavia, March 1991, *Weather*, *50*(9), 313–318, doi:10.1002/j.1477-8696.1995.tb06139.x.

Gautam, R., N. C. Hsu, W. K.-M. Lau, and T. J. Yasunari (2013), Satellite observations of desert dust-induced Himalayan snow darkening, *Geophys. Res. Lett.*, *40*(5), 988–993, doi:10.1002/grl.50226.

Giardino, C., and P. A. Brivio (2003), The application of a dedicated device to acquire bidirectional reflectance factors over natural surfaces, *Int. J. Remote Sens.*, *24*(14), 2989–2995, doi:10.1080/0143116031000094782.

Goudie, a. S., and N. J. Middleton (2001), Saharan dust storms: nature and consequences, *Earth-Science Rev.*, *56*(1-4), 179–204, doi:10.1016/S0012-8252(01)00067-8.

Hadley, O. L., and T. W. Kirchstetter (2012), Black-carbon reduction of snow albedo, *Nat. Clim. Chang.*, *2*(6), 437–440, doi:10.1038/nclimate1433.

Hadley, O. L., C. E. Corrigan, T. W. Kirchstetter, S. S. Cliff, and V. Ramanathan (2010), Measured black carbon deposition on the Sierra Nevada snow pack and implication for snow pack retreat, *Atmos. Chem. Phys.*, *10*(15), 7505–7513, doi:10.5194/acp-10-7505-2010.

Hall, D. K., G. A. Riggs, and V. V. Salomonson (1995), Development of methods for mapping global snow cover using moderate resolution imaging spectroradiometer data, *Remote Sens. Environ.*, *54*(2), 127–140, doi:10.1016/0034-4257(95)00137-P.

Hansen, J., and L. Nazarenko (2004), Soot climate forcing via snow and ice albedos., *Proc. Natl. Acad. Sci. U. S. A.*, *101*(2), 423–8, doi:10.1073/pnas.2237157100.

Hansen, P. M., and J. K. Schjoerring (2003), Reflectance measurement of canopy biomass and nitrogen status in wheat crops using normalized difference vegetation indices and partial least squares regression, *Remote Sens. Environ.*, *86*(4), 542–553, doi:10.1016/S0034-4257(03)00131-7.

Helmert, J., B. Heinold, I. Tegen, O. Hellmuth, and M. Wendisch (2007), On the direct and semidirect effects of Saharan dust over Europe: A modeling study, *J. Geophys. Res.*, *112*(D13), D13208, doi:10.1029/2006JD007444.

Hodson, A. et al. (2007), A glacier respires: Quantifying the distribution and respiration CO 2 flux of cryoconite across an entire Arctic supraglacial ecosystem, *J. Geophys. Res.*, *112*(G4), G04S36, doi:10.1029/2007JG000452.

Immerzeel, W. W., P. D. A. Kraaijenbrink, J. M. Shea, A. B. Shrestha, F. Pellicciotti, M. F. P. Bierkens, and S. M. de Jong (2014), High-resolution monitoring of Himalayan glacier dynamics using unmanned aerial vehicles, *Remote Sens. Environ.*, *150*, 93–103, doi:10.1016/j.rse.2014.04.025.

Irons, J. R., J. L. Dwyer, and J. A. Barsi (2012), The next Landsat satellite: The Landsat Data Continuity Mission, *Remote Sens. Environ.*, *122*, 11–21, doi:10.1016/j.rse.2011.08.026.

Jacobson, M. Z. (2004), Climate response of fossil fuel and biofuel soot, accounting for soot's feedback to snow and sea ice albedo and emissivity, *J. Geophys. Res.*, *109*(D21), D21201, doi:10.1029/2004JD004945.

Jeong, G. Y., J. Y. Kim, J. Seo, G. M. Kim, H. C. Jin, and Y. Chun (2014), Long-range transport of giant particles in Asian dust identified by physical, mineralogical, and meteorological analysis, *Atmos. Chem. Phys.*, *14*(1), 505–521, doi:10.5194/acp-14-505-2014.

Kaspari, S., T. H. Painter, M. Gysel, S. M. Skiles, and M. Schwikowski (2014), Seasonal and elevational variations of black carbon and dust in snow and ice in the Solu-Khumbu, Nepal and estimated radiative forcings, *Atmos. Chem. Phys.*, *14*(15), 8089–8103, doi:10.5194/acp-14-8089-2014.

Kaspari, S., S. M. Skiles, I. Delaney, D. Dixon, and T. H. Painter (2015), Accelerated Glacier Melt on Snow Dome, Mt. Olympus, Washington, USA due to Deposition of Black Carbon and Mineral Dust from Wildfire, *J. Geophys. Res. Atmos.*, *120*(7), n/a–n/a, doi:10.1002/2014JD022676.

Katra, I., L. Arotsker, H. Krasnov, A. Zaritsky, A. Kushmaro, and E. Ben-Dov (2014), Richness and diversity in dust stormborne biomes at the southeast mediterranean., *Sci. Rep.*, *4*, 5265, doi:10.1038/srep05265.

Kaufman, Y. J., and C. Sendra (1988), Algorithm for automatic atmospheric corrections to visible and near-IR satellite imagery, *Int. J. Remote Sens.*, *9*(8), 1357–1381, doi:10.1080/01431168808954942.

Kutuzov, S., M. Shahgedanova, V. Mikhalenko, P. Ginot, I. Lavrentiev, and S. Kemp (2013), High-resolution provenance of desert dust deposited on Mt. Elbrus, Caucasus in 2009–2012 using snow pit and firn core records, *Cryosph.*, *7*(5), 1481–1498, doi:10.5194/tc-7-1481-2013.

Lawrence, D. M. et al. (2011), Parameterization improvements and functional and structural advances in Version 4 of the Community Land Model, *J. Adv. Model. Earth Syst.*, *3*(3), M03001, doi:10.1029/2011MS000045.

Li, J., G. S. Okin, S. McKenzie Skiles, and T. H. Painter (2013), Relating variation of dust on snow to bare soil dynamics in the western United States, *Environ. Res. Lett.*, *8*(4), 044054, doi:10.1088/1748-9326/8/4/044054.

Lin, G., J. E. Penner, M. G. Flanner, S. Sillman, L. Xu, and C. Zhou (2014), Radiative forcing of organic aerosol in the atmosphere and on snow: Effects of SOA and brown carbon, *J. Geophys. Res. Atmos.*, *119*(12), 7453–7476, doi:10.1002/2013JD021186.

Liou, K. N., Y. Takano, C. He, P. Yang, L. R. Leung, Y. Gu, and W. L. Lee (2014), Stochastic parameterization for light absorption by internally mixed BC/dust in snow grains for application to climate models, *J. Geophys. Res. Atmos.*, *119*(12), 7616–7632, doi:10.1002/2014JD021665.

Lucieer, A., D. Turner, D. H. King, and S. A. Robinson (2014), Using an Unmanned Aerial Vehicle (UAV) to capture micro-topography of Antarctic moss beds, *Int. J. Appl. Earth Obs. Geoinf.*, *27*, 53–62, doi:10.1016/j.jag.2013.05.011.

Maher, B. A., J. M. Prospero, D. Mackie, D. Gaiero, P. P. Hesse, and Y. Balkanski (2010), Global connections between aeolian dust, climate and ocean biogeochemistry at the present day and at the last glacial maximum, *Earth-Science Rev.*, *99*(1-2), 61–97, doi:10.1016/j.earscirev.2009.12.001.

Mahowald, N., S. Albani, J. F. Kok, S. Engelstaeder, R. Scanza, D. S. Ward, and M. G. Flanner (2013), The size distribution of desert dust aerosols and its impact on the Earth system, *Aeolian Res.*, doi:10.1016/j.aeolia.2013.09.002.

Mahowald, N. M., A. R. Baker, G. Bergametti, N. Brooks, R. A. Duce, T. D. Jickells, N. Kubilay, J. M. Prospero, and I. Tegen (2005), Atmospheric global dust cycle and iron inputs to the ocean, *Global Biogeochem. Cycles*, *19*(4), n/a–n/a, doi:10.1029/2004GB002402.

McConnell, J. R., R. Edwards, G. L. Kok, M. G. Flanner, C. S. Zender, E. S. Saltzman, J. R. Banta, D. R. Pasteris, M. M. Carter, and J. D. W. Kahl (2007), 20th-century industrial black carbon emissions altered Arctic climate forcing., *Science*, *317*(5843), 1381–4, doi:10.1126/science.1144856.

Meinander, O. et al. (2014), Brief communication: Light-absorbing impurities can reduce the density of melting snow, *Cryosph.*, *8*(3), 991–995, doi:10.5194/tc-8-991-2014.

Mie, G. (1908), Beiträge zur Optik trüber Medien, speziell kolloidaler Metallösungen, *Ann. Phys.*, *330*(3), 377–445, doi:10.1002/andp.19083300302.

Myhre, G. et al. (2013), 2013: Anthropogenic and Natural Radiative Forcing, in *Climate Change 2013: The Physical Science Basis. Contribution of Working Group I to the Fifth Assessment Report of the Intergovernmental Panel on Climate Change*, pp. 659–740.

Oerlemans, J., R. H. Giesen, and M. R. Van Den Broeke (2009), Retreating alpine glaciers: increased melt rates due to accumulation of dust (Vadret da Morteratsch, Switzerland), *J. Glaciol.*, *55*(192), 729–736, doi:10.3189/002214309789470969.

Painter, T. H., and J. Dozier (2004), Measurements of the hemispherical-directional reflectance of snow at fine spectral and angular resolution, *J. Geophys. Res. Atmos.*, *109*, doi:10.1029/2003JD004458.

Painter, T. H., A. P. Barrett, C. C. Landry, J. C. Neff, M. P. Cassidy, C. R. Lawrence, K. E. McBride, and G. L. Farmer (2007), Impact of disturbed desert soils on duration of mountain snow cover, *Geophys. Res. Lett.*, *34*(12), L12502, doi:10.1029/2007GL030284.

Painter, T. H., J. S. Deems, J. Belnap, A. F. Hamlet, C. C. Landry, and B. Udall (2010), Response of Colorado River runoff to dust radiative forcing in snow., *Proc. Natl. Acad. Sci. U. S. A.*, *107*(40), 17125–30, doi:10.1073/pnas.0913139107.

Painter, T. H., S. M. Skiles, J. S. Deems, A. C. Bryant, and C. C. Landry (2012a), Dust radiative forcing in snow of the Upper Colorado River Basin: 1. A 6 year record of energy balance, radiation, and dust concentrations, *Water Resour. Res.*, *48*(7), n/a–n/a, doi:10.1029/2012WR011985.

Painter, T. H., A. C. Bryant, and S. M. Skiles (2012b), Radiative forcing by light absorbing impurities in snow from MODIS surface reflectance data, *Geophys. Res. Lett.*, *39*(17), n/a–n/a, doi:10.1029/2012GL052457.

Painter, T. H., M. G. Flanner, G. Kaser, B. Marzeion, R. A. VanCuren, and W. Abdalati (2013a), End of the Little Ice Age in the Alps forced by industrial black carbon., *Proc. Natl. Acad. Sci. U. S. A.*, *110*(38), 15216–21, doi:10.1073/pnas.1302570110.

Painter, T. H., F. C. Seidel, A. C. Bryant, S. McKenzie Skiles, and K. Rittger (2013b), Imaging spectroscopy of albedo and radiative forcing by light-absorbing impurities in mountain snow, *J. Geophys. Res. Atmos.*, *118*(17), 9511–9523, doi:10.1002/jgrd.50520.

Pedersen, C. A., J.-C. Gallet, J. Ström, S. Gerland, S. R. Hudson, S. Forsström, E. Isaksson, and T. K. Berntsen (2015), In-situ observations of black carbon in snow and the corresponding spectral surface albedo reduction, *J. Geophys. Res. Atmos.*, n/a–n/a, doi:10.1002/2014JD022407.

Pey, J., X. Querol, a. Alastuey, F. Forastiere, and M. Stafoggia (2013), African dust outbreaks over the Mediterranean Basin during 2001–2011: PM_{10} concentrations, phenomenology and trends, and its relation with synoptic and mesoscale meteorology, *Atmos. Chem. Phys.*, *13*(3), 1395–1410, doi:10.5194/acp-13-1395-2013.

Pope, A., and G. Rees (2014), Using in situ spectra to explore Landsat classification of glacier surfaces, *Int. J. Appl. Earth Obs. Geoinf.*, *27*, 42–52, doi:10.1016/j.jag.2013.08.007.

Prospero, J. M. (2002), Environmental characterization of global sources of atmospheric soil dust identified with the NIMBUS 7 Total Ozone Mapping Spectrometer (TOMS) absorbing aerosol product, *Rev. Geophys.*, *40*(1), 1002, doi:10.1029/2000RG000095.

Reynolds, R. L. et al. (2013), Composition of dust deposited to snow cover in the Wasatch Range (Utah, USA): Controls on radiative properties of snow cover and comparison to some dust-source sediments, *Aeolian Res.*, doi:10.1016/j.aeolia.2013.08.001.

Rhoades, C., K. Elder, and E. Greene (2010), The Influence of an Extensive Dust Event on Snow Chemistry in the Southern Rocky Mountains, *Arctic, Antarct. Alp. Res.*, *42*(1), 98–105, doi:10.1657/1938-4246-42.1.98.

Richter, R. (2007), Atmospheric / Topographic Correction for Satellite Imagery (ATCOR - 2/3 User Guide), *ATCOR-2/3 User Guid. Version 6.3*, (February).

Ruth, U. et al. (2008), Proxies and Measurement Techniques for Mineral Dust in Antarctic Ice Cores, *Environ. Sci. Technol.*, *42*(15), 5675–5681, doi:10.1021/es703078z.

Ryan, J. C., A. L. Hubbard, J. E. Box, J. Todd, P. Christoffersen, J. R. Carr, T. O. Holt, and N. Snooke (2015), UAV photogrammetry and structure from motion to assess calving dynamics at Store Glacier, a large outlet draining the Greenland ice sheet, *Cryosph.*, *9*(1), 1–11, doi:10.5194/tc-9-1-2015.

Schaepman-Strub, G., M. E. Schaepman, T. H. Painter, S. Dangel, and J. V. Martonchik (2006), Reflectance quantities in optical remote sensing—definitions and case studies, *Remote Sens. Environ.*, *103*(1), 27–42, doi:10.1016/j.rse.2006.03.002.

Sodemann, H., A. S. Palmer, C. Schwierz, M. Schwikowski, and H. Wernli (2006), The transport history of two Saharan dust events archived in an Alpine ice core, *Atmos. Chem. Phys.*, *6*(3), 667–688, doi:10.5194/acp-6-667-2006.

Steltzer, H., C. Landry, T. H. Painter, J. Anderson, and E. Ayres (2009), Biological consequences of earlier snowmelt from desert dust deposition in alpine landscapes., *Proc. Natl. Acad. Sci. U. S. A.*, *106*(28), 11629–34, doi:10.1073/pnas.0900758106.

Sterle, K. M., J. R. McConnell, J. Dozier, R. Edwards, and M. G. Flanner (2013), Retention and radiative forcing of black carbon in eastern Sierra Nevada snow, *Cryosph.*, *7*(1), 365–374, doi:10.5194/tc-7-365-2013.

Thevenon, F., F. S. Anselmetti, S. M. Bernasconi, and M. Schwikowski (2009), Mineral dust and elemental black carbon records from an Alpine ice core (Colle Gnifetti glacier) over the last millennium, *J. Geophys. Res. D Atmos.*, *114*, doi:10.1029/2008JD011490.

Tschiersch, J., B. Hietel, P. Schramel, and F. Trautner (1990), Saharan dust at jungfraujoch, *J. Aerosol Sci.*, *21*, S357–S360, doi:10.1016/0021-8502(90)90256-W.

Warren, S. G. (1982), Optical properties of snow, *Rev. Geophys.*, *20*(1), 67, doi:10.1029/RG020i001p00067.

Warren, S. G. (2013), Can black carbon in snow be detected by remote sensing?, *J. Geophys. Res. Atmos.*, *118*(2), 779–786, doi:10.1029/2012JD018476.

Warren, S. G., and W. J. Wiscombe (1980), A Model for the Spectral Albedo of Snow. II: Snow Containing Atmospheric Aerosols, *J. Atmos. Sci.*, *37*, 2734–2745, doi:10.1175/1520-0469(1980)037<2734:AMFTSA>2.0.CO;2.

Westoby, M. J., J. Brasington, N. F. Glasser, M. J. Hambrey, and J. M. Reynolds (2012), "Structure-from-Motion" photogrammetry: A low-cost, effective tool for geoscience applications, *Geomorphology*, *179*, 300–314, doi:10.1016/j.geomorph.2012.08.021.

Whitehead, K., B. J. Moorman, and C. H. Hugenholtz (2013), Brief Communication: Low-cost, on-demand aerial photogrammetry for glaciological measurement, *Cryosph.*, *7*(6), 1879–1884, doi:10.5194/tc-7-1879-2013.

Wientjes, I. G. M., R. S. W. Van de Wal, G. J. Reichart, a. Sluijs, and J. Oerlemans (2011), Dust from the dark region in the western ablation zone of the Greenland ice sheet, *Cryosph.*, *5*(3), 589–601, doi:10.5194/tc-5-589-2011.

Winton, V. H. L., G. B. Dunbar, N. A. N. Bertler, M.-A. Millet, B. Delmonte, C. B. Atkins, J. M. Chewings, and P. Andersson (2014), The contribution of aeolian sand and dust to iron fertilization of phytoplankton blooms in southwestern Ross Sea, Antarctica, *Global Biogeochem. Cycles*, *28*(4), 423–436, doi:10.1002/2013GB004574.

Wiscombe, W. J. (1980), Improved Mie scattering algorithms., *Appl. Opt.*, *19*(9), 1505–9, doi:10.1364/AO.19.001505.

Wiscombe, W. J., and S. G. Warren (1980), A Model for the Spectral Albedo of Snow. I: Pure Snow, *J. Atmos. Sci.*, *37*(12), 2712–2733, doi:10.1175/1520-0469(1980)037<2712:AMFTSA>2.0.CO;2.

Yasunari, T. J., R. D. Koster, K.-M. Lau, T. Aoki, Y. C. Sud, T. Yamazaki, H. Motoyoshi, and Y. Kodama (2011), Influence of dust and black carbon on the snow albedo in the NASA Goddard Earth Observing System version 5 land surface model, *J. Geophys. Res.*, *116*(D2), D02210, doi:10.1029/2010JD014861.

Yasunari, T. J., R. D. Koster, K.-M. Lau, and K.-M. Kim (2015), Impact of snow darkening via dust, black carbon, and organic carbon on boreal spring climate in the Earth system, *J. Geophys. Res. Atmos.*, n/a–n/a, doi:10.1002/2014JD022977.

3 Snow Darkening Index (SDI) application: examples from repeated digital images at Torgnon experimental site (Aosta valley)

Abstract

In this paper, we show an application of the Snow Darkening Index (SDI), developed in Chapter 2 of this thesis. The application regards the calculation of SDI from repeated digital images from a micrometeorological ration at the experimental site of Torgnon (Aosta valley, Italy). Time series of SDI was compared with snow height, albedo and temperature in order to evaluate the impact of mineral dust deposition on snow radiative properties and speculate the effect on snow melting.

3.1 Introduction

In recent years, the application of Red Green Blue (RGB) digital images in Earth and Environmental Sciences has gained a lot of interest. The availability of low cost digital sensors (typically compact or rephlex cameras) has raised the possibility to install automatic station in impervious or remote areas, with the possibility to collect multiple images during summer and winter seasons.

Common applications regard the monitoring of vegetation phenology [*Richardson et al.*, 2007; *Migliavacca et al.*, 2011; *Julitta et al.*, 2014], landslides, glaciers [*Jung et al.*, 2010] and snow [*Corripio*, 2010; *Hinkler et al.*, 2010; *Dumont et al.*, 2011; *Parajka et al.*, 2012]. Regarding the two latter, using digital cameras researcher successfully retrieved snow albedo and snow cover, both in Alpine and polar areas.

Snow albedo is influenced by different variables, such as grain size, solar zenith angle (SZA), snow density and presence of light-absorbing impurities (LAI) such as black carbon, mineral dust and volcanic ash. Each of these variables has a characteristic effect on snow spectral albedo [*Warren*, 1982]. In the European Alps, glacier and snow covered areas can be periodically covered by mineral dust transported from Saharan desert [*Sodemann et al.*, 2006] and black carbon produced by industrial activities, biomass burning and wildfires. Deposition of these two LAI can impact snow melting [*Painter et al.*, 2007; *Steltzer et al.*, 2009; *Di Mauro et al.*, 2015] and influence glaciers surface mass balance [*Painter et al.*, 2013]. In a previous work [*Di Mauro et al.*, 2015], we proposed the Snow Darkening Index (SDI) as a possible indicator of LAI deposition on snow in the Alps. SDI is a spectral index calculated as the normalized difference of Red and Green channels, and it can be easily applied to digital images.

In this paper, we evaluate the performance of SDI in capturing dust deposition in the European Alps, calculating it from digital images acquired from a micrometeorological station in an alpine prairie in Torgnon (Aosta valley, Italy). The objective of the chapter is to evaluate the performances of SDI in detection depositions and re-emerging of dust layers in a seasonal snowpack. Results could be useful in assessing the impact of dust depositions on snow and modeling the impact on seasonal snow melting and water availability in the Po valley.

3.2 Torgnon (AO) experimental site

The study area is located in the northwestern Italian Alps (Aosta Valley, IT) at 2160 m a.s.l. (45°50’40’’N, 7°34’41’’E). The area is a subalpine unmanaged pasture classified as intra-alpine with semi-continental climate. The site is generally covered by snow from the end of October to late May. Further information regarding the site can be found in [*Migliavacca et al.*, 2011; *Rossini et al.*, 2012; *Galvagno et al.*, 2013].

The experimental site belongs to the Phenocam network (http://phenocam.sr.unh.edu/webcam/) and is equipped with a webcam system and an eddy covariance flux tower for continuous measurements of net ecosystem carbon dioxide exchange.

3.3 Data and Methods

Digital images were collected using a Nixon digital camera (model d5000 with a fixed white balance) installed at the experimental site in 2009. Following *Richardson et al.* [2007], the camera was pointed North and set at an angle of about 20° below horizontal. Camera focal length was 3.5 mm and the field of view was approximately 79.8°. The camera was fixed at 2.5 m above ground and the same view scene was captured. The images were collected in Joint Photographic Experts Group (JPEG) format and present a resolution of 0.3 megapixels, with three color channels (namely red, green and blue), at 8 bits of radiometric resolution. The images were collected from 10 am to 5 pm, with an hourly temporal resolution. Exposure mode and white balance were set to automatic. Air temperature and snow height were measured respectively by a HMP45 (Vaisala Inc.) and a sonic snow depth sensor (SR50A, Campbell Scientific, Inc.). Albedo was measured with a Kipp and Zonen (cnr4 net radiometer).

A Region Of Interest (ROI) was firstly identified in an approximately flat area, to analyze snow evolution. Images were acquired during 2013 and 2014 melting season. Red, Green and Blue chromatic coordinates were extracted from the selected ROI and the Snow Darkening Index (SDI) was calculated combining the Red and Green channel as follows:

$$SDI = \frac{DN_{Red} - DN_{Green}}{DN_{Red} + DN_{Green}}$$

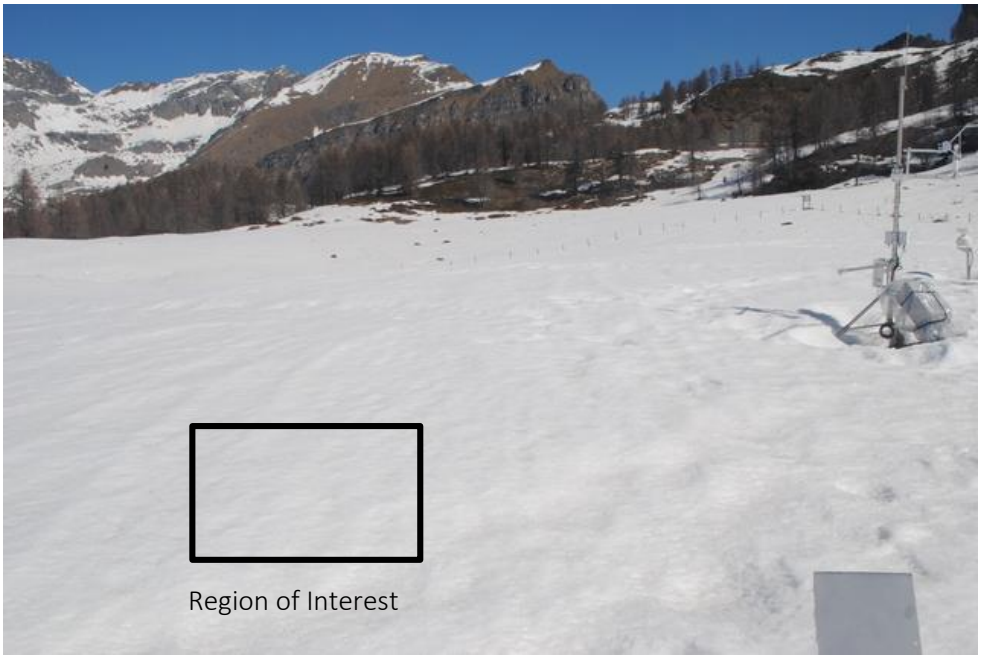

Figure 1 Example of image for the Torgnon experimental site. The image was taken on April 17 2014 at 10 a.m. Black rectangle represents the Region Of Interest (ROI) analyzed.

SDI time series for 2013 and 2014 was analysed, as well as data of snow height, snow temperature and snow albedo, measured by the micrometeorological station in Torgnon.

For evaluating dust depositions timing, we used the Navy Aerosol Analysis and Prediction System (NAAPS) global aerosol model, which is an atmospheric model that simulates the transport and deposition of different particulate matters and gases in the atmosphere. In particular, we used this model to detect the timing of Saharan dust event on the Aosta valley. The NAAPS model is a modified version of that developed by *Christensen* [1997]. The Naval Research Laboratory (NRL) version uses global meteorological fields from the Navy Operational Global Atmospheric Prediction System (NOGAPS) [*Hogan and Rosmond*, 1991] analyses and forecasts on a 1 X 1 degree grid, at 6-hour intervals and 24 vertical levels reaching 100 mbar. The original model used northern hemispheric, 12-hourly European Centre for Medium-Range Weather Forecasts (ECMWF) fields on a 2.5

X 2.5 degree grid. Dust emission occurs whenever the friction velocity exceeds a threshold value, snow depth is less than a critical value, and the surface moisture is less than a critical value. The flux is taken from *Westphal et al.* [1987] and scaled to include only particles with radii smaller than 5 microns. The flux is injected into the lowest two layers of the model. The threshold friction velocity is set to infinity except in known dust-emission areas. These areas originally were defined as areas covered by eight of the 94 land-use types used in the USGS Land Cover Characteristics Database.

We analyzed NAAPS run of Total Optical Depth (TOD) and surface concentration of dust, smoke and sulphate relative to the winters and the springs of 2013 and 2014.

3.4 Results and Discussion

3.4.1 2013 time series

In Figure 2, we show the time series of SDI, snow height, surface temperature and albedo, ranging from DOY 100 to 125 of 2013. From this plot, we can underline the correlation between snow height and snow albedo; this is due to the fact that snow aging causes a growth in grain size and thus a decrease in albedo. During 2013 melting season, surface temperatures became positive around DOY 105, and this caused a rapid snow melt, dampened by small snowfall around DOY 110 and 118. The NAAPS model predicted three major dust events (brown vertical lines in Figure 2) two in April (16th and 30th) and one in May (2nd). In particular, this last event is represented in Figure 3, where Total Optical Depth (TOD) (upper-left panel) and surface concentration of sulfate (upper-right panel), dust (lower-left panel) and smoke (lower-right panel), are mapped at European scale. From these maps is clear that a plume of Saharan dust (high TOD) was transported through the atmosphere and deposited over the Italian peninsula. This dust event caused an increase in SDI and a further decrease in snow albedo. This, coupled with a nearly positive surface temperature, caused a gradual drop of snow height.

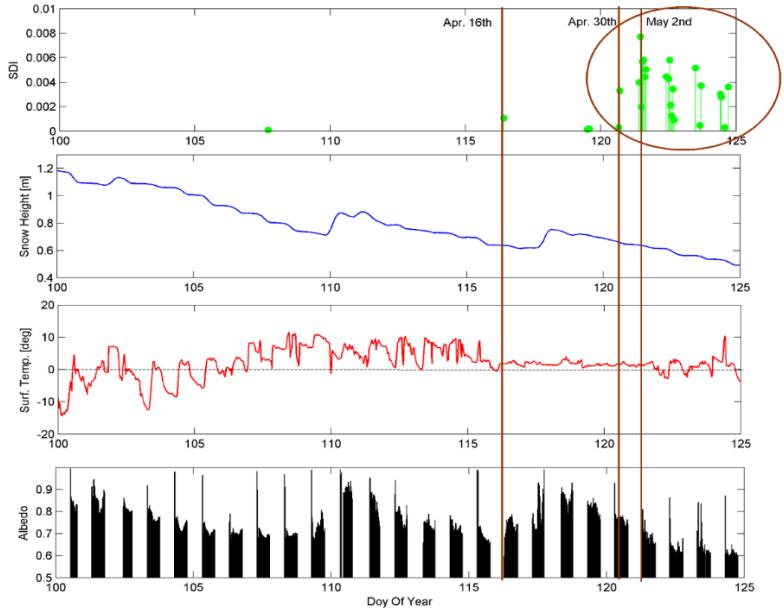

Figure 2 Time series of Snow Darkening Index (SDI), snow height, surface temperature and albedo, observed during 2013 at the Torgnon site

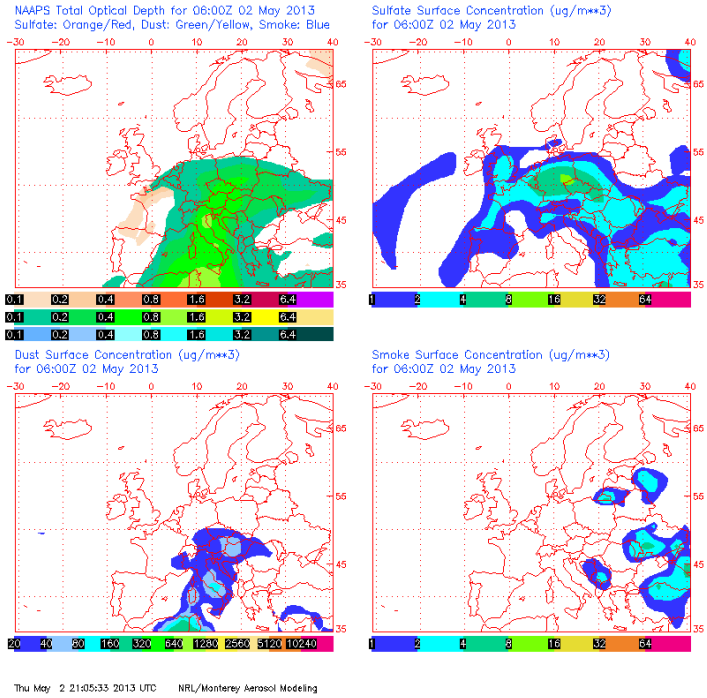

Figure 3 NAAPS model output for the Saharan dust event of May 2nd of 2013.

3.4.2 2014 time series

In Figure 4, we show the time series of SDI, snow height, surface temperature and albedo, ranging from DOY 1 to 125 of 2014. Also in this case, we can see that snow height and snow albedo are well correlated. During 2014 season, NAAPS model predicted 4 major dust events. The first three occurred during February and March, but dust layers were probably buried by new snow, although SDI series showed some variation during the depositions, in particular for the event of February 19th (Figure 5b), the one described in Di Mauro et al. [2015].

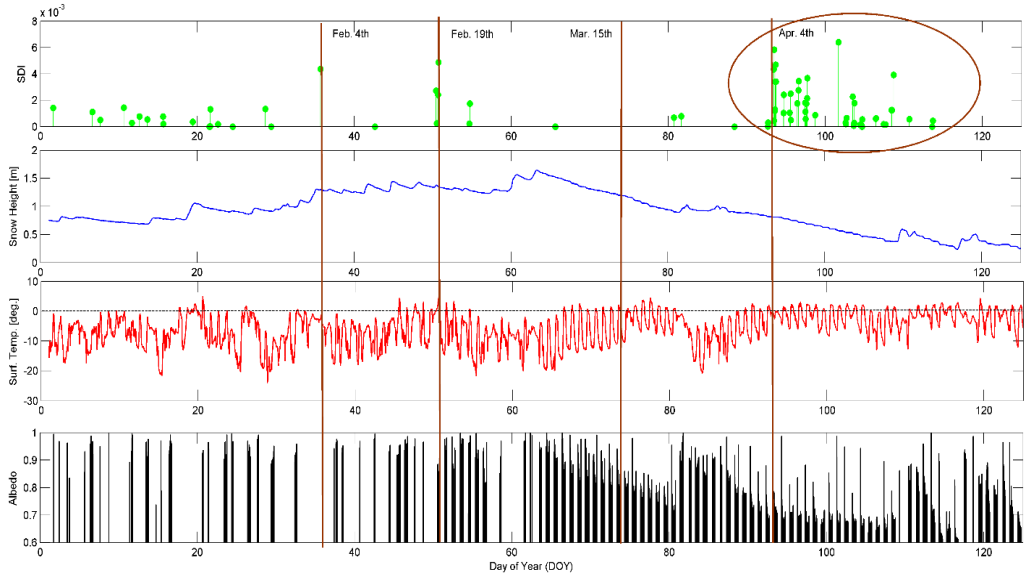

Figure 4 Time series of Snow Darkening Index (SDI), snow height, surface temperature and albedo, observed during 2014 at the Torgnon site

Another dust event occurred in April (Figure 5a) and caused a significant variation in SDI, and thus in albedo values. This variability in SDI could be also related to the re-emergence of dust layers deposited during previous dust events of 2014. This is an important point, because in years characterized by abundant snowfall (such as 2014) the effect of dust depositions on snow albedo can be dampened by the presence of new snow above the dust layers. During the melting season, these layers can aggregate into

the snowpack and re-emerge as the snow melts, acting as a forcing agent in accelerating the melting.

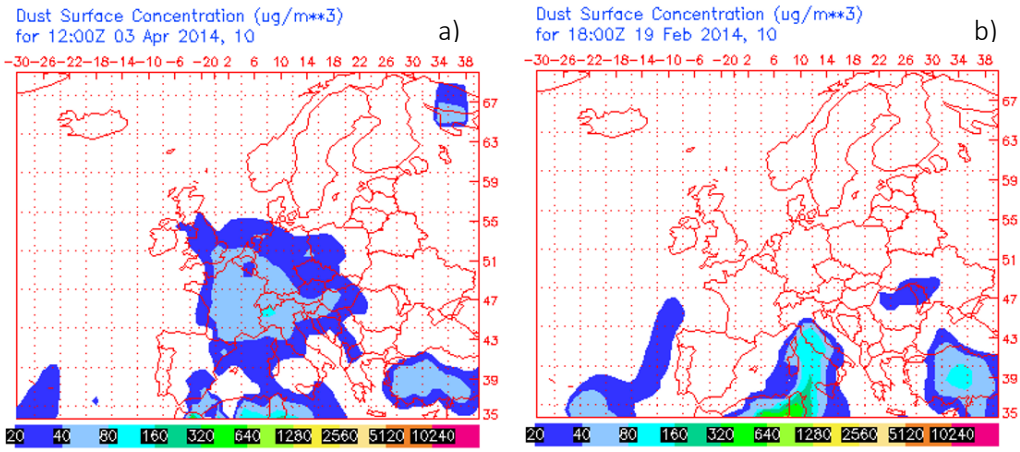

Figure 5 NAAPS model output for dust event on 3 April (left panel) and 19 February (right panel) of 2014

3.5 Conclusions

In this chapter, we showed the possibility to calculate SDI from RGB repeated images taken from a micrometeorological station at the experimental site of Torgnon, in a high altitude Alpine prairie. The integration of these data with an atmospheric transport model (NAAPS), allowed us to evaluate the correspondence of SDI peaking and mineral dust transport from Saharan desert. The good agreement between dust deposition and SDI will allow using this experimental site as a possible validation for satellite imagery (e.g. MODIS; Landsat) and for regional climate models. The presence of dust on snow, in fact, can alter the hydrological cycle in mountain catchments causing fluctuation in water availability in valley regions. Possible developments of these analyses regard the comparison with hydrological models that simulate snow melting, such as the GEOtop model [*Endrizzi et al.*, 2014]. In particular, the evaluation of this model could provide important information regarding water availability in small and medium catchments, and comparisons between observed and simulated snow height could provide information regarding the possible inclusion of light-absorbing impurities effect in hydrological modeling.

Acknowledgments:

I acknowledge ARPA Val D'Aosta (in particular G. Filippa and E. Cremonese) for providing the data of the micrometeorological station. Regions Of Interest (ROI) were extracted using the Phenopix R package (https://r-forge.r-project.org/projects/phenopix/).

Bibliography

Christensen, J. H. (1997), The Danish eulerian hemispheric model — a three-dimensional air pollution model used for the arctic, *Atmos. Environ.*, *31*(24), 4169–4191, doi:10.1016/S1352-2310(97)00264-1.

Corripio, J. (2010), Snow surface albedo estimation using terrestrial photography, *Int. J. Remote Sens.*, 37–41, doi:10.1080/01431160410001709002.

Di Mauro, B., F. Fava, L. Ferrero, R. Garzonio, G. Baccolo, B. Delmonte, and R. Colombo (2015), Mineral dust impact on snow radiative properties in the European Alps combining ground, UAV, and satellite observations, *J. Geophys. Res. Atmos.*, *120*(12), 6080–6097, doi:10.1002/2015JD023287.

Dumont, M., P. Sirguey, Y. Arnaud, and D. Six (2011), Monitoring spatial and temporal variations of surface albedo on Saint Sorlin Glacier (French Alps) using terrestrial photography, *Cryosphere*, *5*, 759–771, doi:10.5194/tc-5-759-2011.

Endrizzi, S., S. Gruber, M. D. Amico, and R. Rigon (2014), GEOtop 2 . 0 : simulating the combined energy and water balance at and below the land surface accounting for soil freezing , snow cover and terrain effects, *Geosci. Model Dev.*, (ii), 2831–2857, doi:10.5194/gmd-7-2831-2014.

Galvagno, M. et al. (2013), Phenology and carbon dioxide source/sink strength of a subalpine grassland in response to an exceptionally short snow season, *Environ. Res. Lett.*, *8*(2), 025008, doi:10.1088/1748-9326/8/2/025008.

Hinkler, J., S. B. Pedersen, M. Rasch, and B. U. Hansen (2010), Automatic snow cover monitoring at high temporal and spatial resolution , using images taken by a standard digital camera, *Int. J. Remote Sens.*, 37–41, doi:10.1080/01431160110113881.

Hogan, T. F., and T. E. Rosmond (1991), The Description of the Navy Operational Global Atmospheric Prediction System's Spectral Forecast Model, *Mon. Weather Rev.*, *119*(8), 1786–1815, doi:10.1175/1520-0493(1991)119<1786:TDOTNO>2.0.CO;2.

Julitta, T. et al. (2014), Agricultural and Forest Meteorology Using digital camera images to analyse snowmelt and phenology of a subalpine grassland, *Agric. For. Meteorol.*, *198-199*, 116–125, doi:10.1016/j.agrformet.2014.08.007.

Jung, J., J. E. Box, J. D. Balog, Y. Ahn, D. T. Decker, and P. Hawbecker (2010), Greenland glacier calving rates from Extreme Ice Survey (EIS) time lapse photogrammetry, *Am. Geophys. Union*.

Migliavacca, M. et al. (2011), Using digital repeat photography and eddy covariance data to model grassland phenology and photosynthetic CO2 uptake, *Agric. For. Meteorol.*, *151*(10), 1325–1337, doi:10.1016/j.agrformet.2011.05.012.

Painter, T. H., A. P. Barrett, C. C. Landry, J. C. Neff, M. P. Cassidy, C. R. Lawrence, K. E. McBride, and G. L. Farmer (2007), Impact of disturbed desert soils on duration of mountain snow cover, *Geophys. Res. Lett.*, *34*(12), L12502, doi:10.1029/2007GL030284.

Painter, T. H., M. G. Flanner, G. Kaser, B. Marzeion, R. A. VanCuren, and W. Abdalati (2013), End of the Little Ice Age in the Alps forced by industrial black carbon., *Proc. Natl. Acad. Sci. U. S. A.*, *110*(38), 15216–21, doi:10.1073/pnas.1302570110.

Parajka, J., P. Haas, R. Kirnbauer, J. Jansa, and G. Blöschl (2012), Potential of time-lapse photography of snow for hydrological purposes at the small catchment scale, *Hydrol. Process.*, *26*(22), 3327–3337, doi:10.1002/hyp.8389.

Richardson, A. D., J. P. Jenkins, B. H. Braswell, D. Y. Hollinger, S. V Ollinger, and M.-L. Smith (2007), Use of digital webcam images to track spring green-up in a deciduous broadleaf forest., *Oecologia*, *152*(2), 323–34, doi:10.1007/s00442-006-0657-z.

Rossini, M. et al. (2012), Remote sensing-based estimation of gross primary production in a subalpine grassland, *Biogeosciences*, *9*(7), 2565–2584, doi:10.5194/bg-9-2565-2012.

Sodemann, H., A. S. Palmer, C. Schwierz, M. Schwikowski, and H. Wernli (2006), The transport history of two Saharan dust events archived in an Alpine ice core, *Atmos. Chem. Phys.*, *6*(3), 667–688, doi:10.5194/acp-6-667-2006.

Steltzer, H., C. Landry, T. H. Painter, J. Anderson, and E. Ayres (2009), Biological consequences of earlier snowmelt from desert dust deposition in alpine landscapes., *Proc. Natl. Acad. Sci. U. S. A.*, *106*(28), 11629–34, doi:10.1073/pnas.0900758106.

Warren, S. G. (1982), Optical properties of snow, *Rev. Geophys.*, *20*, 67, doi:10.1029/RG020i001p00067.

Westphal, D. L., O. B. Toon, and T. N. Carlson (1987), A two-dimensional numerical investigation of the dynamics and microphysics of Saharan dust storms, *J. Geophys. Res.*, *92*(D3), 3027, doi:10.1029/JD092iD03p03027.

4 What darkens mountain glaciers? A radiative and geochemical assessment for the Morteratsch glacier (Swiss Alps)

Abstract

Mountain glaciers represent an important source of fresh water across the globe. Those reservoirs are seriously threatened by global climate change, and a widespread reduction of glacier extension has been observed in recent years. Surface processes that promote ice melting are driven both by temperature/precipitation and albedo. The latter is influenced by the growth of snow grains and by the impurities content (such as dust, soot, ash, algae etc.). The origin of these light-absorbing impurities can be local or distal, often they can aggregate on the glacier tongue forming characteristic cryoconites, that decrease ice albedo promoting the melting.

In this paper, we present results of a hyper-spectral (EO1 - Hyperion) and a multi-spectral (Landsat 8 - OLI) satellite data in characterizing ice and snow surface albedo at the Morteratsch glacier (Swiss Alps). We coupled those satellite data with ground hyperspectral data collected with an ASD field spectrometer on the glacier ablation zone. For each plot, we also sampled ice and processed it with a Neutron Activation Analysis (NAA) in order to determine its geochemical composition. In a previous study, we developed the Snow Darkening Index (SDI), which is non-linearly correlated with dust content in snow. Here we calculated it from Hyperion and OLI data, and characterized snow/ice darkening at the Morteratsch glacier. Results showed that, during summer season, reflectance of ice at Morteratsch can reach very low values (0.1-0.2) and this is due to the interplay of surface dust (from lateral moraine and Saharan desert) and cryoconites, formed by accumulation of dust and dark organic material.

4.1 Introduction

Mountain glaciers represent an important source of fresh water across the globe. Those reservoirs are seriously threatened by global climate change [*Immerzeel et al.*, 2010], and a widespread reduction of glacier extension has been observed in recent years [*Paul et al.*, 2007]. Surface processes that promote ice melting are driven both by temperature/precipitation and by albedo. The latter is mainly influenced by the growth of snow grain size and by the impurities content (such as dust, soot, ash, algae etc.) [*Painter et al.*, 2007]. The impact of these light-absorbing impurities on the cryosphere has been studied at a global [*Flanner et al.*, 2007, 2009] and regional scale [*Painter et al.*, 2010, 2013; *Sterle et al.*, 2013; *Di Mauro et al.*, 2015].

Recent papers showed that Himalayan glaciers are undergoing a darkening process [*Ming et al.*, 2012, 2015; *Gautam et al.*, 2013], this was ascribed to the impact of regional/global warming and to the deposition of light-absorbing impurities on the glacial surface. Impurities such as black carbon and mineral dust are widely present in Himalayan area [*Nair et al.*, 2013; *Ménégoz et al.*, 2014], and their source can be both natural and anthropogenic. Instead, natural sources of mineral dust are represented by arid and hyper-arid areas surrounding the glaciers. Coupling data from an Automated Weather Station (AWS) with distributed modeling, Oerlemans et al. (2009) showed that albedo decrease in mountain glaciers can effectively increase the melt producing negative surface mass balance.

Light-absorbing impurities can be deposited also on ice sheets. In particular, has been observed that Greenland albedo is decreasing in the last decade [*Box et al.*, 2012], and still a lot of uncertainties exist regarding potential causes and impact [*Polashenski et al.*, 2015; *Tedesco et al.*, 2015].

When light-absorbing impurities are deposited on snow and ice, they can aggregate on the glacier tongue forming characteristic cryoconites that decrease ice albedo promoting the melting [*Takeuchi et al.*, 2001]. Cryoconites are small ecosystems with a proper biogeochemical cycling (i.e. carbon and nitrogen) [*Segawa et al.*, 2014], they are

constituted mainly of dust and organic matter that forms typical cryoconite holes in ablation areas of mountain and polar glaciers. Cryoconites were firstly named as "Kryokonites" (from Greek ethimology *kryo*: ice, and *konis:* dust) by Swedish explorer A. E. Nordenskiöld, during his expedition in Greenland interior in 1883 [*Nordenskiöld*, 1883]. Nordenskiöld concluded that these material cannot have been washed down from the mountain ridges at the sides of the glaciers, that neither had it been distributed over the surface of the ice by running water, nor been pressed up from the ground moraine, but that the clay must therefore be a sediment from the air, the chief constituent of which is probably terrestrial dust spread by the wind over the surface of the ice. His statements could be true for Greenland glaciers during the first phase of the industrial revolution, but cannot be extended to mountain glaciers, where multiple processed act in formation and evolution of cryoconites [*Hodson et al.*, 2007; *Bøggild et al.*, 2010].

The geochemical and microbiological composition of cryoconites has been studied in polar and non-polar glaciers [*Aoki et al.*, 2014; *Nagatsuka et al.*, 2014; *Takeuchi et al.*, 2014] but still a lot of uncertainties exist regarding their formation and evolution. Microbiological organisms that colonize extreme environments (e.g. salty lakes, sulfur springs, glaciers and ice caps) are known as 'extremophiles'. They are highly adapted organisms that can live in harsh environments. Microorganisms found in cryoconites are element of this class (often referred as psychrophiles); they can remain quiescent during the winter, when cryoconite holes are buried by new snow, and then become active again during melting season when exposed to solar radiation. In this sense, cryoconites represent an active field of research from multiple disciplines [*Takeuchi et al.*, 2001; *Hodson et al.*, 2007; *Bøggild et al.*, 2010; *Irvine-Fynn et al.*, 2011; *Stibal et al.*, 2012; *Zarsky et al.*, 2013].

To date, a complete assessment of what kind of materials darken mountain glaciers and their impact on glacier albedo is still missing. In this paper, we combine a classic multi-scale remote sensing approach with a geochemical characterization of samples collected

in a large mountain glacier of the European Alps (Vadret da Morteratsch) in order to determine the impact of surface dust and cryoconites on the surface reflectance of Morteratsch glacier.

4.2 Data and Methods

4.2.1 Study area and field campaigns

Vadret da Morteratsch (46°24′34″N, 9°55′54″E) is a glacier located in the Bernina-Disgrazia massif in Swiss Alps. Morteratsch is a valley glacier with an altitude that spans from 2030 to 3976, with an area of 15.81 km^2; it is a typical north facing Alpine glacier experiencing negative mass balances in the last century [*WGMS*, 2013].

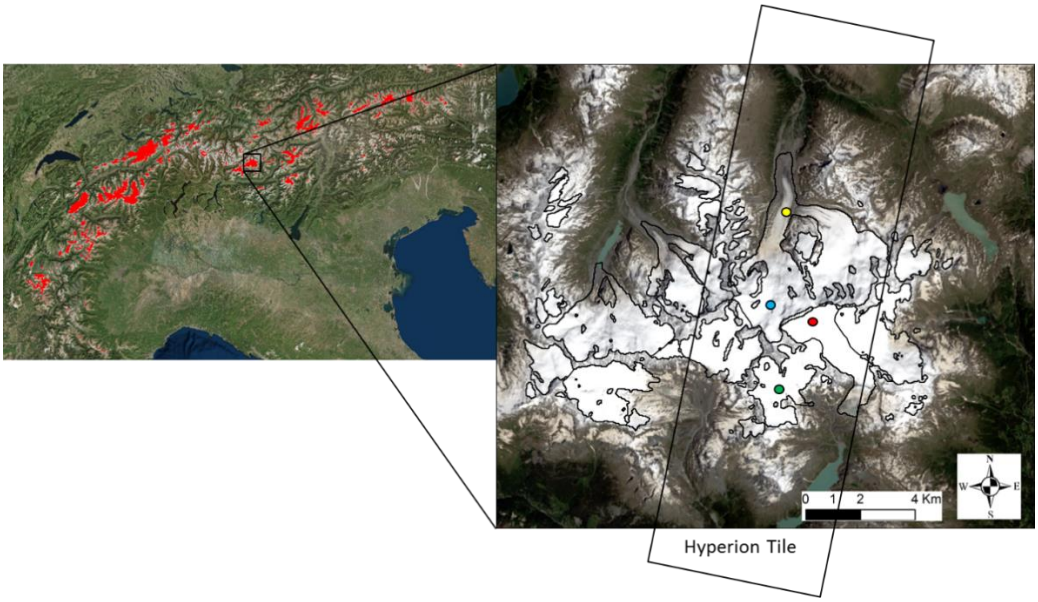

Figure 1 Left panel: Location of the study area, red polygons are glacier extracted from the Randolph Glaciers Inventory v.3.2 [*Pfeffer et al.*, 2014]**. Right panel: True color representation of Hyperion scene. (Markers are color-coded as follows, red: accumulation zone; cyan: serac; yellow: ablation zone; green: bare ice.**

On the 30th July and 31st of September 2015, two field campaign were conducted at the Morteratsch glacier in Swiss Alps. The aim of the field measurements was to collect ground hyperspectral reflectance data and ice/snow samples at the glacier ablation zone. Reflectance was measured in clear sky condition with an Analytical Spectral

Devices (ASD) field spectrometer (Hand Held), which collects reflected radiance from 325 to 1075 nm with a spectral resolution of 1 nanometer. Reflectance was then calculated by normalizing for the incident radiance measured with a calibrated Spectralon© panel. Snow and ice sampling was conducted using Corning tubes (50 mL). Locations of sampling were visually evaluated in order to have the highest variability in snow and ice optical properties. Regarding cryoconites sampling, we broke the upper part of each cryoconite holes and we picked the sediment at the bottom of the hole using a little spoon. All samples were taken back to the University Campus (Milano-Bicocca) and stored at -30 degreees at the EuroCold facility of our department.

A few days before the September campaign, new snowfall occurred on the glacier; so, only spectra of snow were collected, and cryoconite holes were found buried by snow and sampled for the geochemical analysis. We can divide samples in 4 main classes: fresh snow, bright ice, dark ice, and cryoconite holes.

Figure 2 Left: Reflectance measurements during the second campaign (30th September) at Morteratsch glacier. Right: An example of cryoconite hole found on the ablation area of Morteratsch glacier (Photos by R. Garzonio.)

4.2.2 Geochemical analysis

We determined geochemical elemental composition of samples through a Neutron Activation Analysis (NAA). This methodology allows to determine the relative abundance of almost all the element in the periodic table. Irradiations of samples were carried out

at LENA (Applied Nuclear Energy Laboratory, University of Pavia) where a research nuclear reactor (TRIGA Mark II) is installed. Measurements of the irradiated samples were carried out at the Radioactivity Laboratory of the Milano-Bicocca University. A complete description of the methodology can be found in *Baccolo et al.* 2015a, 2015b.

4.2.3 Satellite data

The Earth Observing One (EO-1) satellite mission was launched in November 2000, and features a hyper-spectral (Hyperion) and a multi-spectral sensor (Advanced Land Imager, ALI) [*Middleton et al.*, 2013]. In particular, the Hyperion sensor features a swath of 7.7 km and a spatial resolution of 30 meters. It collects spectral radiance from 400 to 2400 nanometers with a spectral resolution of 10 nm (242 bands). The signal-to-noise ratio (SNR) of Hyperion data varies from 150:1 (for 400-1000 nm) to 60:1 (for 1000-2000 nm), that is comparable to the Airborne Visible/Infrared Imaging Spectrometer (AVIRIS). Even if widely applied for environmental studies (e.g. for inland waters *Giardino et al.*, 2007), still few papers apply Hyperion data for snow and ice satellite monitoring [*Bindschadler and Choi*, 2003; *Casey and Kääb*, 2012; *Casey et al.*, 2012; *Negi et al.*, 2013]. In facts, Hyperion data can provide very important information regarding the optical properties of snow and ice, in particular regarding the impact of light-absorbing impurities and grain size growth.

During August 2015, the Earth Observing One (EO-1) satellite was planned to acquire a series of scenes over the Morteratsch glacier. Among all the available tiles, we selected the one acquired on 7th August (ID: EO1H1930282015219110K5_SG1_01) because of the low cloud cover and the proximity of field campaign (31st July). The selected tile was atmospherically corrected using the 6S code [*Vermote et al.*, 1997]. The Aerosol Optical Depth (AOD) was interpolated from nearby Aerosol Robotic Network (AERONET) stations, and a continental aerosol model was used to approximate atmospheric particle size distributions during summer at Midlatitude. Since the Hyperion sensor is constituted of two spectrometer with different characteristics, the 6S code was run separately for

the Visible Near-Infrared and the ShortWave-Infrared spectrometer. Then the two corrected images were merged and highly noisy bands in the overlapping spectral region were deleted.

Furthermore, a Landsat 8 Operational Land Imager (OLI) was downloaded from the Earth Explorer portal (http://earthexplorer.usgs.gov/). The tile (ID: LC81940282015219LGN00) was acquired on 7th August, a few hours after the Hyperion one. The Landsat Surface Reflectance Climate Data Record (CDR) was downloaded, these products are delivered already corrected for the influence of the atmosphere.

Both from Landsat and Hyperion data, we calculated the Snow Darkening Index (SDI) [*Di Mauro et al.*, 2015], which is a spectral index calculated as a normalized ratio between Red and Green bands, in formula:

$$SDI = \frac{\rho(640;670\text{nm}) - \rho(550;590\text{nm})}{\rho(640;670\text{nm}) + \rho(550;590\text{nm})}$$

SDI is nonlinearly correlated with mineral dust (MD) concentration in snow and represents an important tool for detecting MD deposition and impact on snow albedo. Regarding Hyperion, we used Band at 650 nm and 579 nm; instead, for Landsat 8 we used Band 4 (636-673 nm) and Band 3 (533-590 nm).

4.3 Results

Results from the field spectroscopy survey showed a large variability in spectral albedo on the ablation tongue of Morteratsch glacier. The scale of variation spans from the centimeter to meters, with marked differences in the optical properties of ice. We classified glacier ablation surface in four classes: White Ice (WI), Black Ice (BI), Melt Pond (MP) and Cryoconites. In Figure 3, we show some examples of glacier spectral reflectance. WI samples showed higher reflectance values in the visible wavelengths

with respect to the BI ones (Fig. 3a). WI and BI samples showed low variability in visible wavelengths, whereas MP and Cryoconites showed a peak at 560 nm.

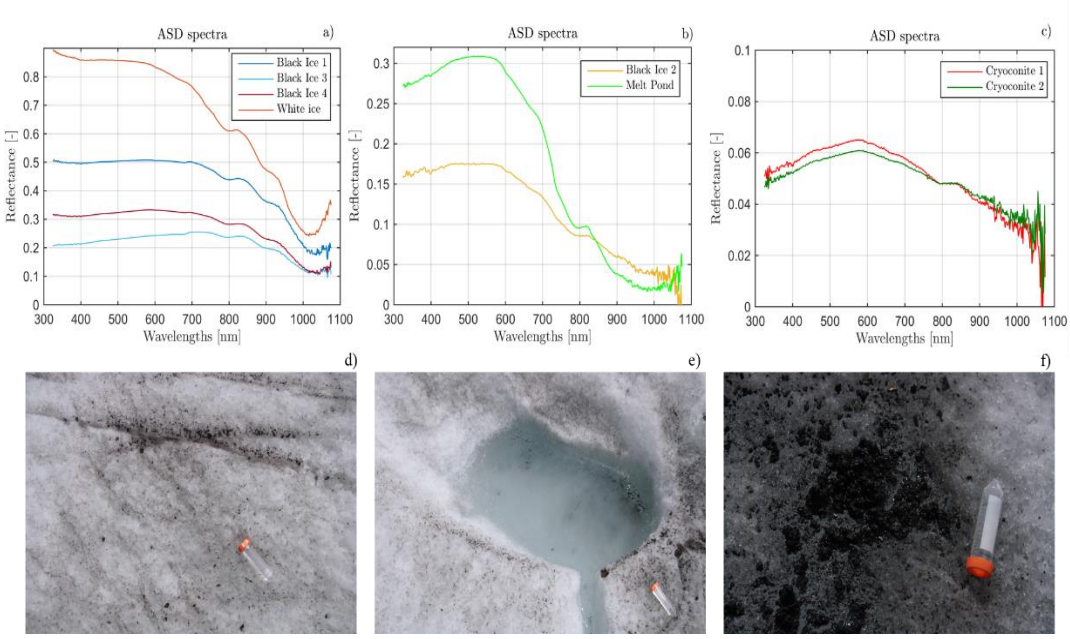

Figure 3 Top panels: Reflectance spectra acquired on the glacier ablation zone with the Field Spec ASD. Note that the scale changing among different plots for representation purposes. Bottom panels: pictures of samples Black ice 4, Melt pond and Cryoconite 1. Corning tubes (12 cm long) is here used for scale reference.

Hyperion hyper-spectral data were analysed to study the variability in spectral albedo across the whole glacier surface. Direct comparison with ground spectra is not presented since the ground survey explored only the ablation area, where most variability in optical properties is below the Hyperion spatial resolution (30 m). In Figure 4, we show some examples of spectra extracted from Hyperion data in different areas of the glacier, that is the accumulation zone, serac, ablation zone and bare ice. Atmospherically corrected reflectance was smoothed using a Savitzky-Golay filter in order to remove the noise from Hyperion spectra. The bands in the overlapping zone of the two spectrometers were removed for representation purposes.

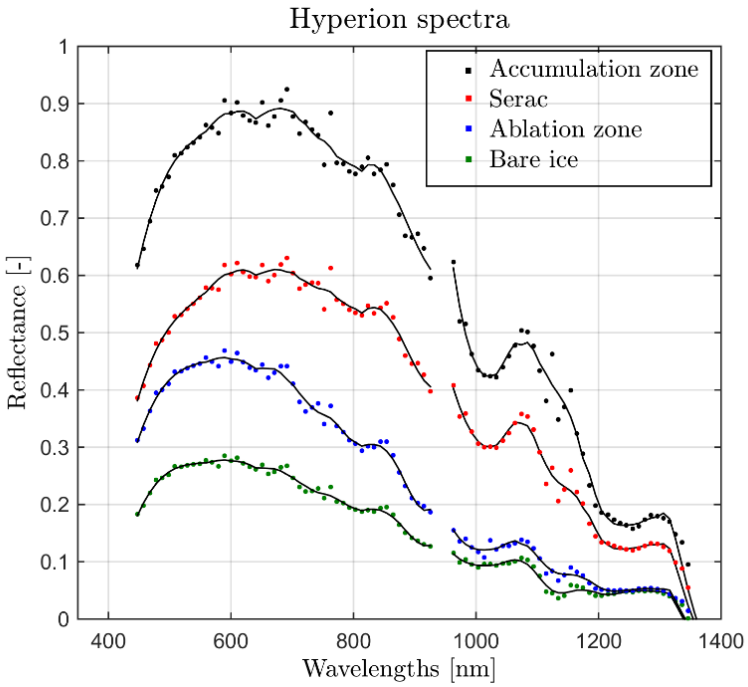

Figure 4 Reflectance spectra of the Morteratsch glacier extracted from Hyperion data. Symbols: crosses: Accumulation zone; dots: Serac; asterisks: ablation zone; circles: bare ice. Red lines are smoothed reflectance with a Savitsky-Golay filter.

The comparison between Hyperion and Landsat data showed good agreement between the two sensors. In Figure 5, we show a simple comparison between the atmospherically corrected reflectance of Hyperion and Landsat 8.

In figure 6, we show a true color representation and SDI map created from Hyperion and Landsat data. In general, the two sensors produced similar pattern over the glacier terrain. Higher SDI values were found over the serac zone, between the accumulation and ablation areas, where a Saharan dust layer was outcropping from 2014 heavy depositions [*Varga et al.*, 2014; *Di Mauro et al.*, 2015]. Also the accumulation zone showed non-zero values of SDI, this suggests the idea that some impurities were deposited also in the upper zone of the glacier.

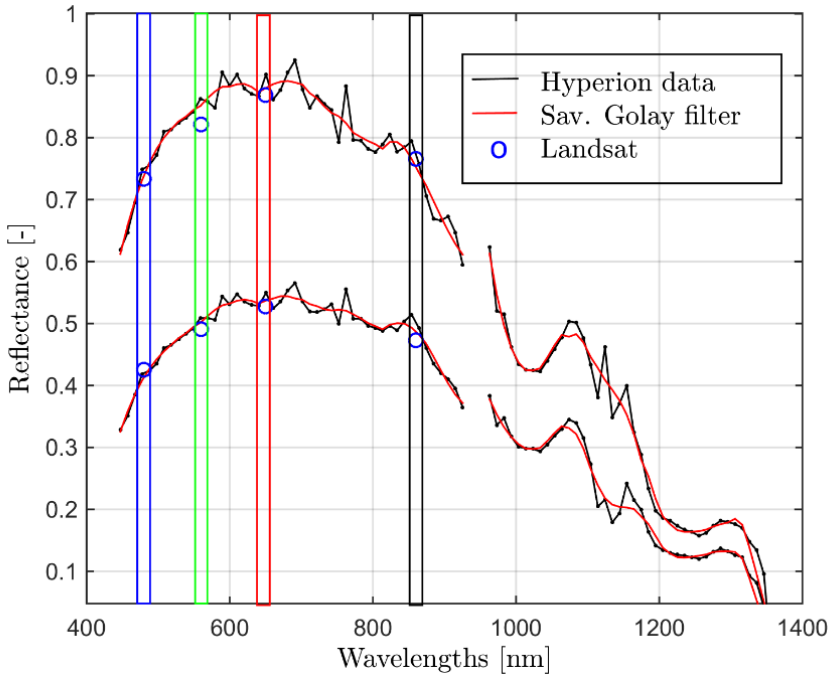

Figure 5 Comparison between Landsat and Hyperion data of the accumulation zone and serac. Vertical lines represent the Landsat acquisition bands in blue (Band 2), green (Band 3), red (Band 4) and near-infrared (Band 5).

Instead, the ablation zone showed a very flat spectral signature (Figure 4), with approximately zero SDI values, this means that other processes are involved in this area, and the SDI is unable to capture them. In fact, during the summer season mineral fine debris and organic matter accumulate on the bare ice (see for example Figure 7, taken in the nearby Fellaria glacier) strongly reducing its albedo and enhancing the melting.

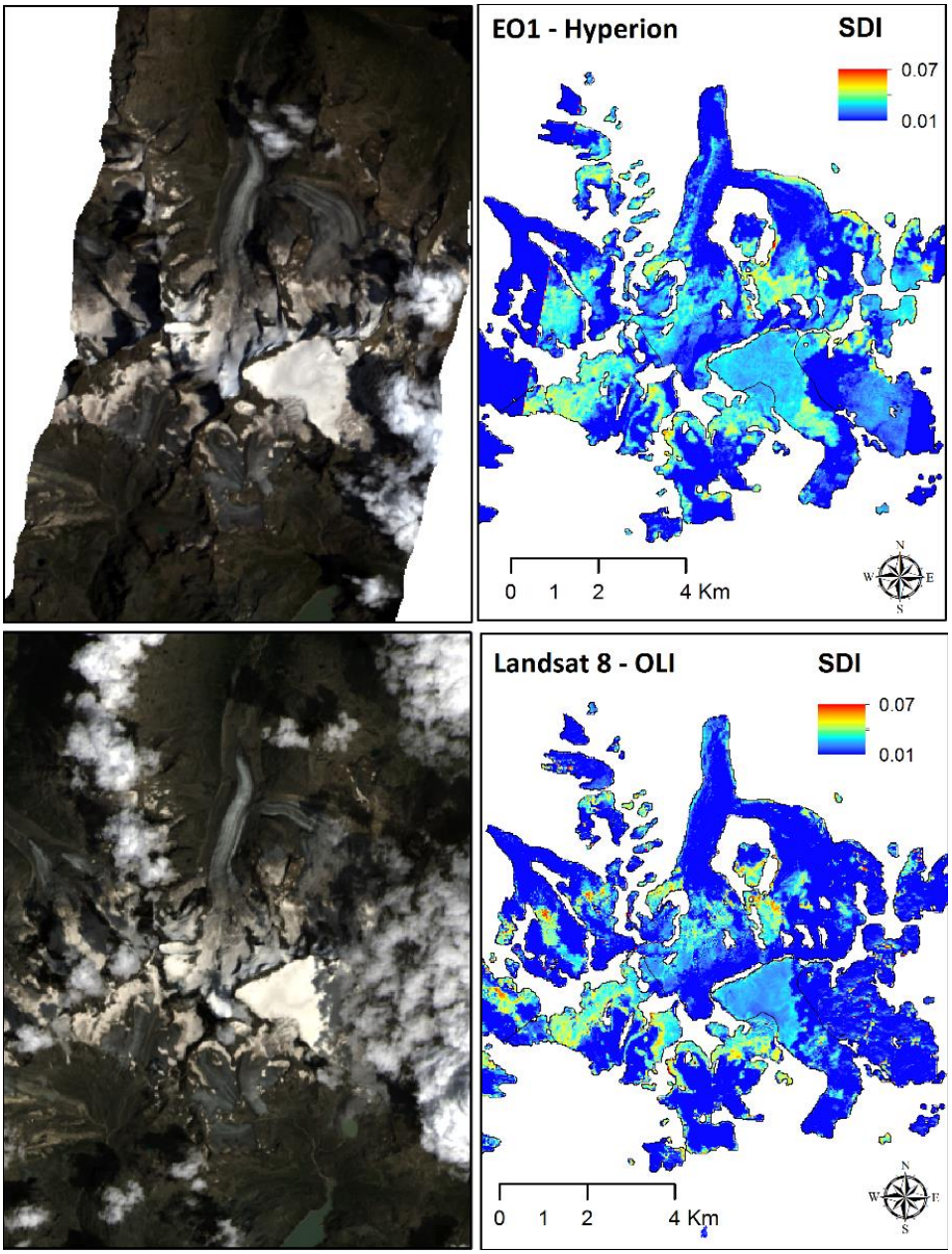

Figure 6 Upper panels: true color representation and SDI of Landsat 8 tile. Lower panels: true color representation and SDI of the Hyperion tile.

Figure 7 Fellaria glacier during summer 2015. Example of glacier surface darkening due to fine debris cover (Photo by F. Fussi)

4.3.1 Elemental composition

Preliminary results from the geochemical characterization showed that elements found in cryoconites hole (CR3 in Figure 8) are present also in sediment from the side moraine (MS1), suggesting an important local source of mineral material. The most abundant elements found are Aluminum (Al) and Silicon (Si), followed by Calcium (Ca), Potassium (K), Magnesium (Mg), Sodium (Na) and Titanium (Ti).

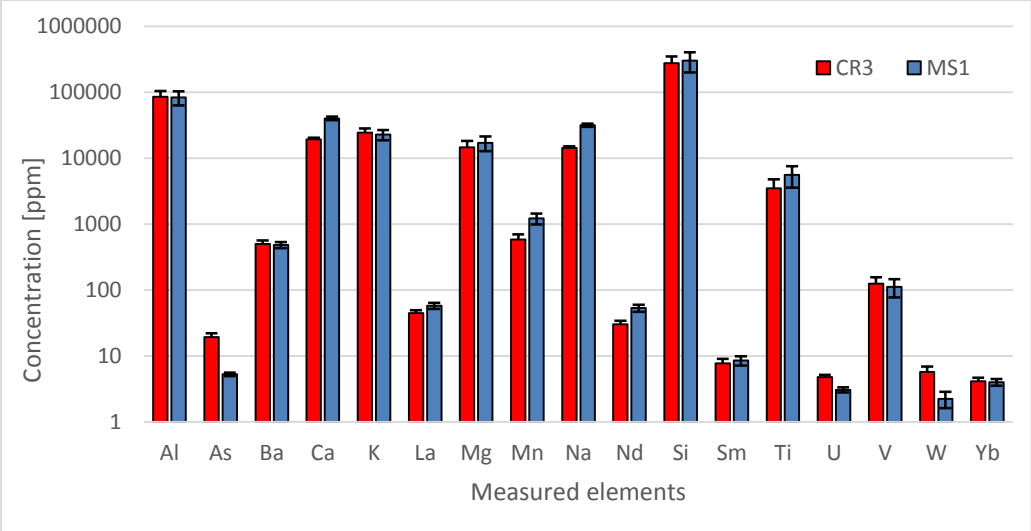

Figure 8 Concentration of the main elements found in cryoconite holes (sample CR3) and in sediments from the side moraine (MS1). Note that the ordinates are showed in a logarithmic scale.

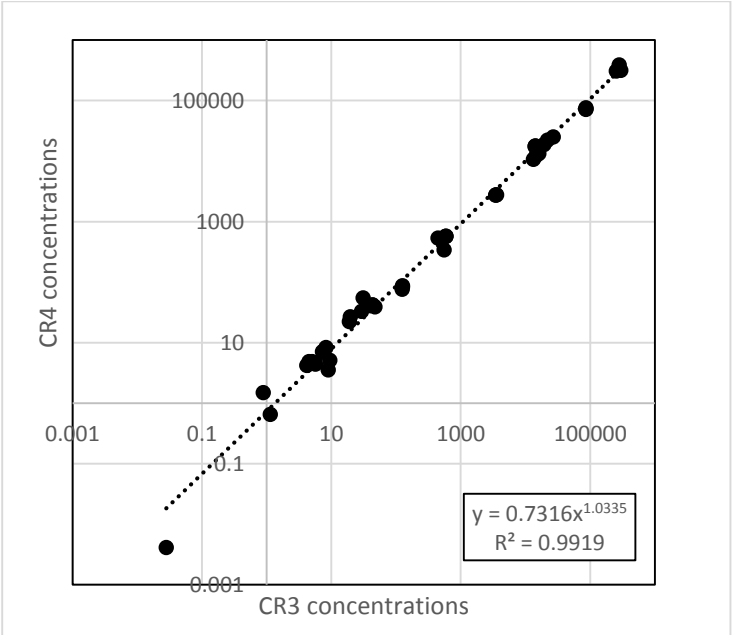

Figure 9 Concentrations of all 45 elements measured in cryoconite holes (sample CR3 and CR4). Note that both axis are represented in logarithmic coordinates

The relative abundance of elements found in cryoconites is here reported in decreasing order: Si > Al > K > Ca > Mg > Na > Ti > Mn > Ba > V > La > Nd > As > Sm > W > U > Yb; instead the abundance in moraine sediments is: Si > Al > Ca > Na > K > Mg > Ti > Mn > Ba > V > La > Nd > Sm > As > Yb > U > W. Differences in the samples can be ascribed, for example, to metabolic activity of microorganisms contained in the cryoconite holes.

We found that elemental concentrations were very similar among different cryoconite holes Figure 9 shows the non-linear (power law function) relation between the concentration of all 45 elements measured in two cryoconite samples (CR3 and CR4).

4.4 Discussion

Results here presented suggest that surface dust and cryoconites can strongly reduce the reflectance of Morteratsch glacier during the summer season, when bare ice is exposed to direct solar radiation. To date, no scientific literature is devoted to study the interplay between dust, cryoconites and glacier albedo decrease in the European Alps. Here we show for the first time the elemental composition of cryoconites and the effect of this non-ice material on spectral reflectance of ice from ground and satellite hyperspectral observations of a glacier in the European Alps.

A previous work on Morteratsch glacier [*Oerlemans et al.*, 2009] showed that the ablation zone is undergoing a darkening process. The authors attributed this albedo decrease to the accumulation of dust from the lateral moraine. In this paper, we showed how spectral reflectance is distributed over the glacier and in particular over the ablation zone. The presence of cryoconite holes and surface dust over the bare ice in alpine glaciers plays an important role in albedo decrease and melting enhancement. Our results show that the reflectance of ice can decrease from 0.8 to 0.1 because of the presence of surface non-ice material, producing very high instantaneous radiative forcing. Furthermore, SDI maps showed the presence of outcropping mineral dust from Saharan depositions occurred during the extremely dusty 2014 spring season [*Varga et*

al., 2014; *Di Mauro et al.*, 2015]. The presence of dust across the equilibrium line altitude (ELA) of an Alpine glacier during the summer season further decrease its albedo and enhances the melt at higher altitude, where new snow and firn are directly exposed to solar radiation.

Cryoconite holes can be part of an active process in crevasses and glacier moulin formation, and in the fragmentation of the ablation zone. We suggest that cryoconites are also involved in a feedback process, here explained: when cryoconite holes are disrupted by surface melting, they release large quantity of dark material and water on the surface of the glacier (see for example Figure 3f). This process further increases the surface melting, since water has a higher thermal inertia with respect to ice. In fact, it can efficiently absorb solar radiation and transfer it to underlying ice, promoting its melting. We named this process as "cryoconite-runoff feedback", and we claim that it can occur on different scale both on mountain glaciers and ice sheets.

The geochemical characterization of cryoconites showed a strong input of local sources, but important enrichments of Arsenic (As), Tungsten (W) and Uranium (U) were also found in cryoconite holes. Our results are consistent with those found by *Wientjes et al.* [2011] and *Singh et al.* [2013], which measured high concentration of metals (in particular Arsenic) in cryoconites in South-West Greenland and Svalbard respectively. Furthermore, the high presence of Tungsten in cryoconites suggests a strong biological activity, since it is the only metal from the third transition series that is known to occur in biomolecules.

In this paper, we focused on the geochemical and radiative properties of cryoconites, although they are formed by living microorganisms (such as cyanobacteria), important features that promote ice melting are due to their geochemical properties.

4.5 Conclusions

In this paper, we showed how non-ice materials influence the spectral reflectance of an Alpine glacier (Vadret da Morteratsch). Results from field campaigns and satellite hyperspectral data showed that surface dust and cryoconites can decrease ice spectral reflectance from 0.8 to 0.1 in visible wavelengths, adding a consistent input of energy to the glacier radiative balance. In particular, the ablation zone was covered by fine debris originating from the side moraine. The relevance of this process is high, since Alpine glacier are in strong retreat and accumulation of light-absorbing impurities can strongly decrease albedo and influence the melt.

Acknowledgements

I acknowledge G. Baccolo, R. Garzonio, C. Giardino and I. Cazzaniga (CNR-IREA) for participating the field campaigns and for the help the atmospheric correction of Hyperion data. I would also like to thank Lawrence Ong (NASA GSFC) for scheduling the EO1 satellite data acquisition. I also thank D. Massabò (INFN-UNIGE) and A. Piazzalunga (UNIMIB) for measuring BC, OC, EC and MAC; although not included in this version, these data will be helpful to attribute possible anthropogenic impact on cryoconites. A final version of this chapter will be submitted to *The Cryosphere* journal.

Bibliography

Aoki, T., S. Matoba, J. Uetake, N. Takeuchi, and H. Motoyama (2014), Field activities of the "Snow Impurity and Glacial Microbe effects on abrupt warming in the Arctic" (SIGMA) Project in Greenland in 2011-2013, *Bull. Glaciol. Res.*, *32*, 3–20, doi:10.5331/bgr.32.3.

Baccolo, G., M. Clemenza, B. Delmonte, N. Maffezzoli, M. Nastasi, E. Previtali, and V. Maggi (2015a), Assessing the geochemical fingerprint of the 2010 Eyjafjallajökull tephra through instrumental neutron activation analysis: a trace element approach, *J. Radioanal. Nucl. Chem.*, *306*(2), 429–435, doi:10.1007/s10967-015-4092-7.

Baccolo, G., N. Maffezzoli, M. Clemenza, B. Delmonte, M. Prata, A. Salvini, V. Maggi, and E. Previtali (2015b), Low-background neutron activation analysis: a powerful tool for atmospheric mineral dust analysis in ice cores, *J. Radioanal. Nucl. Chem.*, *306*(3), 589–597, doi:10.1007/s10967-015-4206-2.

Bindschadler, R., and H. Choi (2003), Characterizing and correcting hyperion detectors using ice-sheet images, *IEEE Trans. Geosci. Remote Sens.*, *41*(6), 1189–1193, doi:10.1109/TGRS.2003.813208.

Bøggild, C. E., R. E. Brandt, K. J. Brown, and S. G. Warren (2010), The ablation zone in northeast Greenland : ice types , albedos and impurities, *J. Glaciol.*, *56*(195), 101–113.

Box, J. E., X. Fettweis, J. C. Stroeve, M. Tedesco, D. K. Hall, and K. Steffen (2012), Greenland ice sheet albedo feedback: thermodynamics and atmospheric drivers, *Cryosph.*, *6*(4), 821–839, doi:10.5194/tc-6-821-2012.

Casey, K., and A. Kääb (2012), Estimation of Supraglacial Dust and Debris Geochemical Composition via Satellite Reflectance and Emissivity, *Remote Sens.*, *4*(12), 2554–2575, doi:10.3390/rs4092554.

Casey, K. a., a. Kääb, and D. I. Benn (2012), Geochemical characterization of supraglacial debris via in situ and optical remote sensing methods: a case study in Khumbu Himalaya, Nepal, *Cryosph.*, *6*(1), 85–100, doi:10.5194/tc-6-85-2012.

Di Mauro, B., F. Fava, L. Ferrero, R. Garzonio, G. Baccolo, B. Delmonte, and R. Colombo (2015), Mineral dust impact on snow radiative properties in the European Alps

combining ground, UAV, and satellite observations, *J. Geophys. Res. Atmos.*, *120*(12), 6080–6097, doi:10.1002/2015JD023287.

Flanner, M. G., C. S. Zender, J. T. Randerson, and P. J. Rasch (2007), Present-day climate forcing and response from black carbon in snow, *J. Geophys. Res.*, *112*(D11), D11202, doi:10.1029/2006JD008003.

Flanner, M. G., C. S. Zender, P. G. Hess, N. M. Mahowald, T. H. Painter, V. Ramanathan, and P. J. Rasch (2009), Springtime warming and reduced snow cover from carbonaceous particles, *Atmos. Chem. Phys.*, *9*(7), 2481–2497, doi:10.5194/acp-9-2481-2009.

Gautam, R., N. C. Hsu, W. K.-M. Lau, and T. J. Yasunari (2013), Satellite observations of desert dust-induced Himalayan snow darkening, *Geophys. Res. Lett.*, *40*(5), 988–993, doi:10.1002/grl.50226.

Giardino, C., V. E. Brando, A. G. Dekker, N. Strömbeck, and G. Candiani (2007), Assessment of water quality in Lake Garda (Italy) using Hyperion, *Remote Sens. Environ.*, *109*(2), 183–195, doi:10.1016/j.rse.2006.12.017.

Hodson, A. et al. (2007), A glacier respires: Quantifying the distribution and respiration CO 2 flux of cryoconite across an entire Arctic supraglacial ecosystem, *J. Geophys. Res.*, *112*(G4), G04S36, doi:10.1029/2007JG000452.

Immerzeel, W. W., L. P. H. van Beek, and M. F. P. Bierkens (2010), Climate change will affect the Asian water towers., *Science*, *328*(5984), 1382–5, doi:10.1126/science.1183188.

Irvine-Fynn, T. D. L., J. W. Bridge, and A. J. Hodson (2011), In situ quantification of supraglacial cryoconite morphodynamics using time-lapse imaging: an example from Svalbard, *J. Glaciol.*, *57*(204), 651–657, doi:http://dx.doi.org/10.3189/002214311797409695.

Ménégoz, M. et al. (2014), Snow cover sensitivity to black carbon deposition in the Himalayas: from atmospheric and ice core measurements to regional climate simulations, *Atmos. Chem. Phys.*, *14*(8), 4237–4249, doi:10.5194/acp-14-4237-2014.

Middleton, E. M., S. G. Ungar, D. J. Mandl, L. Ong, S. W. Frye, P. E. Campbell, D. R.

Landis, J. P. Young, and N. H. Pollack (2013), The earth observing one (EO-1) satellite mission: Over a decade in space, *IEEE J. Sel. Top. Appl. Earth Obs. Remote Sens.*, *6*(2), 243–256, doi:10.1109/JSTARS.2013.2249496.

Ming, J., Z. Du, C. Xiao, X. Xu, and D. Zhang (2012), Darkening of the mid-Himalaya glaciers since 2000 and the potential causes, *Environ. Res. Lett.*, *7*(1), 014021, doi:10.1088/1748-9326/7/1/014021.

Ming, J., Y. Wang, Z. Du, T. Zhang, W. Guo, C. Xiao, X. Xu, M. Ding, D. Zhang, and W. Yang (2015), Widespread Albedo Decreasing and Induced Melting of Himalayan Snow and Ice in the Early 21st Century, *PLoS One*, *10*(6), e0126235, doi:10.1371/journal.pone.0126235.

Nagatsuka, N., N. Takeuchi, T. Nakano, K. Shin, and E. Kokado (2014), Geographical variations in Sr and Nd isotopic ratios of cryoconite on Asian glaciers, *Environ. Res. Lett.*, *9*(4), 045007, doi:10.1088/1748-9326/9/4/045007.

Nair, V. S., S. S. Babu, K. K. Moorthy, A. K. Sharma, and A. Marinoni (2013), Black carbon aerosols over the Himalayas: direct and surface albedo forcing, *Tellus B*, *65*, doi:10.3402/tellusb.v65i0.19738.

Negi, H. S., H. S. Jassar, G. Saravana, N. K. Thakur, Snehmani, and a. Ganju (2013), Snow-cover characteristics using Hyperion data for the Himalayan region, *Int. J. Remote Sens.*, *34*(6), 2140–2161, doi:10.1080/01431161.2012.742213.

Nordenskiöld, A. E. (1883), Nordenskiold on the inland ice of Greenland., *Science*, *2*(44), 732–8, doi:10.1126/science.ns-2.44.732.

Oerlemans, J., R. H. Giesen, and M. R. Van Den Broeke (2009), Retreating alpine glaciers: increased melt rates due to accumulation of dust (Vadret da Morteratsch, Switzerland), *J. Glaciol.*, *55*(192), 729–736, doi:10.3189/002214309789470969.

Painter, T. H., A. P. Barrett, C. C. Landry, J. C. Neff, M. P. Cassidy, C. R. Lawrence, K. E. McBride, and G. L. Farmer (2007), Impact of disturbed desert soils on duration of mountain snow cover, *Geophys. Res. Lett.*, *34*(12), L12502, doi:10.1029/2007GL030284.

Painter, T. H., J. S. Deems, J. Belnap, A. F. Hamlet, C. C. Landry, and B. Udall (2010), Response of Colorado River runoff to dust radiative forcing in snow., *Proc. Natl.*

Acad. Sci. U. S. A., *107*(40), 17125–30, doi:10.1073/pnas.0913139107.

Painter, T. H., M. G. Flanner, G. Kaser, B. Marzeion, R. A. VanCuren, and W. Abdalati (2013), End of the Little Ice Age in the Alps forced by industrial black carbon., *Proc. Natl. Acad. Sci. U. S. A.*, *110*(38), 15216–21, doi:10.1073/pnas.1302570110.

Paul, F., A. Kääb, and W. Haeberli (2007), Recent glacier changes in the Alps observed by satellite: Consequences for future monitoring strategies, *Glob. Planet. Change*, *56*(1-2), 111–122, doi:10.1016/j.gloplacha.2006.07.007.

Pfeffer, W. T. et al. (2014), The Randolph Glacier Inventory : a globally complete inventory of glaciers, , *60*(221), 537–552, doi:10.3189/2014JoG13J176.

Polashenski, C. M., J. E. Dibb, M. G. Flanner, J. Y. Chen, Z. R. Courville, A. M. Lai, J. J. Schauer, M. M. Shafer, and M. Bergin (2015), Neither dust nor black carbon causing apparent albedo decline in Greenland's dry snow zone; implications for MODIS C5 surface reflectance, *Geophys. Res. Lett.*, *42*(21), n/a–n/a, doi:10.1002/2015GL065912.

Segawa, T., S. Ishii, N. Ohte, A. Akiyoshi, A. Yamada, F. Maruyama, Z. Li, Y. Hongoh, and N. Takeuchi (2014), The nitrogen cycle in cryoconites: Naturally occurring nitrification-denitrification granules on a glacier, *Environ. Microbiol.*, *16*, 3250–3262, doi:10.1111/1462-2920.12543.

Singh, S. M., J. Sharma, P. Gawas-Sakhalkar, A. K. Upadhyay, S. Naik, S. M. Pedneker, and R. Ravindra (2013), Atmospheric deposition studies of heavy metals in Arctic by comparative analysis of lichens and cryoconite, *Environ. Monit. Assess.*, *185*, 1367–1376, doi:10.1007/s10661-012-2638-5.

Sterle, K. M., J. R. McConnell, J. Dozier, R. Edwards, and M. G. Flanner (2013), Retention and radiative forcing of black carbon in eastern Sierra Nevada snow, *Cryosph.*, *7*(1), 365–374, doi:10.5194/tc-7-365-2013.

Stibal, M., M. Šabacká, and J. Žárský (2012), Biological processes on glacier and ice sheet surfaces, *Nat. Geosci.*, *5*(11), 771–774, doi:10.1038/ngeo1611.

Takeuchi, N., S. Kohshima, and K. Seko (2001), Structure, Formation, and Darkening Process of Albedo-Reducing Material (Cryoconite) on a Himalayan Glacier: A Granular Algal Mat Growing on the Glacier, *Arctic, Antarct. Alp. Res.*, *33*(2), 115–122, doi:10.2307/1552211.

Takeuchi, N., N. Nagatsuka, J. Uetake, and R. Shimada (2014), Spatial variations in impurities (cryoconite) on glaciers in northwest Greenland, *Bull. Glaciol. Res.*, *32*(0), 85–94, doi:10.5331/bgr.32.85.

Tedesco, M., S. Doherty, X. Fettweis, P. Alexander, J. Jeyaratnam, E. Noble, and J. Stroeve (2015), The darkening of the Greenland ice sheet: trends, drivers and projections (1981–2100), *Cryosph. Discuss.*, *9*(5), 5595–5645, doi:10.5194/tcd-9-5595-2015.

Varga, G., C. Cserháti, J. Kovács, J. Szeberényi, and B. Bradák (2014), Unusual Saharan dust events in the Carpathian Basin (Central Europe) in 2013 and early 2014, *Weather*, *69*(11), 309–313, doi:10.1002/wea.2334.

Vermote, E. F., D. Tanre, J. L. Deuze, M. Herman, and J.-J. Morcette (1997), Second Simulation of the Satellite Signal in the Solar Spectrum, 6S: an overview, *IEEE Trans. Geosci. Remote Sens.*, *35*(3), 675–686, doi:10.1109/36.581987.

Wientjes, I. G. M., R. S. W. Van de Wal, G. J. Reichart, a. Sluijs, and J. Oerlemans (2011), Dust from the dark region in the western ablation zone of the Greenland ice sheet, *Cryosph.*, *5*(3), 589–601, doi:10.5194/tc-5-589-2011.

Zarsky, J. D., M. Stibal, A. Hodson, B. Sattler, M. Schostag, L. H. Hansen, C. S. Jacobsen, and R. Psenner (2013), Large cryoconite aggregates on a Svalbard glacier support a diverse microbial community including ammonia-oxidizing archaea, *Environ. Res. Lett.*, *8*(3), 035044, doi:10.1088/1748-9326/8/3/035044.

Zemp, M., S. U. Nussbaumer, K. Naegeli, I. Gärtner-Roer, F. Paul, M. Hoelzle, and W. Haeberli (2013), *Glacier Mass Balance Bulletin No. 12 (2010–2011)*, Zurich, Switzerland.

5 Summary and conclusions

In this thesis, I developed different methodologies for determining the impact of light-absorbing impurities on snow and ice in the European Alps. These analyses were never applied in this geographical context, and it is widely accepted that the Alps are very sensitive to climatic and environmental changes. Results showed that seasonal input of mineral dust can strongly alter the radiative properties of snow and ice, generating high instantaneous radiative forcings. This process has the ability to accelerate the melting of seasonal snow and glaciers ice, through the direct decrease of reflected energy and consequent increasing in absorption of incident radiation, that enhance the phase transition from ice to water.

Important findings regard the possibility to monitor this process from multi-scale observations, that is from ground, UAV, digital photography and satellite data. The field campaigns organized during the Ph.D. allowed to directly observing the impact of impurities on snow and ice, in order to develop a simple and easily applicable spectral index, the Snow Darkening Index (SDI). Results from the campaigns on the Morteratsch glacier allowed us to observe directly and for the first time the impact of cryoconite formation and disruption on the albedo of a mountain glacier in the Alps. In fact, to date no scientific literature analyse the impact of cryoconites on the radiative properties of ice using proximal and remote sensing data in the European Alps. Furthermore, the geochemical characterization allowed us to guess the source of this non-ice material, in particular regarding the input of local mineral source.

The impact of light-absorbing impurities on the cryosphere is gaining interest from the scientific community; in particular, in relation to the darkening processes observed in

Greenland Ice Sheet, where albedo has been observed to decrease in the last decades. Possible mechanisms proposed to explain these observations regards the direct impact of impurities transported from lower latitudes and the outcropping of bare ice, that resurfaces past depositions, lowering the albedo and promoting the melting.

The processes described in this thesis can occur also at a planetary scale in large icy bodies of the solar system (i.e. Europa and Enceladus). In fact, in these harsh environments ice and dust actively interact producing effects, whose analogs can be studied on Earth's surface. In particular, Jupiter's moon Europa is globally covered by a thick cover of ice, where dust is deposited from Europa's cryovolcanoes and interplanetary transport (i.e. from the nearby Io moon, which is the most volcanically active planetary body of the solar system). Methodologies developed in this thesis (e.g. SDI mapping, instantaneous radiative forcing calculation) will be applied to multi and hyperspectral data collected by Galileo spacecraft (e.g. from the Solid State Imager and the Near-Infrared Mapping Spectrometer) to study the impact of dust on ice in the outer solar system. Furthermore, Europa is suspected to hold a buried ocean under the ice; and this is thought to be able to sustain life. Possible cryoconite-like structures could have been formed also on the surface of Europa. This is particularly important in relation to the fact the life on Earth resisted during long "Snow-ball Earth periods" (e.g. Proterozoic eon, around 715 million years ago), when Earth was fully covered by snow and ice.

Appendix 1: Further research

Power law distributions of wildfires across Europe: benchmarking a land surface model with observed data

Abstract

Monthly wildfire burned area frequency is here modeled with a power law distribution and scaling exponent across different European biomes are estimated. Data sets, spanning from 2000 to 2009, comprehend the inventory of monthly burned areas from the European Forest Fire Information System (EFFIS) and simulated monthly burned areas from a recent parameterization of a Land Surface Model (LSM), that is the Community Land Model (CLM). Power law exponents are estimated with a Maximum Likelihood Estimation (MLE) for different European biomes. The characteristic fire size (CFS), i.e. the area that most contributes to the total burned area, was also calculated both from EFFIS and CLM data set. We used the power law fitting and the CFS analysis to benchmark CLM model against the EFFIS observational wildfires data set available for Europe.

Results for the EFFIS data showed that power law fittings holds for 2-3 orders of magnitude in the Boreal and Continental ecoregions, whereas the distribution of the Alpine, Atlantic are fitted only in the upper tail. Power law instead is not a suitable model for fitting CLM simulations.

CLM benchmarking analysis showed that the model strongly overestimates burned areas and fails in reproducing size-frequency distribution of observed EFFIS wildfires. This benchmarking analysis showed that some refinements in CLM structure (in particular regarding the anthropogenic influence) are needed for predicting future wildfires

scenarios, since the low spatial resolution of the model and differences in relative frequency of small and large fires can affect the reliability of the predictions.

Introduction

Wildfire size frequency has been studied since fire data have been regularly collected and then analyzed to gain a mechanistic understanding of the underlying process and to develop predictive models of this complex natural phenomenon [*Cumming*, 2001; *Moritz et al.*, 2005; *Zinck and Grimm*, 2009; *McKenzie et al.*, 2011]. The spatio-temporal distribution of wildfires in a certain area can be used to characterize the fire regime. Although widely used, this term still lacks a clear and widely accepted definition [*Krebs et al.*, 2010]. Fire regimes are mainly a function of land cover (e.g. type of fuel) and climate (temperature, precipitation, duration of the dry-wet season, etc.), but they also depend on socio-economic factors such as population density, agricultural practices and so on [*Pausas and Keeley*, 2009; *Bowman et al.*, 2011]. Recent climate change has been found to impact wildfire regimes and future increases in global temperature coupled with more frequent droughts are expected to increase fire activity [*Flannigan et al.*, 2000], in particular in Mediterranean landscapes [*Pausas*, 2004]. Despite some attempts based both on satellite [*Chuvieco et al.*, 2008] and inventory data [*Malamud et al.*, 2005], to date there is no well-established/quantitative method for classifying fire regimes across different climates. A proper classification method is needed for the quantification of climate change impact on ecosystems and wildfire scenarios [*Migliavacca et al.*, 2013a; *Yang et al.*, 2014].

Many difficulties are encountered in the modeling of wildfires because of the intrinsic complexity of this system, in which many environmental and social variables are involved in the ignition, propagation and suppression of fires. Some models were formulated to describe and predict wildfire spatial and temporal frequencies. According to *Zinck and Grimm* [2009] these models can be classified in two categories: the fire ecology approach and the statistical physics approach. The former class of models aims to reproduce

environmental interactions between the physical status of vegetation and forcing agents that lead to wildfires [*Peterson*, 2002; *Thonicke et al.*, 2008, 2010]; the latter class of models analyzes emergent properties of wildfire using information from fire catalogs and models them as cellular automata [*Bak et al.*, 1987, 1990; *Drossel and Schwabl*, 1992].

Regarding the latter category of models, *Bak et al.* [1990] proposed an interpretation of the spatial distribution of wildfires involving the theory of Self-Organized Criticality (SOC). This theory was first formalized by *Bak et al.* [1987] for the explanation of 1/*f* noise, using the analogy of the "sand pile" model, and then widely applied in various fields [*Newman*, 1996; *Jørgensen et al.*, 1998; *Hergarten*, 2002; *Turcotte and Malamud*, 2004; *Pueyo*, 2007]. In this framework, a simple dynamical system accumulates energy (and mass) for a certain period of time and then energy is dissipated as a fractal [*Bak et al.*, 1990] generating scale invariance in events magnitude (*i.e.* non-existence of a characteristic size of the process).

Emergent properties, such as the frequency-size scaling, can be revealed searching for power law distributions in empirical data. Those distributions have been widely found in nature and these occurrences have often been linked to scale invariance and fractals. Power law theoretical background has been applied to different natural hazards [*Turcotte and Malamud*, 2004], such as earthquakes [*Gutenberg and Richter*, 1956], fracture systems [*Bonnet et al.*, 2001], landslides [*Guzzetti et al.*, 2002; *Malamud et al.*, 2004; *Frattini and Crosta*, 2013], rock and snow avalanches [*Crosta et al.*, 2007; *Birkeland*, 2002], tropical cyclones [*Corral et al.*, 2010] and wildfires [*Malamud*, 1998]. For the latter, the scaling exponent of the power law has been estimated from different data sets in various geographic contexts [*Malamud*, 1998; *Ricotta et al.*, 1999, 2001; *Song et al.*, 2001, 2006; *Corral et al.*, 2008; *Fiorucci et al.*, 2008; *Lin and Rinaldi*, 2009]. Scaling exponents have also been also interpreted as a proxy of fire regimes [*Hantson et al.*, 2015] in North America [*Malamud et al.*, 2005; *Millington et al.*, 2006] and in the Iberian Peninsula [*Moreno et al.*, 2011]. Nevertheless, the existence of a power law

scaling in wildfires has been questioned by several authors [*Reed and McKelvey*, 2002; *Benavent-Corai et al.*, 2007; *McKenzie and Kennedy*, 2012; *Lehsten et al.*, 2014] and some uncertainties still remain about their frequency distribution. For example, *Reed and McKelvey* (2002) suggested that it is necessary to have a constant extinguishment-growth rate ratio (i.e. fire suppression and vegetation recovery are constant in space and time) to hold a power law at all sizes of burned areas. Since it is difficult for both extinguishment and growth to be spatially and temporally constant, a power law is not expected to hold for the entire range of fire size. Recently, *Lehsten et al.* [2014] proposed an alternative statistics, the Characteristic Fire Size (CFS), to measure the fire size that contributes the most to the total burned area. CFS in the pan-Boreal area showed to explain the distribution of wildfires better than a power law distribution, using two independent inventory datasets.

Regarding the fire models implemented in Land Surface Models (LSM), such as the Community Land Model (CLM), different comparisons between observed and simulated data have been performed by many authors [*Kloster et al.*, 2010; *Thonicke et al.*, 2010; *Migliavacca et al.*, 2013b]. The ability of a LSM to mimic realistic wildfires dynamic has been questioned, and further comparison are needed to assess the reliability of LSM prediction for future global climate scenarios.

Recently *Luo et al.* [2012] proposed a framework methodology to benchmark LSM; those benchmark analyses aim to: (i) target aspects of model performance to be evaluated, (ii) define a set of benchmarks as references to test model performance, (iii) compare performance skills among models to identify model strengths and deficiencies, and (iv) propose model improvements. As scaling behavior of natural hazard represents an important insight in the complexity of this natural phenomenon, those scaling properties can be used as a benchmark for LSM. At date, only a work by *Fletcher et al.* [2014] incorporates power law scaling in dynamic global vegetation models (DGVMs), observing promising results for the Amazonian region.

In this paper, we benchmark one version of the CLM model with power law scaling exponent and Characteristic Fire Size (CFS) calculations using a well-established observational data set of forest and non-forest wildfires (the European Forest Fire Information System, EFFIS) *[McInerney et al., 2013; Camia et al., 2014]*. In particular, one criterion for model benchmarking is to evaluate how model structures are able to reproduce the relationships between a set of particular variables against a set of benchmarks, the latter derived from observed data. For this reason, we evaluated whether a LSM is able to mimic the probability distributions of wildfires in Europe that emerges from the analysis of a well-established observational dataset. The LSM here used is a recent parameterization of CLM for its specific application in Europe [*Migliavacca et al.*, 2013a, 2013b]. The comparison is performed because, although the model has been successfully applied to simulate the mean burned area and its relationship with environmental and climatic conditions [*Kloster et al.*, 2010; *Migliavacca et al.*, 2013b], poor performances have been reported in the description of interannual variability and severe fire seasons [*Migliavacca et al.*, 2013b]. In particular, in Europe severe fire seasons characterized by large fire events [*San-Miguel-Ayanz et al.*, 2013] are source of a great concern in the scientific community because of the direct link with climate extremes (e.g. 2003 and 2010 heat waves).

Data Sets and classifications

EFFIS inventory data

The European Fire Database contains information on forest and grassland fires compiled by European Union Member States and by other European countries within the framework of the European Forest Fire Information System (EFFIS) [*Camia et al.*, 2014]

EFFIS, the European Commission reference system for pan-European fire information, is a modular decision support system that monitors fires at a continental scale supporting fire management across Europe with the contributions of national forest fire services in the single countries [*McInerney et al.*, 2013]. In the EFFIS dataset, forest fires are defined

as uncontrolled vegetation fires spreading wholly or in part on forest and/or other wooded land. Grasslands and shrublands are also included, while agricultural land is excluded from the fire statistics. We imposed a minimum fire size for data analysis equal to 1 hectare, and they are often affected by undersampling. Fire size is the total burned area in hectares split into the main land cover categories affected.

Every year, contributing countries submit fire data derived from the collection of individual fire records, which are routinely compiled by local fire fighters after fires have been extinguished. Data are checked, stored and managed by the Joint Research Centre (JRC) within the European Fire Database of EFFIS.

Among the available data, we used monthly totals of burned area from 2000 to 2009 in order to have a temporal resolution equal to the LSM. The EFFIS data were aggregated at NUTS (Nomenclature of Territorial Units for Statistics, EUROSTAT, version 2006) level 3, which correspond to local administrative units of variable extent.

CLM simulated data set

The model simulations conducted in this study were performed with a modified version of CLM version 3.5 [e.g., *Stöckli et al.*, 2008] extended with a carbon-nitrogen biogeochemical model [*Thornton et al.*, 2007, 2009; *Randerson et al.*, 2009]. The prognostic treatment of fires is based on the algorithm developed by *Kloster et al.* [2010] and modified by *Migliavacca et al.* [2013b] for its application in Europe, where the model has been successfully applied to simulate fires for the present climate. Briefly, the model simulates burned area as a function of population density, soil moisture, biomass available to burn and wind-speed. The runs used in this study refer to the period 2000–2009, and were conducted at a spatial resolution of 0.9 × 1.2 degrees (Gaussian grid). CLM was forced by the ERA-Interim reanalysis obtained from the European Centre for Medium-Range Weather Forecasts (ECMWF) [*Dee et al.*, 2011]. Specifically, six hourly data of air temperature, wind speed, specific humidity and atmospheric pressure, as well as three hourly total of incoming shortwave radiation and precipitation were used.

Population density data were obtained from the HYDE data set [*Goldewijk*, 2001] and regridded to match the model resolution applied in this study. The spin-up of the model was conducted according to *Migliavacca et al.* [2013b].

Classification

Both EFFIS and CLM data sets were classified using a simplified version of the climatic stratification proposed by [*Metzger et al.*, 2005], also known as the "Environmental Stratification of Europe". This classification is based on a principal component analysis and a cluster analysis of available environmental variables. The original 13 environmental zones were merged into 5 classes (Figure 1): Continental, Boreal, Atlantic, Alpine and Mediterranean, in order to resemble principal biomes in Europe and to avoid highly fragmented classes that are incompatible with LSM resolution.

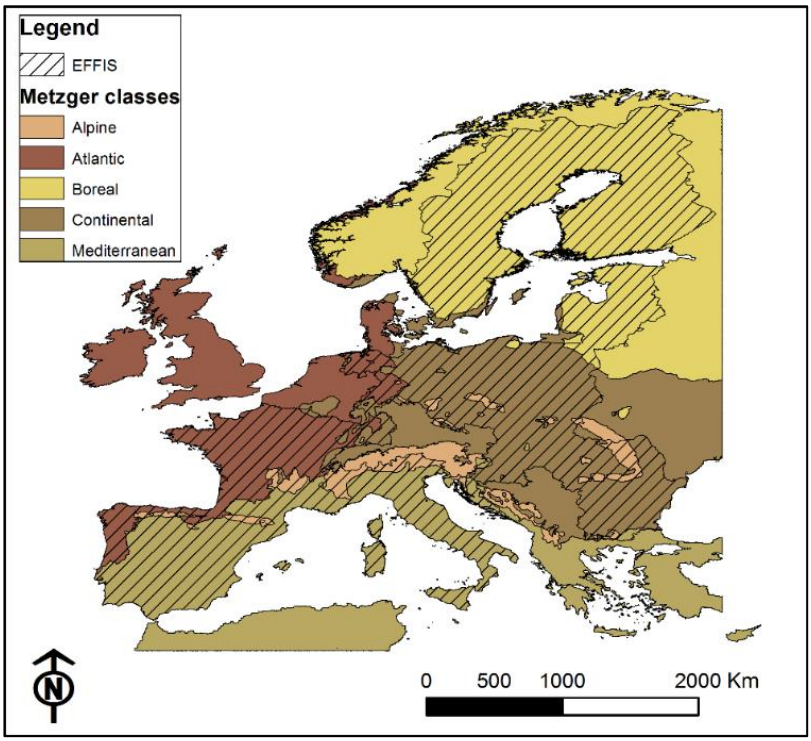

Figure 1 Climatic classification of European environment [*Metzger et al.*, 2005].The 5 class stratification used here include Continental, Boreal, Atlantic, Alpine and Mediterranean. Shaded areas represent the available EFFIS data set in the considered period (2000-2009).

Power law fitting

Power law scaling exponents are expected to reveal emerging properties of complex systems. In this framework, different eco-climatic classes are expected to show different power law coefficients. Regarding wildfires: higher (absolute) values of the exponents could be interpreted as an indicator of a greater incidence of small monthly burned area with respect to the total burned area; conversely, lower exponents will reveal that the contribution of large extreme events to the total burned area is greater.

Power law exponents are here estimated using a Maximum Likelihood Estimation (MLE) [*Clauset et al.*, 2009], in particular we used recent methodology based on MLE applied to binned data [*Virkar and Clauset*, 2014].

Power law distributions are characteristic probability density distribution functions that can be expressed as:

$$p(x) \propto x^{-\alpha}$$

where x is the measured or simulated quantity and α is a constant that assumes real values. Values of α are informative about the underlying process since they are closely related to scale invariance. In fact, when $\alpha < 2$, the probability distribution of x is characterized by all infinitive statistical moments, when $2 \leq \alpha < 3$, the first moment (i.e. the mean) exists and all the other moments are infinite. Scale invariance occurrs when the probability $p(x)$ of an event of dimension x is proportional to the probability $p(Cx)$ of an event of dimension Cx, in the formula:

$$p(x) \propto p(Cx)$$

Consequently, in the dimension range of x in which the power law holds, the characteristic size of the process cannot be calculated (non-existence of the mean) and the probability of an event of size x occurring is proportional to that of an event of size Cx.

Clauset et al. [2009] proposed a unified method to fit power law distributions in empirical data, then modified by *Virkar and Clauset* [2014] for the application to binned data. Those methods have been largely applied by researchers interested in power law distribution and it can be summarized as follows. The estimated power law $\hat{\alpha}$ scaling exponent is calculated with a Maximum Likelihood Estimation (MLE):

$$\hat{\alpha} = 1 + n\left[\sum_{i=1}^{n} \ln \frac{x_i}{x_{\min}}\right]^{-1}$$

where x_i, $i = 1,2,..n$ are the observed values of x such as $x_i \geq x_{\min}$. The goodness of fit is evaluated with a *p-value* from Kolmogorov-Smirnov statistics [*Press et al.*, 2002] that measures the distance D between the distribution of the empirical data and the hypothesized model (characterized by the estimated $\hat{\alpha}$ and $x_{\min}$). The *p-value* is defined as the fraction of the synthetic distances that are larger than the empirical distance. If the *p-value* is larger than 0.1, the fitting is statistically significant since the difference between the empirical data and the model can be attributed to statistical fluctuations alone.

Different probability distributions were tested against the power law. In particular, we here tested the lognormal, the exponential, the power law with exponential cut-off and the stretched exponential (Weibull) as possible competitors to the power law. Those functions are listed in Table 1.

The comparison is made by calculating the logarithm of the ratio of the two likelihoods (Loglikelihood Ratio, LR), since it provides a simple test statistic for discriminating power law from other distributions. LR assumes positive values if the first distribution (the power law) better fits the data with respect to another distribution, it is indistinguishable from zero in the event of a tie. The significance of this comparison is then assessed using the method proposed by *Vuong* [1989].

Function name	Functional form f(x)
Power law with cutoff	$x^{-\alpha}e^{-\lambda x}$
Exponential	$e^{-\lambda x}$
Stretched exponential	$x^{\beta-1}e^{-\lambda x^{\beta}}$
Lognormal	$\frac{1}{x}e^{\left[-\frac{(\ln x-\mu)^2}{2\sigma^2}\right]}$

Table 1 Alternative probability distributions tested against the power law.

Data binning represents a delicate topic in power law research. Here we applied a standardized and objective binning scheme based on 20 bins distributed as a logarithm between the minimum and the maximum value of burned area for each class. This method is consistent with previous works that analyzed power law distributions in wildfires [*Ricotta et al.*, 1999; *Malamud et al.*, 2005; *Moreno et al.*, 2011].

It is important to underline that the method of fitting here applied aims to detect the power law above a minimum bin value. The method assumes that only a minimum threshold exists and only the upper tail of the distribution is fitted by a power law or an alternative distribution.

The code for fitting power laws and testing alternative distribution was iteratively applied to each ecological class both for EFFIS and for CLM data sets. Then, the inverse cumulative distribution functions (CDF) were represented and results were compared.

Characteristic Fire Size

Recently, Lehsten et al. [2014] proposed a novel statistic to analyze wildfires size distribution called the Characteristic Fire Size (CFS). The authors claim that whether the CFS is normally distributed, this feature can be used as support for rejection the power law distribution of fire sizes. Here we calculate the CFS with the formula:

$$CFS_i = n_f(i)\langle m(i)\rangle$$

Where $n_f(i)$ is the burned areas in the *i-th* bin, and $\langle m(i)\rangle$ is the mean fire size in that bin. Representing the distribution of the CFS_i as a function of each bin, Lehsten et al. [2014] showed that this is approximated by a normal distribution for different pan-Boreal ecoregions. The maximum value of CFS_i can be used to represent the fire size that most contributes to the burned area, hereafter simply referred as CFS. In case of a power law distribution, CFS would show a linear pattern in a log-linear plot.

We calculated CFS for both CLM and EFFIS data, using the same binning scheme described in Section 3. Results are then are compared and CFS are spatially represented at European scale.

Results

First basic comparisons between EFFIS and CLM were made representing the two time series of sum of monthly burned area for the different ecoregions here analyzed (Figure 2). As already reported using an administrative stratification [*Migliavacca et al.*, 2013b], CLM strongly overestimates burned areas. We found this feature to hold true also for the climatic stratification applied here. In ecoregions characterized by a little fire seasonality (i.e. Alpine, Atlantic and Continental), CLM badly reproduce EFFIS time series. For the Boreal domain, where fires spread mostly in the summer season and are almost absent during the winter and autumn, CLM qualitatively reproduces this trend observed in EFFIS data. Regarding the Mediterranean ecoregion, the strong seasonality of monthly burned area is reproduced by CLM. Further detailed and quantitative comparisons between EFFIS and CLM can be found in *Migliavacca et al.* [2013b].

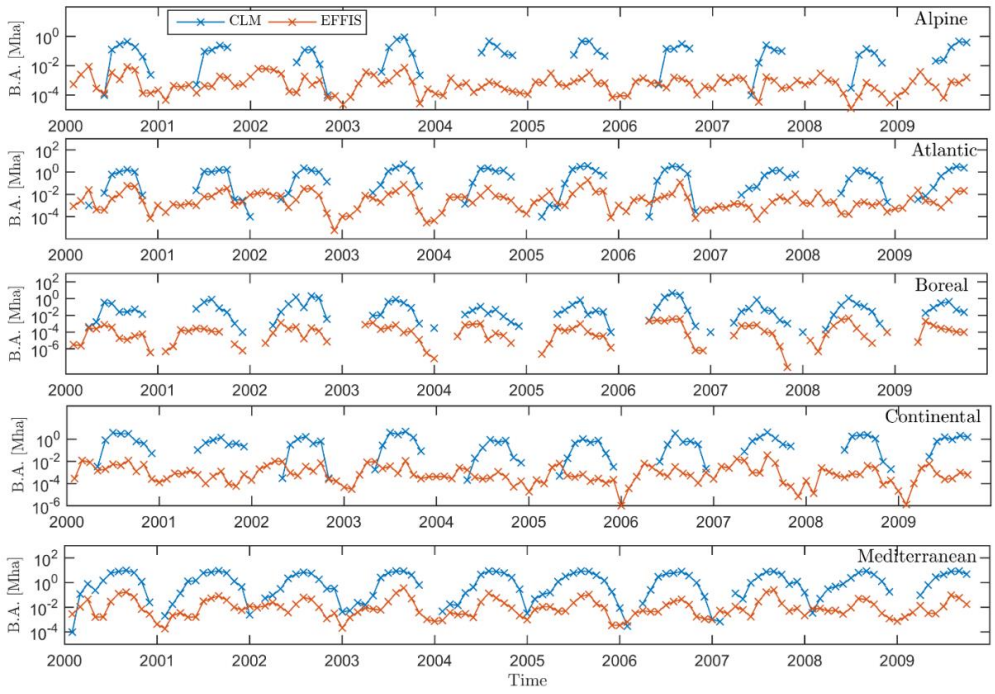

Figure 2 Monthly burned area time series for different ecoregions across Europe for the EFFIS (orange line) and CLM (blue line) data set. Note that ordinates are represented in a logarithmic scale.

The inverse cumulative distribution functions (CDF) of monthly burned areas are shown in Figure 3. These results were obtained with the MLE method [*Virkar and Clauset*, 2014] and applied respectively to EFFIS and CLM data aggregated with the simplified Metzger classification [*Metzger et al.*, 2005]. Results for the EFFIS data set (red lines) showed statistical significance (*p-value* of the Kolmogorov-Smirnov test >0.1) for all the classes. Values of the exponent α range from 1.84 to 3.63. Results from the statistical analysis are summarized in Table 1. The minimum values for which the PL holds (b_{min} in Table 1) resulted higher for the Alpine, Atlantic and Mediterranean biomes, instead for the Boreal and Continental biomes we found low values of 40.8 and 29.7 hectares, signifying that also small burned areas can be explained by the PL distribution.

Ecoregion	Alpha	b_{min} [ha]	KS p-value
Alpine	2.75	449.4	**0.79**
Atlantic	2.55	2905.1	**0.62**
Boreal	2.16	40.8	**0.15**
Continental	1.84	29.7	**0.44**
Mediterranean	3.63	6158.5	**0.72**

Table 2 Summary of power law fits for the EFFIS data set. Significant Kolmogorov-Smirnov (KS) p-values are marked in bold.

The ranges of validity for the PL reach about three orders of magnitude for the Continental biome and about two orders for the Atlantic, Alpine and Boreal ecoregions. For the Mediterranean biome, although statistically significant, only one order of magnitude of burned area is explained by the PL distribution. For the Boreal and Continental biomes we found a deviation from the power law fit in the tail of the distribution, often referred as "cut-off".

Regarding CLM data (green lines), power law fits are limited to the upper two bins of the whole distribution, signifying that the power law is not a suitable model for the description of those data and only the fires larger than 10^5 behave like a power law. We accounted these fittings as spurious and non statistically sounding. The shape of the distributions in CLM data showed an overall accentuated curvature with respect to the EFFIS for the Alpine, Atlantic and Mediterranean biomes. Instead, the Boreal and Continental biomes show a less accentuated curvature resembling more the observed EFFIS CDF.

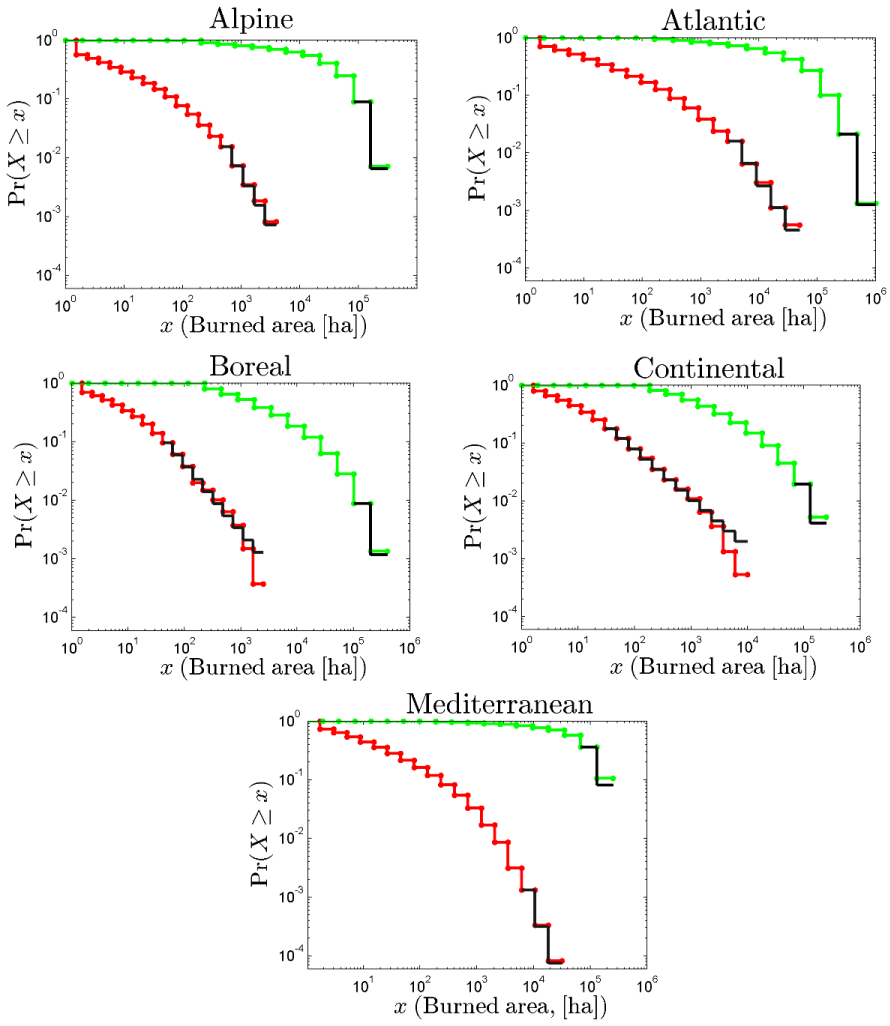

Figure 3 Results of power law fitting for the EFFIS (red lines) and CLM (green lines) data sets for each ecoregion across Europe. In these graphs, the abscissa represents the monthly burned area (in hectares, ha) and the ordinate represents the inverse cumulative distribution function (CDF). Note that both axes are represented in a logarithmic scale.

In Table 3 are presented the Log-likelihood Ratio (LR) for the comparison of PL with other statistical distributions (summarized in Table 1). The positive sign of LR values means that, in the PL validity range, this distribution is favored against the others. The significance of the comparison was assessed by a statistical test [*Vuong*, 1989] that resulted significant for the majority of the comparisons. In some cases, the LR comparison was not statistically significant (p>0.1), meaning that the sign of LR is not

reliable and the test fails to favor one model distribution over the other. The last column of Table 3 shows the number of bins fitted by the power law distribution. We found that the power law holds against other distributions in many cases, but only for the Boreal and Continental biomes a high number of bins is fitted (respectively ten and twelve). For the Alpine and Atlantic biomes, five bins in the tail are fitted and for the Mediterranean biome, only three bins are fitted. We account this latter are spurious and not significant since the fitting regards only a few part of the total data.

Ecoregion	Lognormal	Exponential	Power law with cut off	Stretched exponential	n. bins
Alpine	**4.8*** **	**5.03*** **	**1.73***	**5.39*** **	5
Atlantic	**4.4*** **	**3.65*** **	0.82 ns	**3.8*** **	5
Boreal	**2.8*** **	**5.86*** **	1.52 ns	**1.99*** **	10
Continental	0.37 ns	**9.93 *** **	**3.33 *** **	0.24 ns	12
Mediterranean	**4.61 *** **	**2.78 *** **	0.88 ns	**3.58 *** **	3

Table 3 Logarithms of the likelihood ratio (LR) between a power law distribution and four alternative distribution for the EFFIS data set. Positive values of the ratio means that the power law is favored over the alternatives. Significances are expressed for p<0.001 (***), p<0.01 (**), p<0.05 (*), p>0.1 (non-significant, ns). Last column contains the number of fitted bins in the tail.

Figure 4 shows the CFS plots for each ecoregion in Europe. Regarding EFFIS, the Alpine, Atlantic and Mediterranean biomes feature a similar behavior, where the CFS increases for small burned areas, reaches a maximum value and then decreases again for larger burned areas. For the Mediterranean ecoregion, data show a Gaussian shape, since it is clearly discernible both an increasing and a decreasing trend, with a peak at 2069 ha (logCFS = 3.31). The Boreal ecoregion show a bimodal distribution, the first peaks at 92.2 ha (logCFS = 1.96) and the second one peaks at 729.7 ha (logCFS = 2.86). For the Continental biome, we observed a continuous increasing trend in the CFS, and no decreasing trend, except for two lower values in the uppermost part of the distribution. The marked overestimation of CLM results here in a separation between distributions. Furthermore, CLM data show a Gaussian-like shape, featuring a characteristic event size for all ecoregion, except for the Continental biome, that show an almost continuous increasing trend.

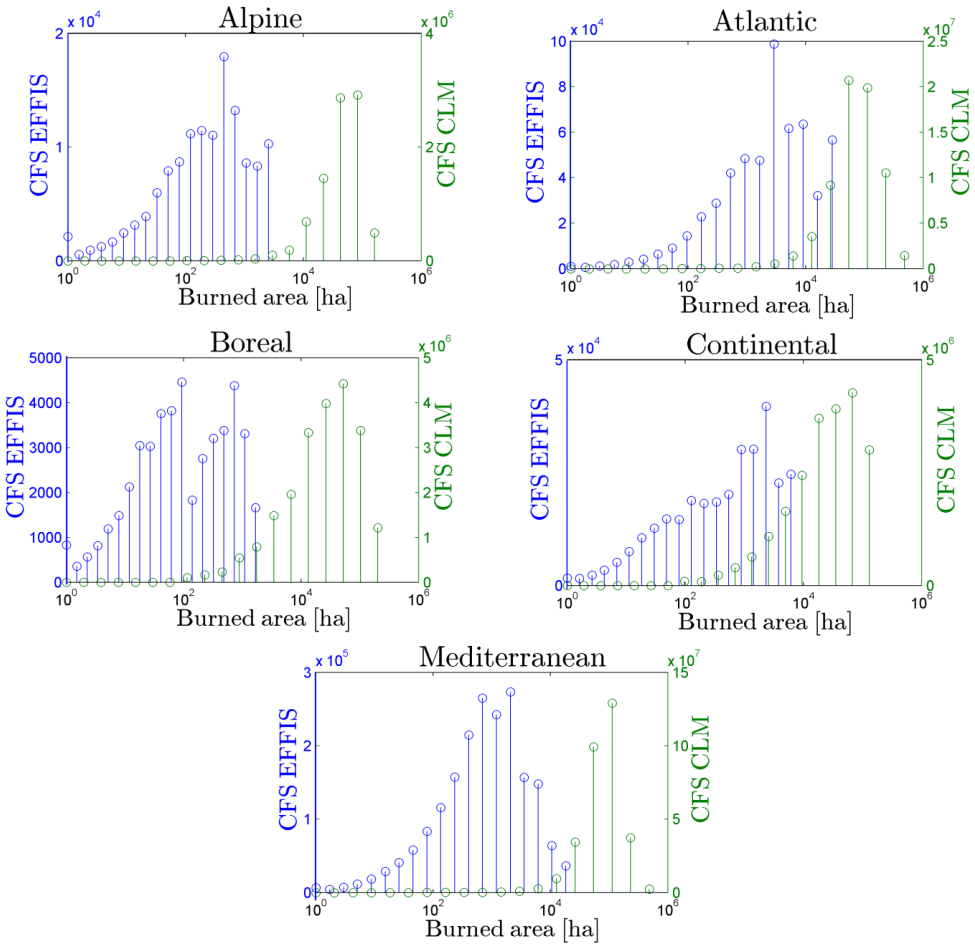

Figure 4 Characteristic Fire Size (CFS) distribution for the EFFIS (blue lines) and for the CLM (green lines) data. Each plot represents a different ecological region in Europe.

In Figure 5, we show a spatial representation of power law exponents for the EFFIS data set at European scale. A latitudinal gradient is displayed in the map, where higher exponents are associated with lower latitudes and lower exponent are generally associated with higher latitudes. The map of power law exponent for the CLM is not showed here since those fitting resulted non statistically sound.

In Figure 6, a map of CFS for the CLM simulated data is showed. Also in this case, a spatial pattern appears: higher CFS are displayed in the Mediterranean area and lower CFS in

the Continental and Boreal areas. The map of CFS is here showed only for CLM since EFFIS data showed that not all the ecoregion allowed the estimation of a CFS.

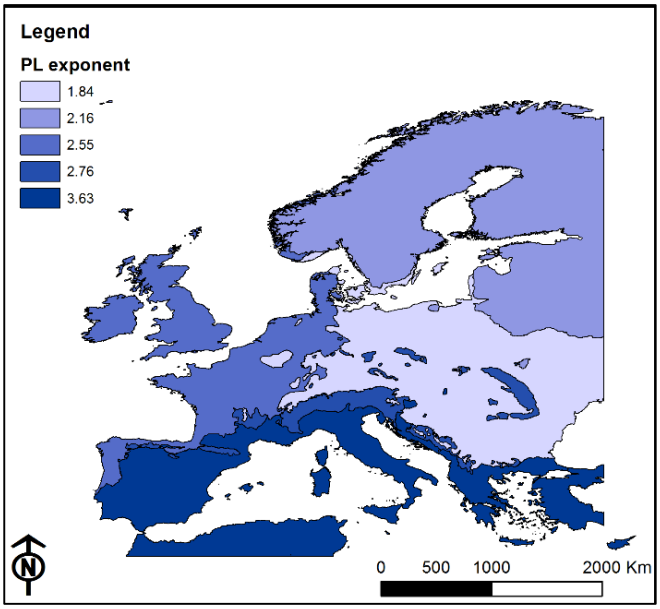

Figure 5 Spatial representation of power law α exponent for the EFFIS data set.

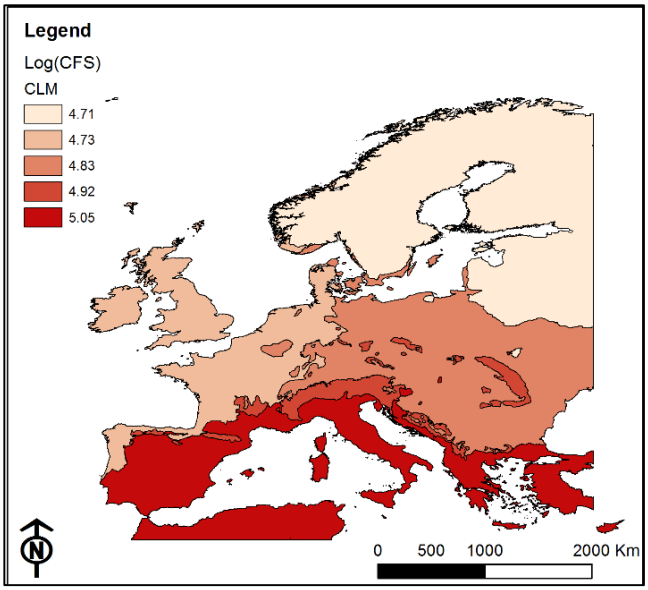

Figure 6 Spatial representation of the Characteristic Fire size (CFS) for the Community Land Model (CLM) burned area simulations.

Discussion

The main objective of this work was to test whether a power law function approximates wildfires distribution across European biomes using two large data set (EFFIS and CLM). In particular, specific object was to use scaling coefficients to benchmark a land surface model (CLM) against a well-established observational data set (EFFIS). These objects address important questions regarding wildfire theoretical background, since whether fire size distribution follows or not a power law distribution in Europe represents a fundamental insight in the complexity of fire dynamics. We also remark that data aggregation plays a fundamental role in power law scaling analysis [*Fiorucci et al.*, 2008; *Cristelli et al.*, 2012], since the more the single classes of data are coherent, the more emergent behavior are likely to appear.

In order to compare EFFIS and CLM dataset, we applied a temporal (monthly) and spatial (ecoregions) aggregation of fires. This aggregation was necessary since CLM does not simulate single fires events but only temporal aggregated sums of burned area in each pixel, and for this specific dataset the aggregation is monthly. We also assumed that different European ecoregions features different fire dynamics and we aimed to characterize them with power laws, as previously applied by Malamud et al. [2005] in North America.

Results from the EFFIS data set showed that wildfires distribution in the Boreal and Continental ecoregions feature a statistically sound power law for many orders of magnitude. The Alpine, Atlantic and Mediterranean ecoregion show a power law only in the upper tail of the distribution and only for a few orders of magnitude, we considered those fit not significant for the purpose of the paper.

We interpret these results (Figures 3 and 5) using the Self Organized Criticality (SOC) theoretical framework. In the Boreal and Continental biomes, wildfires feature a general lower incidence with respect the Mediterranean domain [*De Groot et al.*, 2013]. In the

Boreal and Continental biomes, where mainly evergreen needle leaf and broad leaf forests are present, wildfires are a rare event that can spread also for large areas since the landscape is homogeneous and non-fragmented. Furthermore, those land covers are not very resilient to fire [*Goetz et al.*, 2006; *Lentile et al.*, 2006] and this could act like a feedback mechanism, where fire is prevented by the absence of fuel available to burn due to previous fire. The SOC framework can be applied here since Boreal and Continental ecosystems accumulates (bio)mass (e.g. litter and deadwood) and energy through the seasonal cycles of vegetation by converting the constant input of solar radiation and carbon dioxide. Mass and energy are then dissipated by fire as a fractal, since small wildfires are naturally occurring in large number [*Randerson et al.*, 2012], and when fire spreads it is difficultly suppressed before it can reach large extension because of the small population density and little landscape fragmentation. In any case, very big fire events are prevented through fire suppression by fire-fighters, this may results in a deviation from the power law fit in the tail of the distribution (Figure 3), often referred as a finite-size effect [*Hergarten*, 2002; *Corral et al.*, 2010]. These results support that Northern Europe ecosystem show a more natural fire regime, since the influence of humans is located mainly in the upper tail of the distribution, and fire ignition and spreading is more likely be dictated by climate and fuel availability.

CFS analysis on EFFIS data shows that Boreal and Continental biomes do not feature a characteristic size of monthly wildfires. In particular, the Boreal biome shows a double peak in CFS plot (Figure 4), this could mean that small and large fires follow a different behavior that is instead masked by the cumulative distributions representation (Figure 3). The Continental biome features no characteristic size, this can be used as a further support to the power law scaling.

Southern and Central Europe (SCE) biomes (i.e. Alpine, Atlantic and Mediterranean) do not feature a statistically sound power law, and the CFS revealed that they show a Gaussian-like distribution featuring one characteristic dimension. SCE biomes are highly

fragmented and wildfires are usually triggered and suppressed by human beings [*Ganteaume et al.*, 2013]. We claim that the high population density and landscape fragmentation play an important role in the lack of power law fit in SCE biomes. Wildfires are often triggered by arson or accidental causes (roughly in 90% of the total fires) that involve human being. Furthermore, active fire-fighting methods and efficient fire suppression, strongly limit the spreading of wildfires in different land covers. This results in a strong deviation from a "natural fire regime", where fire spreading is mainly dictated by climate variability and vegetation spatial distribution. Furthermore, these ecosystem are generally highly resilient to fire [*Díaz-Delgado et al.*, 2003; *Di Mauro et al.*, 2014] and repeated fire can happen in the same burn scar from one year to the subsequent, preventing the feedback mechanism described for the Boreal and Continental biomes (Chapin III, 2000). Also in these areas, large fires can occur; those events are possibly escaped from human suppression. For example, events like these can be triggered by extreme heat waves [*Trigo et al.*, 2006; *Barriopedro et al.*, 2011] that create environmental conditions that promote large fires spreading. The CFS analysis showed that for the Mediterranean area a clear characteristic size can be calculated, instead for the Alpine and Atlantic biomes we found some noise in the upper tail of the distribution, that can be related to the incidence of large fires, that is higher than expected in a lognormal distribution. In fact, for those two areas the power law analysis revealed that the scaling holds only in the upper tail with statistical significance, even if only a few bins are fitted by the power law.

Regarding the benchmark analysis of CLM, we used two methodologies: power law fitting and the CFS analysis. From both results we found that in its current formulation, CLM badly reproduce the properties found in the EFFIS data set. In particular, the power law function is not a suitable description of wildfires distribution for all ecoregions in Europe. The fitting is limited to the upper two bins of the distribution, and we accounted it as not enough for a statistically sound fitting. The CFS analysis showed that, using CLM, in all the European ecoregion the mean values of burned area is well behaved, since a

characteristic event size can be calculated from the peak of the Gaussian-like distributions represented in Figure 4.

The model benchmarking strategy applied in this study showed that improvements are needed in using this model for prediction of the distribution of wildfires in Europe. This can be done by developing the model structure, for instance to reduce the overestimation in Central Europe and the lack of description of interannual variability [*Migliavacca et al.*, 2013b]. At the moment, fire suppression is parameterized just as a function of population density; we can suggest that, for example, including the scaling parameter in the model structure can help in limiting fire spreading and in representing in a more realistic way the incidence of wildfires in Europe. Another option is to use a model optimization based on multiple constrains, for instance by including the observed power laws by environmental region to better describe the spatial variability of fire regimes. A pilot work by Fletchet et al. [2014] showed that including the scaling factor in a vegetation model increased the estimation accuracy of burned areas in the Amazonian region.

We also found that spatial representation of alpha exponents calculated from EFFIS data and CFS calculated from CLM clearly depicts differences in fire regime in Europe, as previously found in North America [*Malamud et al.*, 2005; *Millington et al.*, 2006], since they display a latitudinal gradient related to the incidence of climate on fire regimes. In particular, lower scaling coefficient calculated from EFFIS are related to higher latitudes, instead higher CFS values calculated from CLM are related to lower latitudes.

Power law generating mechanisms play a fundamental role in the interpretation of results [*Carlson and Doyle*, 1999, 2002; *Moritz et al.*, 2005]; the fact that heavy-tailed distributions occur in complex systems implies that extreme events occur more frequently than they would in other distribution [*Stumpf and Porter*, 2012]. This is an important issue in understanding the impact and relative frequency of large wildfires in Europe [*San-Miguel-Ayanz et al.*, 2013].

Conclusions

In this paper, we analyzed wildfire distribution across Europe using EFFIS and CLM data. Regarding EFFIS data, we found that cumulative distribution of Boreal and Continental biomes can be approximated by a power law function with statistical significance. Instead, the Mediterranean, Atlantic and Alpine biomes did not show significant fits. We interpreted these results as a result of a feedback mechanism between human management of wildfires and natural fire regime. We benchmarked CLM simulation with observed data, and we found that the model does not reproduce the scaling found in the Boreal and Continental biomes, and it strongly overestimates burned areas in all biomes. Possible constraints regarding the inclusion of scaling exponents in the model formulation are proposed in order to reduce the spreading of fire using EFFIS observed variability.

Based on theoretical considerations, we can also speculate that, if the power law properly describes wildfire distribution, it would be very unlikely observed at all orders of magnitude in inventory data or simulated monthly burned area that includes anthropogenic influence. Furthermore, since wildfire is a natural hazard with strong human influences both in ignition and suppression, we conclude that a power law scaling behavior is likely observed only for natural environments, and deviation from the power law can be ascribed by the influence of human being on natural fire regimes.

Acknowledgements

I would like to acknowledge the European Commission Joint Research Centre (JRC) for providing the dataset extracted from the European Fire Database of EFFIS.

A full version of this chapter is currently under discussion in *Nonlinear Processes in Geophysics Discussion*:

Di Mauro, B., Fava, F., Frattini, P., Camia, A., Colombo, R., and Migliavacca, M.: Power law distributions of wildfires across Europe: benchmarking a land surface model with observed data, *Nonlin. Processes Geophys. Discuss.*, 2, 1553-1586, doi:10.5194/npgd-2-1553-2015, 2015.

Bibliography

Bak, P., C. Tang, and K. Wiesenfeld (1987), Self-organized criticality: An explanation of the 1/f noise, *Phys. Rev. Lett.*, *59*(4), 381–384, doi:10.1103/PhysRevLett.59.381.

Bak, P., K. Chen, and C. Tang (1990), A forest-fire model and some thoughts on turbulence, *Phys. Lett. A*, *147*(5-6), 297–300, doi:10.1016/0375-9601(90)90451-S.

Barriopedro, D., E. M. Fischer, J. Luterbacher, R. M. Trigo, and R. García-Herrera (2011), The hot summer of 2010: redrawing the temperature record map of Europe., *Science*, *332*(6026), 220–4, doi:10.1126/science.1201224.

Benavent-Corai, J., C. Rojo, J. Suárez-Torres, and L. Velasco-García (2007), Scaling properties in forest fire sequences: The human role in the order of nature, *Ecol. Modell.*, *205*(3-4), 336–342, doi:10.1016/j.ecolmodel.2007.02.028.

Birkeland, K. W. (2002), Power-laws and snow avalanches, *Geophys. Res. Lett.*, *29*(11), 1554, doi:10.1029/2001GL014623.

Bonnet, E., O. Bour, N. E. Odling, P. Davy, I. Main, P. Cowie, and B. Berkowitz (2001), Scaling of fracture systems in geological media, *Rev. Geophys.*, *39*(3), 347, doi:10.1029/1999RG000074.

Bowman, D. M. J. S. et al. (2011), The human dimension of fire regimes on Earth., *J. Biogeogr.*, *38*(12), 2223–2236, doi:10.1111/j.1365-2699.2011.02595.x.

Camia, A., J. San-Miguel-Ayanz, and T. Durrant (2014), *The European Fire Database: technical specifications and data submission*, Luxemburg.

Carlson, J., and J. Doyle (1999), Highly optimized tolerance: A mechanism for power laws in designed systems, *Phys. Rev. E*, *60*(2), 1412–1427, doi:10.1103/PhysRevE.60.1412.

Carlson, J. M., and J. Doyle (2002), Complexity and robustness., *Proc. Natl. Acad. Sci. U. S. A.*, *99 Suppl 1*(90001), 2538–45, doi:10.1073/pnas.012582499.

Chuvieco, E., L. Giglio, and C. Justice (2008), Global characterization of fire activity: toward defining fire regimes from Earth observation data, *Glob. Chang. Biol.*, *14*(7), 1488–1502, doi:10.1111/j.1365-2486.2008.01585.x.

Clauset, A., C. R. Shalizi, and M. E. J. Newman (2009), Power-Law Distributions in Empirical Data, *SIAM Rev.*, *51*(4), 661–703, doi:10.1137/070710111.

Corral, Á., L. Telesca, and R. Lasaponara (2008), Scaling and correlations in the dynamics of forest-fire occurrence, *Phys. Rev. E*, *77*(1), 016101, doi:10.1103/PhysRevE.77.016101.

Corral, Á., A. Ossó, and J. E. Llebot (2010), Scaling of tropical-cyclone dissipation, *Nat. Phys.*, *6*(9), 693–696, doi:10.1038/nphys1725.

Cristelli, M., M. Batty, and L. Pietronero (2012), There is more than a power law in Zipf., *Sci. Rep.*, *2*, 812, doi:10.1038/srep00812.

Crosta, G. B., P. Frattini, and N. Fusi (2007), Fragmentation in the Val Pola rock avalanche, Italian Alps, *J. Geophys. Res.*, *112*(F1), F01006, doi:10.1029/2005JF000455.

Cumming, S. G. (2001), A parametric model of the fire-size distribution, *Can. J. For. Res.*, *31*, 1297–1303, doi:10.1139/x01-032.

Dee, D. P. et al. (2011), The ERA-Interim reanalysis: configuration and performance of the data assimilation system, *Q. J. R. Meteorol. Soc.*, *137*(656), 553–597, doi:10.1002/qj.828.

De Groot, W. J., M. D. Flannigan, and A. S. Cantin (2013), Climate change impacts on future boreal fire regimes, *For. Ecol. Manage.*, *294*, 35–44, doi:10.1016/j.foreco.2012.09.027.

Díaz-Delgado, R., F. Lloret, and X. Pons (2003), Influence of fire severity on plant regeneration by means of remote sensing imagery, *Int. J. Remote Sens.*, *24*, 1751–1763, doi:10.1080/01431160210144732.

Di Mauro, B., F. Fava, L. Busetto, G. F. Crosta, and R. Colombo (2014), Post-fire resilience in the Alpine region estimated from MODIS satellite multispectral data, *Int. J. Appl. Earth Obs. Geoinf.*, *32*, 163–172, doi:10.1016/j.jag.2014.04.010.

Drossel, B., and F. Schwabl (1992), Self-organized critical forest-fire model., *Phys. Rev. Lett.*, *69*(11), 1629–1632.

Fiorucci, P., F. Gaetani, and R. Minciardi (2008), Regional partitioning for wildfire regime characterization, *J. Geophys. Res.*, *113*(F2), F02013, doi:10.1029/2007JF000771.

Flannigan, M. ., B. . Stocks, and B. . Wotton (2000), Climate change and forest fires, *Sci. Total Environ.*, *262*(3), 221–229, doi:10.1016/S0048-9697(00)00524-6.

Fletcher, I. N., L. E. O. C. Aragão, A. Lima, Y. Shimabukuro, and P. Friedlingstein (2014), Fractal properties of forest fires in Amazonia as a basis for modelling pan-tropical burnt area, *Biogeosciences*, *11*(6), 1449–1459, doi:10.5194/bg-11-1449-2014.

Frattini, P., and G. B. Crosta (2013), The role of material properties and landscape morphology on landslide size distributions, *Earth Planet. Sci. Lett.*, *361*, 310–319, doi:10.1016/j.epsl.2012.10.029.

Ganteaume, A., A. Camia, M. Jappiot, J. San-Miguel-Ayanz, M. Long-Fournel, and C. Lampin (2013), A review of the main driving factors of forest fire ignition over Europe., *Environ. Manage.*, *51*(3), 651–62, doi:10.1007/s00267-012-9961-z.

Goetz, S. J., G. J. Fiske, and A. G. Bunn (2006), Using satellite time-series data sets to analyze fire disturbance and forest recovery across Canada, *Remote Sens. Environ.*, *101*, 352–365, doi:10.1016/j.rse.2006.01.011.

Goldewijk, K. K. (2001), Estimating global land use change over the past 300 years: The HYDE Database, *Global Biogeochem. Cycles*, *15*(2), 417–433, doi:10.1029/1999GB001232.

Gutenberg, B., and C. F. Richter (1956), Magnitude and energy of earthquakes, *Ann. Geophys.*, *9*(1), 1–15, doi:10.4401/ag-5590.

Guzzetti, F., B. D. Malamud, D. L. Turcotte, and P. Reichenbach (2002), Power-law correlations of landslide areas in central Italy, *Earth Planet. Sci. Lett.*, *195*(3-4), 169–183, doi:10.1016/S0012-821X(01)00589-1.

Hantson, S., S. Pueyo, and E. Chuvieco (2015), Global fire size distribution is driven by human impact and climate, *Glob. Ecol. Biogeogr.*, *24*(1), 77–86, doi:10.1111/geb.12246.

Hergarten, S. (2002), *Self-Organized Criticality in Earth Systems*, Springer Berlin Heidelberg, Berlin, Heidelberg.

Jørgensen, S. E., H. Mejer, and S. N. Nielsen (1998), Ecosystem as self-organizing critical systems, *Ecol. Modell.*, *111*(2-3), 261–268, doi:10.1016/S0304-3800(98)00104-5.

Kloster, S., N. M. Mahowald, J. T. Randerson, P. E. Thornton, F. M. Hoffman, S. Levis, P. J. Lawrence, J. J. Feddema, K. W. Oleson, and D. M. Lawrence (2010), Fire

dynamics during the 20th century simulated by the Community Land Model, *Biogeosciences*, *7*(6), 1877–1902, doi:10.5194/bg-7-1877-2010.

Krebs, P., G. B. Pezzatti, S. Mazzoleni, L. M. Talbot, and M. Conedera (2010), Fire regime: history and definition of a key concept in disturbance ecology., *Theory Biosci.*, *129*(1), 53–69, doi:10.1007/s12064-010-0082-z.

Lehsten, V., W. J. de Groot, M. Flannigan, C. George, P. Harmand, and H. Balzter (2014), Wildfires in boreal ecoregions: Evaluating the power law assumption and intra-annual and interannual variations, *J. Geophys. Res. Biogeosciences*, *119*(1), 14–23, doi:10.1002/2012JG002252.

Lentile, L. B., Z. A. Holden, A. M. S. Smith, M. J. Falkowski, A. T. Hudak, P. Morgan, S. A. Lewis, P. E. Gessler, and N. C. Benson (2006), Remote sensing techniques to assess active fire characteristics and post-fire effects, *Int. J. Wildl. Fire*, *15*, 319–345, doi:10.1071/WF05097.

Lin, J., and S. Rinaldi (2009), A derivation of the statistical characteristics of forest fires, *Ecol. Modell.*, *220*(7), 898–903, doi:10.1016/j.ecolmodel.2009.01.011.

Luo, Y. Q. et al. (2012), A framework for benchmarking land models, *Biogeosciences*, *9*(10), 3857–3874, doi:10.5194/bg-9-3857-2012.

Malamud, B. D. (1998), Forest Fires: An Example of Self-Organized Critical Behavior, *Science (80-.).*, *281*(5384), 1840–1842, doi:10.1126/science.281.5384.1840.

Malamud, B. D., D. L. Turcotte, F. Guzzetti, and P. Reichenbach (2004), Landslide inventories and their statistical properties, *Earth Surf. Process. Landforms*, *29*(6), 687–711, doi:10.1002/esp.1064.

Malamud, B. D., J. D. a Millington, and G. L. W. Perry (2005), Characterizing wildfire regimes in the United States., *Proc. Natl. Acad. Sci. U. S. A.*, *102*(13), 4694–9, doi:10.1073/pnas.0500880102.

McInerney, D., J. San-Miguel-Ayanz, P. Corti, C. Whitmore, C. Giovando, and A. Camia (2013), Design and Function of the European Forest Fire Information System, *Photogramm. Eng. Remote Sens.*, *79*(10), 965–973, doi:10.14358/PERS.79.10.965.

McKenzie, D., and M. C. Kennedy (2012), Power laws reveal phase transitions in landscape controls of fire regimes., *Nat. Commun.*, *3*, 726, doi:10.1038/ncomms1731.

McKenzie, D., C. Miller, and D. A. Falk (Eds.) (2011), *The Landscape Ecology of Fire*, Ecological Studies, Springer Netherlands, Dordrecht.

Metzger, M. J., R. G. H. Bunce, R. H. G. Jongman, C. A. Mücher, and J. W. Watkins (2005), A climatic stratification of the environment of Europe, *Glob. Ecol. Biogeogr.*, *14*(6), 549–563, doi:10.1111/j.1466-822X.2005.00190.x.

Migliavacca, M. et al. (2013a), Modeling biomass burning and related carbon emissions during the 21st century in Europe, *J. Geophys. Res. Biogeosciences*, *118*(4), 1732–1747, doi:10.1002/2013JG002444.

Migliavacca, M. et al. (2013b), Modeling burned area in Europe with the Community Land Model, *J. Geophys. Res. Biogeosciences*, *118*(1), 265–279, doi:10.1002/jgrg.20026.

Millington, J. D. A., G. L. W. Perry, and B. D. Malamud (2006), Models, data and mechanisms: quantifying wildfire regimes, *Geol. Soc. London, Spec. Publ.*, *261*(1), 155–167, doi:10.1144/GSL.SP.2006.261.01.12.

Moreno, M. V., B. D. Malamud, and E. a. Chuvieco (2011), Wildfire Frequency-Area Statistics in Spain, *Procedia Environ. Sci.*, *7*, 182–187, doi:10.1016/j.proenv.2011.07.032.

Moritz, M. a, M. E. Morais, L. a Summerell, J. M. Carlson, and J. Doyle (2005), Wildfires, complexity, and highly optimized tolerance., *Proc. Natl. Acad. Sci. U. S. A.*, *102*(50), 17912–17917.

Newman, M. (1996), Self-organized criticality, evolution and the fossil extinction record, *Proc. R. Soc. …*, *3801*, 1–20.

Pausas, J. G. (2004), Changes in Fire and Climate in the Eastern Iberian Peninsula (Mediterranean Basin), *Clim. Change*, *63*(3), 337–350, doi:10.1023/B:CLIM.0000018508.94901.9c.

Pausas, J. G., and J. E. Keeley (2009), A Burning Story: The Role of Fire in the History of Life, *Bioscience*, *59*(7), 593–601, doi:10.1525/bio.2009.59.7.10.

Peterson, G. D. (2002), Contagious Disturbance, Ecological Memory, and the Emergence of Landscape Pattern, *Ecosystems*, *5*(4), 329–338, doi:10.1007/s10021-001-0077-1.

Press, W. H., S. A. Teukolsky, W. T. Vetterling, and B. P. Flannery (2002), *Numerical Recipes in C*.

Pueyo, S. (2007), Self-organised criticality and the response of wildland fires to climate change, *Clim. Change*, *82*, 131–161, doi:10.1007/s10584-006-9134-2.

Randerson, J. T. et al. (2009), Systematic assessment of terrestrial biogeochemistry in coupled climate-carbon models, *Glob. Chang. Biol.*, *15*, 2462–2484, doi:10.1111/j.1365-2486.2009.01912.x.

Randerson, J. T., Y. Chen, G. R. van der Werf, B. M. Rogers, and D. C. Morton (2012), Global burned area and biomass burning emissions from small fires, *J. Geophys. Res.*, *117*(G4), G04012, doi:10.1029/2012JG002128.

Reed, W. J., and K. S. McKelvey (2002), Power-law behaviour and parametric models for the size-distribution of forest fires, *Ecol. Modell.*, *150*(3), 239–254, doi:10.1016/S0304-3800(01)00483-5.

Ricotta, C., G. Avena, and M. Marchetti (1999), The flaming sandpile: self-organized criticality and wildfires, *Ecol. Modell.*, *119*(1), 73–77, doi:10.1016/S0304-3800(99)00057-5.

Ricotta, C. et al. (2001), Self-organized criticality of wildfires ecologically revisited, *Ecol. Modell.*, *141*(1-3), 307–311, doi:10.1016/S0304-3800(01)00272-1.

San-Miguel-Ayanz, J., J. M. Moreno, and A. Camia (2013), Analysis of large fires in European Mediterranean landscapes: Lessons learned and perspectives, *For. Ecol. Manage.*, *294*, 11–22, doi:10.1016/j.foreco.2012.10.050.

Song, W., F. Weicheng, W. Binghong, and Z. Jianjun (2001), Self-organized criticality of forest fire in China, *Ecol. Modell.*, *145*(1), 61–68, doi:10.1016/S0304-3800(01)00383-0.

Song, W., J. Wang, K. Satoh, and W. Fan (2006), Three types of power-law distribution of forest fires in Japan, *Ecol. Modell.*, *196*(3-4), 527–532, doi:10.1016/j.ecolmodel.2006.02.033.

Stöckli, R., D. M. Lawrence, G.-Y. Niu, K. W. Oleson, P. E. Thornton, Z.-L. Yang, G. B. Bonan, A. S. Denning, and S. W. Running (2008), Use of FLUXNET in the Community Land Model development, *J. Geophys. Res.*, *113*(G1), G01025, doi:10.1029/2007JG000562.

Stumpf, M. P. H., and M. a Porter (2012), Mathematics. Critical truths about power laws., *Science*, *335*(6069), 665–6, doi:10.1126/science.1216142.

Thonicke, K., S. Venevsky, S. Sitch, and W. Cramer (2008), The role of fire disturbance for global vegetation dynamics: coupling fire into a Dynamic Global Vegetation Model, *Glob. Ecol. Biogeogr.*, *10*(6), 661–677, doi:10.1046/j.1466-822X.2001.00175.x.

Thonicke, K., A. Spessa, I. C. Prentice, S. P. Harrison, L. Dong, and C. Carmona-Moreno (2010), The influence of vegetation, fire spread and fire behaviour on biomass burning and trace gas emissions: results from a process-based model, *Biogeosciences*, *7*(6), 1991–2011, doi:10.5194/bg-7-1991-2010.

Thornton, P. E., J.-F. Lamarque, N. A. Rosenbloom, and N. M. Mahowald (2007), Influence of carbon-nitrogen cycle coupling on land model response to CO 2 fertilization and climate variability, *Global Biogeochem. Cycles*, *21*(4), n/a–n/a, doi:10.1029/2006GB002868.

Thornton, P. E., S. C. Doney, K. Lindsay, J. K. Moore, N. Mahowald, J. T. Randerson, I. Fung, J.-F. Lamarque, J. J. Feddema, and Y.-H. Lee (2009), Carbon-nitrogen interactions regulate climate-carbon cycle feedbacks: results from an atmosphere-ocean general circulation model, *Biogeosciences*, *6*(10), 2099–2120, doi:10.5194/bg-6-2099-2009.

Trigo, R. M., J. M. C. Pereira, M. G. Pereira, B. Mota, T. J. Calado, C. C. Dacamara, and F. E. Santo (2006), Atmospheric conditions associated with the exceptional fire season of 2003 in Portugal, *Int. J. Climatol.*, *26*(13), 1741–1757, doi:10.1002/joc.1333.

Turcotte, D. L., and B. D. Malamud (2004), Landslides, forest fires, and earthquakes: examples of self-organized critical behavior, *Phys. A Stat. Mech. its Appl.*, *340*(4), 580–589, doi:10.1016/j.physa.2004.05.009.

Virkar, Y., and A. Clauset (2014), Power-law distributions in binned empirical data, *Ann. Appl. Stat.*, *8*(1), 89–119.

Vuong, Q. H. (1989), Likelihood Ratio Tests for Model Selection and Non-Nested Hypotheses, *Econometrica*, *57*, 307–333, doi:10.2307/1912557.

Yang, J., H. Tian, B. Tao, W. Ren, J. Kush, Y. Liu, and Y. Wang (2014), Spatial and temporal patterns of global burned area in response to anthropogenic and environmental factors: Reconstructing global fire history for the 20th and early 21st centuries, *J. Geophys. Res. Biogeosciences*, *119*(3), 249–263, doi:10.1002/2013JG002532.

Zinck, R. D., and V. Grimm (2009), Unifying wildfire models from ecology and statistical physics., *Am. Nat.*, *174*(5), E170–85, doi:10.1086/605959.

Appendix 2: Research output

Complete list of publications

Published papers:

- **Di Mauro B.,** Fava F., Busetto L., Crosta G.F. and Colombo R. Post-fire resilience in the Alpine region estimated from MODIS satellite multispectral data. *International Journal of Applied Earth Observation and Geoinformation*, Volume 32, October 2014, Pages 163-172, ISSN 0303-2434, http://dx.doi.org/10.1016/j.jag.2014.04.010. (2014) I.F. 2014: 3.47
- **Di Mauro B.,** F. Fava, L. Ferrero, R. Garzonio, G. Baccolo, B. Delmonte and Colombo R. Mineral dust impact on snow radiative properties in the European Alps combining ground, UAV, and satellite observations. *Journal of Geophysical Research - Atmospheres* 120, doi:10.1002/2015JD023287. (2015) I.F. 2014: 3.42
- Rotiroti M., **Di Mauro B.**, Fumagalli L. and Bonomi T. COMPSEC, a new tool to derive natural background levels by the component separation approach: application in two different hydrogeological contexts in northern Italy. *Journal of Geochemical Exploration* doi:10.1016/j.gexplo.2015.06.017. (2015) I.F. 2014: 2.747
- **Di Mauro B.**, F. Fava, Frattini P., Camia A., Colombo R. and Migliavacca M. Power law distributions of wildfires across Europe: benchmarking a land surface model with observed data. *Nonlinear Processes in Geophysics Discussion,* 2, 1553-1586, doi:10.5194/npgd-2-1553-2015, (2015) I.F. 2014: 0.987

Paper under review:

- Garzonio R., **Di Mauro B.**, Strigaro D., Colombo R., De Amicis M. and Maggi V. Mapping the Suitability for Ice Core Drilling of glaciers in the European Alps and in the Asian High Mountains. (In review for: *Journal of Glaciology*)

Papers in preparation:

- **Di Mauro B.**, Baccolo G., Garzonio R., Massabò D., Piazzalunga A., Colombo R. What darkens mountain glaciers? A geochemical and radiative assessment for the Vadret da Morteratsch (Swiss Alps) (In prepraration for: *The Cryosphere*)
- Garzonio R., Cogliati S., **Di Mauro B.**, and Colombo R. The Hyperspectral UAV (HyUAV): a novel spectroscopy tool for environmental monitoring. (In preparation for: *IEEE Transaction on Geoscience and Remote Sensing*)

Communications to conferences:

- **Di Mauro B.**, Fava F., Busetto L., Crosta G. F. and Colombo R. Evaluation of vegetation post-fire resilience in the Alpine region using descriptors derived from MODIS spectral index time series. Geophysical Reasearch Abstract. Vol. 15, EGU2013-4221 European Geoscience Union EGU, Vienna, Austria 2013. (Poster presentation)
- **Di Mauro B.**, Crosta G. F., Fava F., Busetto L., and Colombo R. A Dynamical System Perspective of Multi-temporal Remote Sensing: Analysis of MODIS Spectral Index Time Series from Forest Wildfires. Progress In Electromagnetics Research Symposium PIERS 2013 in Stockholm, Sweden, 2013 (Oral presentation)
- **Di Mauro B.**, Delmonte B., Fagnani M., Fava F. , Garzonio R. and Colombo R. Model simulation and hyperspectral measurements of snow albedo and light absorbing impurities. International Conference on Atmospheric Dust, Castellaneta Marina (TA), Italy 2014 (Keynote lecture)

- Di Mauro B., P. Frattini, A. Camia, R. Colombo and Migliavacca M. Spatial-temporal power law distribution of wildfires in Europe: a comparison between observed and simulated datasets. Data Analysis and Modeling in Earth Sciences, DAMES. Milan, Italy 2014. (Oral presentation)
- Di Mauro B., Fava F., Ferrero L., Garzonio R., Baccolo G., Delmonte B. and Colombo R. Mineral dust radiative effect on snow in the European Alps. Geophysical Reasearch Abstract. European Geoscience Union EGU, Vienna, Austria 2015. (Oral presentation)
- Garzonio R., Di Mauro B., S. Cogliati, A. Zanin, B. Tattarletti, F. Zacchello, P. Marras and Colombo R. The HYUAV: a novel UAV-based spectroscopy tool for environmental monitoring. UAVs in Environmental Research. University of Exeter, Cornwall (UK). (Oral presentation)
- Fussi F., F. Fava, B. Di Mauro, T. Bonomi, L. Fumagalli, M. Di Leo, C. H. Kane, G. Faye, M. Niang, S. Wade, B. Hamidou and R. Colombo. Integration of Remote Sensing and other public GIS data source to identify suitable zones for groundwater exploitation by manual drilling. European Geosciences Union (EGU), Vienna, Austria (2015).
- Fussi F, M. Di Leo, T. Bonomi, B. Di Mauro, F. Fava, L. Fumagalli, C. H. Kane, G. Faye, M. Niang, S. Wade, B. Hamidou and R. Colombo. Morphometric analysis with open source software to explore shallow hydrogeological features in Senegal and Guinea. European Geosciences Union (EGU), Vienna, Austria (2015).
- Fussi F., Fumagalli L., Bonomi T., Kane M., Niag M., Fava F., Di Mauro B., Wade S; Hamidou B; Rossini M, Colombo R. (2015). Integration of Stratigraphic Data, Pump Test and Geophysics for the Analysis of Shallow Unconsolidated Aquifers. In West Africa and Identification of Suitable Condition for Manual Drilling. IAH Congress - AQUA 2015, Roma.

- Cogliati S., R. Garzonio, **B. Di Mauro**, B. Tattarletti, F. Zacchello, P. Marras and R. Colombo. The Hyperspectral UAV (HyUAV) a novel UAV-based spectroscopy tool. ESSEM COST Action ES1309 OPTIMISE October 8th-10th 2014, Milan, Italy. (Oral presentation)
- Fava F. & **B. Di Mauro**, Remote sensing applications for Alpine seminatural system management and conservation, Forum Alpinum 2014, Boario Terme (IT) (Invited presentation)
- Fava F., Rossini M., Panigada C., Cogliati S., Julitta T., **Di Mauro B.**, Colombo R. (2014). Remote sensing applications for mapping ecosystem services in the European Alps First Italian meeting on the MAES working group activities, 27-2-2014, Rome (Invited presentation)
- Fussi F., L. Fumagalli, T. Bonomi, F. Fava, **B. Di Mauro**, C.H. Kane, M. Faye, S. Wade, G. Faye, B. Hamidou, and R. Colombo: Use of remote sensing and terrain modeling to identify suitable zones for manual drilling in Africa and support low cost water supply. Groundwater, poverty and development, Overseas Development Institute, London 28/11/2014 (Oral presentation)
- Garzonio R., **B. Di Mauro**, D. Strigaro, M. De Amicis, V. Maggi, R. Colombo, Definition of a methodology to map the suitability of mountain glaciers for ice core drilling using morphometric and climatic indicators, International symposium on The Future of the Glaciers 2014, Turin (IT) (Oral presentation)
- Rotiroti M., **B. Di Mauro**, L. Fumagalli and T. Bonomi, Component separation approach to estimate natural background levels: a case study from the lower Po Plain (northern Italy), Flowpath 2014, Viterbo, (IT) (Oral presentation)
- Fava F., Migliavacca M., Rossini M., **Di Mauro B.**, Julitta T. and Colombo R. Land Surface Phenology of Alpine environments in the European Alps from MODIS data. COST Action ES0903 EUROSPEC Final Conference, 6-8 November 2013 (Poster presentation)

- Comi A., Degni F., Cutellè C.F., Cogliati S., Rizzi C., Casati M., Sangiorgi G., Perrone M.G., **Di Mauro B.**, Mocnik G., Bolzacchini E., Ferrero L. Characterising the U9 Milan background site that links together radiation and pollution measurements. European Aerosol Conference EAC2015 - September 6th to 11th.Milan 2015. (Poster presentation)
- **Di Mauro B.**, G. Baccolo, R. Garzonio, A. Piazzalunga, D. Massabò, and R. Colombo. Mountain glaciers darkening: geochemical characterization of cryoconites and their radiative impact on the Vadret da Morteratsch (Swiss Alps). Accepted for EGU 2016
- **Di Mauro B.**, T. Julitta, and R. Colombo. Glacier albedo decrease in the European Alps: potential causes and links with mass balances. Accepted for EGU 2016
- Quarfeld J., **Di Mauro B.**, Julitta T., Verbesselt J., Colombo R. Exploring fire dynamics with BFAST approach: case studies in Sardinia, Italy. Accepted for EGU 2016
- Ferrero L., Mocnik G., Cogliati S., Comi A., Degni F., **Di Mauro B.**, Colombo R., and Bolzacchini E. Direct Radiative Effect and Heating Rate of black carbon aerosol: high time resolution measurements and source-identified forcing effects. Accepted for EGU 2016